MODELING OF MECHANICAL PROPERTIES OF CERAMIC-METAL COMPOSITES FOR ARMOR APPLICATIONS

by

Ali Mansur

A thesis submitted to the Faculty of Graduate and Postdoctoral Studies

in partial fulfillment of the requirements for the degree of

MASTER OF APPLIED SCIENCE

In Mechanical Engineering

Ottawa-Carleton Institute for Mechanical and Aerospace Engineering

University of Ottawa

Ottawa, Canada

(July 2011)

Abstract

In this study, AISI 450 stainless steel and ceramic-metal matrix composites (CMMCs) impacted by a 7.61x51mm armor piercing (AP) projectile, are numerically investigated. The numerical simulations are performed using the finite element method Abaqus/Explicit. For AISI steel, a total of three different failure criteria are used in order to determine the critical thickness values for perforation for different projectile impact velocities: (1) the standard Abaqus ductile and shear criteria; (2) the local tensile elongation at fracture; and (3) the strain energy absorbed by the material at fracture. Mechanical properties including the yield strength and the percentage elongation at fracture are obtained from literature stress-strain data. Overall, the standard Abaqus and the elongation to fracture criteria yield comparable results, while the strain energy model yields critical plate thickness values nearly twice as large as those obtained using the two other models. Because of the unavailability of most parameters needed for the standard ductile-shear criteria, only the alternative failure criteria, elongation to fracture and strain energy, were used for CMMCs, specifically WC-CO. This yielded critical plate thicknesses for perforation similar to those of AISI 450 stainless steel. This result is contrary to the real condition experience and expectation that CMMCs provide better ballistic performance. It can be rationalized by the non-consideration of local heating and shear band formation in this study. Still overall, experimental data from literature and the modeling results of this study are in fairly good agreement. However, substantial improvements are still required to make finite element analysis (FEA) modeling an accurate tool for the characterization of the ballistic impact events. Including local heating at the impact point and shear band formation as well as better defining the effective deformation volume are key aspects for future studies.

Acknowledgements

I am thankful to God for providing me with good health and power of thinking. The author wishes to express his sincere gratitude to his professors, Dr. Michel Nganbe and Dr. Atef Fahim for the endless effort that they have devoted to helping further this research. Their guidance and advice have been greatly appreciated. Without their help, this research could not have been completed. I am thankful to the Faculty of Graduate and Post Doctoral Studies (FGPS), the Faculty and staff members of the Mechanical Engineering Department at the University of Ottawa, Canada who provided me all kinds of possible support and a better working environment. I would like to appreciate the devotion of my parents, wife and kids who gave me enough time from their share to complete this work.

Contents

Abstract ii

Acknowledgements iii

1 Introduction 1

  1.1 Layout 4

2 Literature Review 5

  2.1 Deformation and fracture of metal based materials 5

    2.1.1 Elastic deformation 5

    2.1.2 Plastic deformation 6

    2.1.3 Deformation energy and fracture 7

    2.1.4 High strain rate deformation 9

  2.2 Finite Element Analysis of the impact event 10

  2.3 Armor materials 14

  2.4 Composite materials 17

    2.4.1 Basic Concepts 18

    2.4.2 Types of Composite Materials 19

3 Finite Element Modeling 21

  3.1 Introduction to the Abaqus software 21

    3.1.1 Abaqus/Standard and Abaqus/Explicit 22

  3.2 Numerical model and simulation 22

  3.3 Modeling with standard Abaqus ductile and shear failure criteria 29

    3.3.1 Progressive damage and failure 29

    3.3.2 Damage initiation criteria for the fracture of metals 30

    3.3.3 Damage evolution 32

  3.4 Modeling with alternative failure criteria 34

    3.4.1 Critical principal strain criterion 36

    3.4.2 Critical strain energy criterion 37

  3.5 Material definitions 40

4 Results 44

5 Discussion and Validation 62
6 Conclusions..65
7 Future work..67
8 References..68
9 Appendix..75

List of Tables

Table 3.1: Modeling with different meshing size 23

Table 3.2: Physical and mechanical properties of target plates and projectiles used in this study..25

Table 4.1: Critical thicknesses for perforation of AISI 450 stainless steel plates by a 7.62x51mm hard tungsten carbide projectile for different projectile velocities and models .54

Table 4.2: Critical thicknesses for perforation of WC-CO composite impacted by a 7.62x51mm hard tungsten carbide projectile for different projectile impact velocities using Abaqus with the elongation to fracture failure criterion..57

Table 4.3: Critical thickness calculated using the energy method...60

Table 4.4: Simulated critical thicknesses for different plate materials, projectiles, and impact speeds using the elongation to fracture failure criterion...61

List of Figures

Figure 2.1: Typical stress-strain diagram with the various stages of deformation………..…5

Figure 2.2: Modulus of resilience ………………………………………………………8

Figure 2.3: Toughness or total energy per unit volume absorbed by the material until fracture…………………………………………………………………..…………9

Figure 2.4: Mechanisms of armor penetration...…………………………….…………10

Figure 2.5: Classification of composite materials ……………………………..…………16

Figure 2.6: Types of Composite Materials ………………………………….………19

Figure 3.1: Plate model in 3D……………………………………………………….24

Figure 3.2: The real 7.62 x 51 mm Armor Piercing projectile……………………………...26

Figure 3.3: Dimensions of the 7.62x51 mm Armor Piercing projectile ………………...….26

Figure 3.4: The 7.62x51 projectile model in 3D……………………………………..…26

Figure 3.5: Meshed model of plate and projectile………………………………………..27

Figure 3.6: Initial assembly of projectile and plate/target with zero (0) gap……………..…28

Figure 3.7: Boundary conditions applied in the model…………………………...………28

Figure 3.8: Typical uniaxial stress-strain response of a ductile metal specimen …………...29

Figure 3.9: Stress-strain curve with progressive damage degradation …………………..….33

Figure 3.10: Real plasticity with strain hardening (a) and perfect plasticity curves (b) considered in this study…………………………………………………………...35

Figure 3.11: Stress-strain curves for brittle and ductile materials. The colored area below the curve represents the strain energy per unit volume at fracture …………………………….38

Figure 3.12: Cone representing the effective deformation volume of the plate during impact…………………………………………………………………………………..39

Figure 3.13: Front (a) and back (b) circular surfaces of the effective deformation cone volume………………………………………………………………………………….39

Figure 3.14: Experimental stress-strain curve of AISI 450 stainless steel with strain hardening ……………………………………………………………………...……….41

Figure 3.15: Perfectly elastic-plastic stress-strain curve for AISI 450 stainless steel ……...41

Figure 3.16: True stress-strain curve of WC-CO ……………………………………...…42

Figure 3.17: Perfectly elastic-plastic stress-strain curve for WC-CO………………………42

Figure 3.18: Engineering stress–strain curves for Weldox 460 E and Weldox 700 E ……...43

Figure 3.19: Perfectly elastic-plastic stress-strain curves for Weldox 460 E and Weldox 700 E……………………………………………………………………………………..43

Figure 4.1: Penetration simulation of a 7.62x51mm hard tungsten carbide projectile with an impact velocity of 360 m/s through a 9.9 mm thick AISI 450 stainless steel plate…………46

Figure 4.2: Kinetic and strain energy for the whole model changes during impact of a 9.9 mm thick AISI steel plate by a 7.62x51mm hard tungsten carbide projectile at a velocity of 360 m/s……………………………………………………………………………………47

Figure 4.3: The kinetic energy of the projectile during the impact of a 9.9 mm thick AISI steel plate at 360 m/sec……………………………………………………………...47

Figure 4.4: The velocity of the projectile during the impact of a 9.9 mm thick AISI steel plate at 360 m/sec…………………………………………………………………………48

Figure 4.5: Kinetic and strain energy for the whole model changes during impact of a 9.9 mm thick AISI steel plate by a 7.62x51 mm hard tungsten carbide projectile with an impact velocity of 340 m/s……………………………………………………………..……49

Figure 4.6: The kinetic energy of the projectile during the impact of a 9.9 mm thick AISI steel plate at 340 m/sec……………………………………………………...……49

Figure 4.7: The velocity of the projectile during the impact of a 9.9 mm thick AISI steel plate at 340 m/sec……………………………………………………………………………50

Figure 4.8: Deformation progression at the back surface of an 8.7 mm thick AISI plate struck by a 7.62x51mm hard tungsten carbide projectile with an impact velocity of 360 m/s…….52

Figure 4.9: Kinetic and strain energy for the whole model changes during impact of an 8.7 mm thick AISI 450 stainless steel plate by a 7.62x51 mm hard tungsten carbide projectile at a velocity of 360 m/s…………………………………………………………………...…53

Figure 4.10: the kinetic energy of the projectile during the impact of an 8.7 mm thick AISI 450 stainless steel plate at 360 m/sec…………………………………………………..…53

Figure 4.11: Dependence of the critical thicknesses for perforation of AISI 450 stainless steel plates on projectile speed as determined using models with standard ductile and shear criteria, as well as with the elongation to fracture criterion……………………………...….55

Figure 4.12: Maximum deformation at the back surface of AISI 450 stainless steel targets versus impact velocity……………………………………………………………………….56

Figure 4.13: Dependence of the critical thickness for perforation of WC-CO plates on projectile speed as determined using the elongation to fracture failure criterion………...…57

Figure 4.14: Deformation progression at the back surface of a 9.7 mm thick WC-CO plate struck by a 7.62x51 mm hard tungsten carbide projectile with an impact velocity of 400 m/s……………………………………………………………………………………...….59

Figure 4.15: The maximum deformation of the back surface of WC-CO plates versus the impact velocity……………………………………………………………………………59

Nomenclature

σ	Applied stress
E	Young's modulus
ε	Resulting strain
% EL	Percentage of plastic strain at fracture
l_f	Fracture length
l_o	Original length
% RA	Percent reduction in area
A_o	Original cross sectional area
A_o	Cross sectional area at the point of fracture
u	Strain energy per unit volume (Strain-energy density)
ε_f	Fracture strain
u_r	Modulus of resilience
u_r	Modulus of toughness
$\boldsymbol{\rho}$	Density
v	Poisson’s ratio
σ_y	Yield stress
el%	Elongation at break
η	Stress triaxiality

$\dot{\varepsilon}^{pl}$	Strain rate
$\bar{\varepsilon}_{\mathrm{D}}^{pl}$	Equivalent plastic strain at the onset of ductile damage
p	Pressure stress
q	Von Mises equivalent stress
θ_s	Shear stress ratio
τ_{max}	Maximum shear stress
k_s	Material parameter
$\bar{\varepsilon}_0^{pl}$	Equivalent plastic strain at the onset of damage
$\bar{\varepsilon}_f^{pl}$	Equivalent plastic strain at failure
D	Overall damage variable
$\bar{\sigma}$	Effective (or undamaged) stress tensor
σ_{true}	True stress
ε_{ln}^{pl}	True plastic strain
σ_{nom}	Nominal stress
ε_{nom}	Nominal strain
$\mathrm{K_E}$	Kinetic energy
m	Projectile mass
v	Initial velocity
V_c	Volume of the cone

r_1	Radius of the front cone face
r_2	Radius of the back cone face
t	Thickness of the plate

1 Introduction

Increasing security concerns are forcing developed countries to find sophisticated ways to protect their citizens at home, and their troops during peace-keeping missions abroad. One of the most efficient protection methods is the use of armor systems. However, the failure of even the best armored tanks has shown that novel materials are needed for better protection. Conventional materials such as high strength steels are heavy, and they often fail by strong concentration of plastic deformation accompanied by extreme adiabatic heat in few shear planes, which strongly soften the material. On the other hand, harder materials such as ceramics do not possess sufficient toughness and generally need to be backed up by more ductile metals. The objective of the project is therefore to investigate ceramic-metal nano-composites for use in armor systems. Ceramic nano particles are expected not only to strengthen metal matrixes such as high strength steel, but also to disperse plastic deformation and prevent the formation of adiabatic shear bands. The requirements for armor design are dependent on the applications of the system being protected. The most important factors are protective capacity, cost, and weight. Several contributions have been made to investigate the performance of fabric, soft laminate, and composite armors [12-33]. Despite the wealth of available experimental and numerical investigations on the perforation and penetration of ductile metal and ceramic composite targets impacted by different projectiles, few studies have investigated the damage formation and the failure in ceramic-metal matrix composite (CMMC) targets struck by projectiles.

The experimental analysis is often used to study impact loading, deformation, and damage of armor plates. However, this method is expensive, time consuming, and requires multiple standardized test prototypes, equipment, and strongly regulated test settings. A significant advantage of finite element analysis (FEA) is that an advanced preliminary study can be carried out using a virtual prototype in a virtual environment which can substantially cut costs, reduce the development time, and substantially optimize the overall development process for armor materials.

The objective of this research is to use the finite element software Abaqus to model the dynamic impact loading of steel and ceramic-metal matrix composite plates by ballistic projectiles. The specific goals are:

- To study the plastic deformation and its concentration in armor plates during impact.
- To study and compare different approaches for defining the failure criterion.
- To validate and optimize the FEA simulation of ballistic impacts using impact test data available in the literature.
- To use FEA to predict critical thicknesses for the penetration of steel and ceramic-metal matrix composites by ballistic projectiles.
- To investigate steel and ceramic-metal matrix composites for use in armor systems.
- To study potential advantages and disadvantages of ceramic-metal matrix composite armors as compared to their steel counterparts.

Due to the high impact speed and strain-rate, the heat locally generated by the plastic deformation and friction in the impact region has no time to dissipate and be transferred or conducted away. Therefore, the impact region and the few activated shear regions behave adiabatically resulting in extreme local temperature rise, softening and ultimately excessive plastic deformation or even failure. This is known as adiabatic shear localisation or thermal-plastic instability which causes the so-called adiabatic shear bands (ASB) which can be extremely narrow in some cases.

Ceramic metal matrix composites have been experimentally shown to provide better ballistic performance than steel; however, modeling studies are yet to be done to better understand the basis of this superiority. The current work is one of the very first of its kind to numerically study the ballistic impact behavior of nanostructured ceramic-metal matrix composites. This in addition to time constrains, dictate that the focus of the thesis be on the overall material deformation and the investigation of whether standard methods used on metallic materials and polymer composites can be applied to ceramic-metal matrix composites. Multiple studies have been carried out recently to numerically capture adiabatic shear band formation, mostly using meshless numerical methods. In fact, with the currently available techniques it is practically impossible to capture adiabatic shear band formation using Finite Element Analysis due to the extremely small mesh size required which may lead to element distortion and locking during modeling. It is further important to note that friction, heat, thermal softening as well as the effects of shock wave and impedance are not considered in the used FEA model. Therefore, modeling errors can be expected particularly at high projectile impact speed.

1.1 Layout

The thesis is subdivided into seven chapters. After an introduction to the research topic in chapter 1, a literature review on material deformation and the analysis of the impact event is presented in chapter 2. In chapter 3, a theoretical background on the finite element approach is presented and the use of the FEA software Abaqus for the ballistic impact is explained. Chapter 4 summarises the results, and chapter 5 contains a discussions and a validation of the obtained modeling values. Finally, conclusions are presented in chapter 6 and chapter 7 lays out suggestions for future work.

2 Literature Review

2.1 Deformation and fracture of metal based materials

When a sufficient load is applied to a metal or a material, it undergoes elastic and partially plastic. The level of deformation depends on the type of material, forces applied, size, and geometry of the material. Figure 2.1 shows the engineering stress-strain diagram for a typical ductile material such as steel.

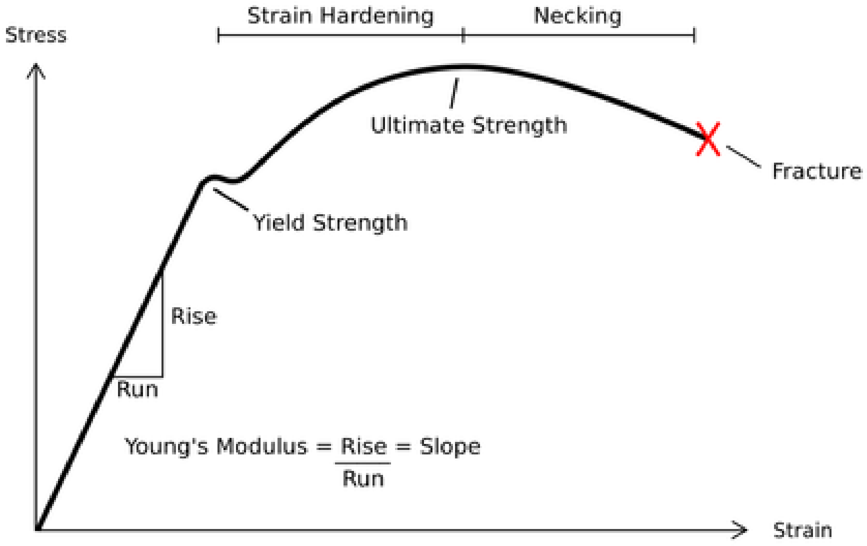

Figure 2.1: Typical stress-strain diagram with the various stages of deformation [1]

2.1.1 Elastic deformation

Elastic deformation of materials is a reversible shape change at relatively low stresses. The linear-elastic deformation is governed by the Hooke's law:

$$\sigma = E \, . \, \varepsilon \qquad (2.1)$$

Where σ is the applied stress, E is a material constant called Young's modulus, and ε is the resulting strain. This linear relationship allows determining the modulus of elasticity, or Young's modulus, defined as the slope of the stress-strain curve in the elastic range. The elastic range ends when the material reaches its yield strength. At this point, plastic deformation begins as can be seen in Figure 2.1.

However, some materials such as concrete, gray cast iron, and many polymers, respond nonlinearly in the elastic region. For these materials, the Hooke's law is inapplicable. The magnitude of the modulus of elasticity of most typical metals ranges between 45 GPa for magnesium and 407 GPa for tungsten [2].

2.1.2 Plastic deformation

Plastic deformation begins above the yield point and is permanent, irreversible or non-recoverable. The stress is no longer linearly proportional to the strain and the Hook’s law (2.1) is not valid in the plastic range.

In the stress-strain curve in Figure 2.1, the plastic deformation is defined by a strain hardening region, necking region and finally fracture. Due to strain hardening, the stress needed to further deform the material increases with strain and the material becomes stronger till the maximum stress (ultimate strength) is reached. After the ultimate strength, necking occurs resulting in a reduction in cross sectional area of the material. Therefore, the material’s resistance to deformation decreases ultimately leading to material fracture.

The ability of materials to undergo plastic deformation before fracture defines their failure mode as either ductile or brittle. The ductility of materials is a measure of the degree of plastic deformation sustained prior to fracture. Ductile materials have four distinct deformation stages: elastic behavior, yielding, plastic deformation and strain hardening, and necking. Brittle materials have very little or no yielding behavior, rather they fracture suddenly without or after only little prior plastic deformation, warning or notice.

The ductility of materials can be expressed by the percentage elongation or the percentage reduction in area until fracture:

$$\% \text{ EL} = \left(\frac{l_f - l_o}{l_f}\right) \text{x100} \qquad (2.2)$$

$$\% \text{ RA} = \left(\frac{A_o - A_f}{A_o}\right) \text{x100} \qquad (2.3)$$

Where % EL is the percentage of plastic strain at fracture, l_f is the fracture length, l_o is the original length, % RA is the percent reduction in area, A_o is the original cross sectional area and A_f is the cross sectional area at the point of fracture.

2.1.3 Deformation energy and fracture

When a material is deformed by an external loading, it tends to store strain energy internally throughout its volume. The strain energy per unit volume is called the *strain-energy density* ***u*** and can be expressed as

$$u = \int_0^{\varepsilon_f} \sigma \, d\varepsilon \qquad (2.4)$$

where ε_f is the fracture strain.

The modulus of Resilience is the ability of the material to absorb elastic energy per unit volume without any permanent deformation. The modulus of resilience u_r is the *elastic* *strain-energy density* and is represented by the shaded area under the stress-strain curve up to the yield point. It is obtained by integration from zero to the elastic limit of the material see Figure 2.2 and equation (2.5) applies.

$$u = \frac{1}{2}\frac{\sigma^2}{E} \qquad (2.5)$$

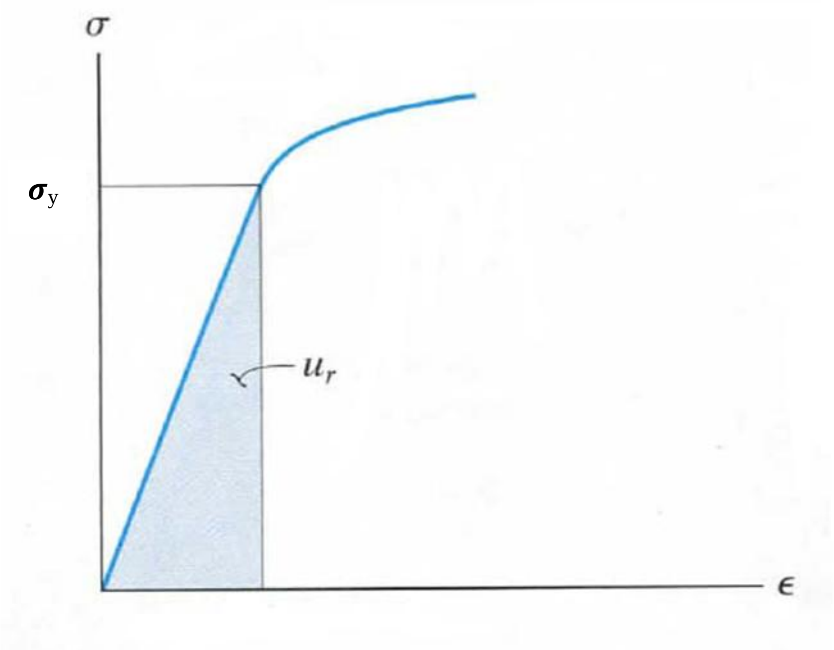

Figure 2.2: Modulus of resilience [3]

The toughness is the ability of the material to absorb elastic and plastic strain energy by plastically deforming prior to fracture. It is the *strain-energy density* represented by the shaded area under the diagram in Figure 2.3.

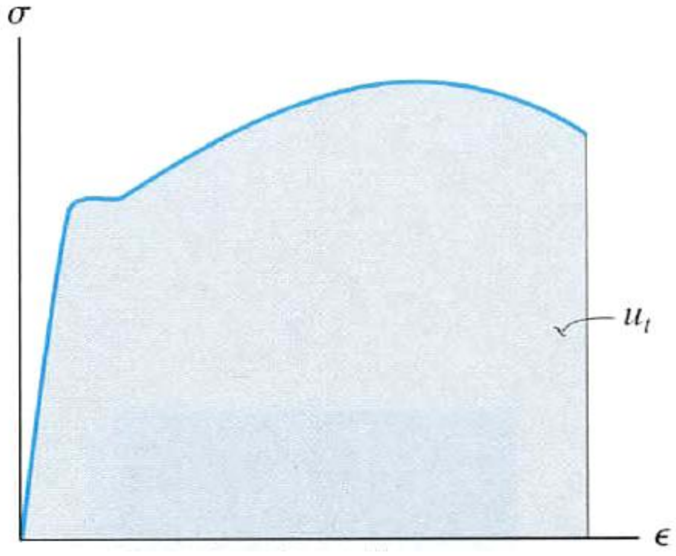

Figure 2.3: Toughness or total energy per unit volume absorbed by the material until fracture [3]

2.1.4 High strain rate deformation

The strain rate is the speed of deformation of materials subjected to stresses. As most deformation processes are time dependent, particularly at high temperature, deformation and failure mechanisms depend on strain rate. As the strain rate increases, the deformation process changes gradually from fully isothermal to fully adiabatic, because there is not enough time for the heat generated during deformation to escape out of the body at extremely high strain rates. This can give rise to adiabatic shear instability that has a profound effect on the mechanical response of the material. As deformation proceeds, adiabatic heating can occur in a narrow region and thermal softening dominates the plastic deformation leading to the formation of adiabatic shear bands. Adiabatic shear bands (ASB) result from deformation instability and are thin regions of highly deformed material, which are often the sites of further damage and complete failure. ASBs are often created during shock wave loading that is characterized by high strain rate in the material. They are usually more brittle than the bulk material and have been shown to be the cause of many cases of failure under dynamic loading.

2.2 Finite Element Analysis of the impact event

Impact can be defined as a high force or shock applied over a short period of time when two or more bodies collide. The effect critically depends on the relative velocity of the bodies with one another. When an armor plate is subjected to a ballistic impact, the kinetic energy of the projectile is transferred to the plate and is absorbed thereby converting kinetic energy into strain energy. Therefore, deformation occurs in the impacted area of the plate. If the plate absorbs greater energy, a larger deformation of the material occurs. However, the projectile penetrates or passes through (perforation) the plate if the kinetic energy exceeds the capability of the energy absorption of the material of the plate [4]. Figure 2.5 shows the various failure mechanisms of armors.

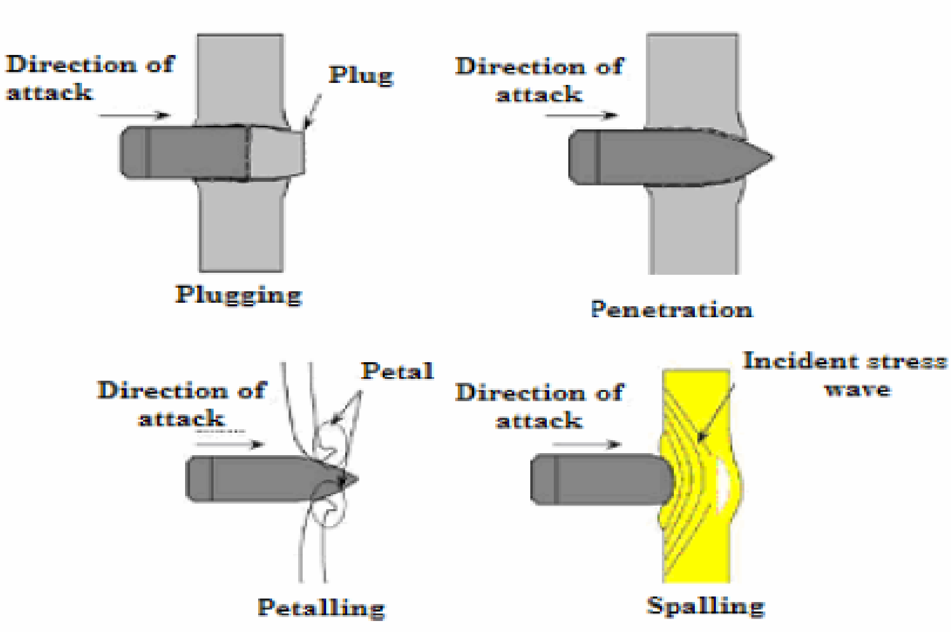

Figure 2.4: Mechanisms of armor penetration [5]

Plugging occurs in the material when impacted by a blunt or hemispherical-nosed projectile at a velocity close to the ballistic limit that causes plugging failure by slugging of approximately the same diameter as the projectile.

Penetration is defined as the digging of projectile into the target body afar from the thickness of spall crater. The measurement of cross section of the digging depth is called penetration depth.

Petalling is produced by high radial and circumferential tensile stresses after the passage of the initial stress wave. The intense-stress fields occur near the tip of the projectile. Bending moments created by the forward motion of plate material pushed by the striker causes the characteristic deformation pattern. It is most frequently observed in thin plates struck by conical bullets at relatively low impact velocities or by blunt projectile near the ballistic limit [6].

Spalling is tensile failure as a result of shock wave propagating from the rear surface of a finite-thickness plate being impacted. Spalling occurs in materials that are stronger in compression than they are in tension (e.g. ceramic armors).

Designing light-weight armors is a complex task and requires a comprehensive understanding of the different stages of the impact process. There are several different methodologies to assess the design of light weight armors. First, the experimental method provides the highest accuracy, but the drawbacks include cost and lack of detailed information for the impact event. Second, numerical modeling provides a better understanding of the process and is quite valuable for an improved armor design. The main advantage of numerical modeling is that it can provide an analysis of a definite projectile-target system in a very short period of time using only a personal computer and appropriate software [7].

A fair amount of research has been completed addressing different aspects of modeling impact loading and damage of armor plates under low and high velocities. Børvik et al. [8] described a coupled computational model of viscoplasticity and damage for the prediction of deformation and facture in ductile materials (Weldox 460E steel) using the explicit finite element code LS-DYNA and reported that the numerical solution is found to be mesh sensitive. Nazeer et al. [9] investigated the perforation of ductile metal targets by a conical indenter and developed mathematical relations for the fracture mechanism with respect to the response and fracture toughness of metal sheets of various thicknesses with the following conclusions:

1. The fracture toughness analysis of ductile material sheets can be performed by this method.
2. The sheet bending angle decreases almost linearly with the conical tool angle.
3. The results were reproducible on SIC half-hard and NS4 aluminum sheets.
4. The process can be mathematically analyzed using rigid-plastic fracture mechanics.
5. The number of cracks/petals formed and the fracture toughness of the material can be evaluated using this analysis.
6. The parametric optimal behavior is characteristic of conical tools and has not been observed in ball and sharp tool indentation of the ductile metal sheets. The effect of relative deformability of missile and plate on the ballistic limit of thin ductile plates struck at normal obliquity by soft cylindrical missiles was studied by Liu and Stronger [10]. It was shown that the failure changed from dishing to plugging as the ratio of the plate thickness to missile

radius increased and a soft or deformable missile changes shape as it penetrates a ductile metal target.

Rusinek et al. [11] studied the experimental and numerical analysis of the failure process of mild steel sheets subjected to normal impact by hemispherical projectiles and reported that petalling is the failure mode predicted for all cases studied in the absence of plug ejection; the number and the disposition of the petals were in agreement with the experimental observations.

Several contributions have been made to investigate the performance of composite armors, fabrics, soft laminates, and fiber reinforced composites [12-33].

The ballistic efficiency of ceramic/metal composite armor systems against 7.62 armor piercing (AP) and 40.7g steel projectiles was investigated by M. Lee and Y.H. Yoo [12]. They reported that the optimum thickness ratio h_1/h_2 is between 1.5 and 3, where h_1 is the ceramic plate thickness and h_2 is the backing plate thickness. They combined numerical and experimental approach and concluded that the simulation method, which is more cost-effective than experiments, can be used as a useful design tool for the optimization of lightweight ceramic/metal armor systems. Wang et al. [13] studied the dynamic response of alumina tiles backed by aluminum plates under conditions of normal impact by cylindro-conical projectiles. They found that the tip of the striker is flattened and a conical fracture pattern develops at the projectile’s front. They identified that the required backing plate thickness is a function of the deformation mechanism (petalling, plugging, partial penetration and indentation). In addition, they noted that the fracture propagation speed in alumina was about 3000 m/s, significantly slower than the shock wave speed, which was roughly 10000 m/s and the ballistic limit increased as the ceramic became thicker.

Espinosa et al. [14] investigated the response of multilayered ceramic–steel targets at high velocity impact and penetration using finite element simulation. They found that the penetration process is highly dependent on the multilayered configuration and the target structural design (geometry and boundary condition) which is found to be less dependent on the ceramic materials as usually assumed by most investigators.

Although there have been many experimental and numerical investigations on the perforation and penetration of ductile metal and ceramic composite targets impacted by different projectiles, few studies have investigated the damage formation and the failure in nano ceramic-metal matrix composites (CMMC) targets struck by projectiles. The ballistic performance of CMMCs was investigated through experimental tests using high-speed machinegun bullets and numerical modeling by T. Lin and Q. Yang [34]. They presented the latest development of a novel class of nanostructured metal matrix composites (NMMCs) based on submicron SiC particulates reinforced nanocrystalline Al alloys. They reported that the predicted penetration depth obtained from the modified ballistic model agreed very well with those from real tests, with a deviation less than 10%.

2.3 Armor materials

A number of criteria must be considered when selecting materials for use in armor systems including allowable volume and costs. No single armor material is best. Rather, a material providing adequate protection against one specific threat in a given system configuration may be inadequate for a different application, particularly if its volume or weight needs to be reduced [35].

The most common materials used for armor applications are:

Steel (Rolled homogeneous armor) is strong, hard and tough; it does not shatter when struck by a fast moving hard projectile.

Aluminum is used when light weight is required. It is most commonly used on APCs (Armored personnel carrier) and armored cars.

Wrought Cast Iron is used as ironclad for some warships.

Titanium is considered to be the most effective metal armor. However, it has not seen much use due to its very high costs.

High Density Depleted Uranium is sometimes used in tank amours, generally sandwiched between sheets of steel armor plates.

Plastic Armors are highly effective for stopping armor piercing bullets because they can deflect the projectile and lodge it between the plastic armor and the steel backing plate.

Bulletproof Glass is an informal term for *glass* that is particularly resistant to penetration when struck by a bullet.

Ceramics: The most common ceramics used for armor applications are Silicon Carbide, Boron Carbide, Titanium Diboride, Aluminum Nitride, Silicon Nitride, Aluminum Oxide (85% pure), Aluminum Oxide (high purity), Tungsten Carbide and Glass [36].

Composites:

The classification of composite materials is shown in Figure 2.5, which consists of three main classes: particle-reinforced, fiber-reinforced, and structural composites.

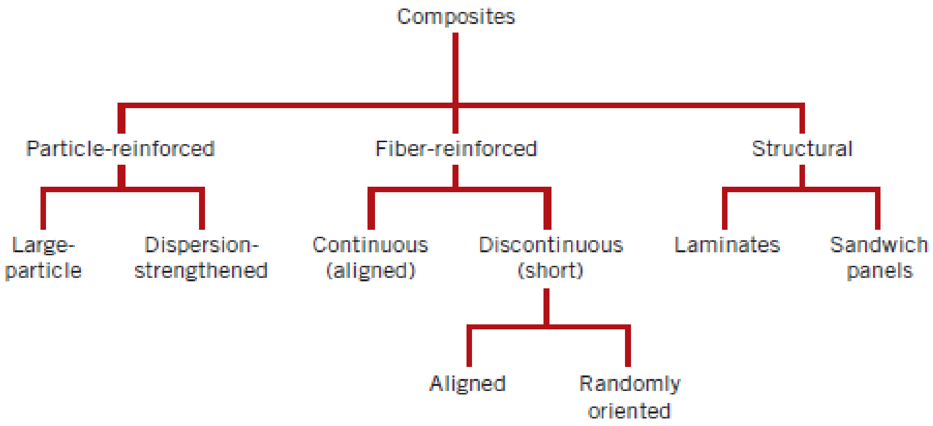

Figure 2.5: Classification of composite materials [2]

Body armors were very heavy in the 1990s when they were used by peacekeeping soldiers in 1993 in Mogadishu, Somalia. The heavy weight reduced the soldiers' mobility and dramatically increased their fatigue. Consequently, armors reduced their capabilities to fight and increased casualties. Although lighter weight ceramic armors were available, the manufacturing costs and therefore purchasing costs were too high.

The requirements for armor design are depending on the applications of the system being protected. The most important factors are protective capacity, cost, and weight. Weight is not a critical factor in case of defensive walls or bunkers. Therefore, low cost materials can be used by increasing the resistance with larger thickness. However, in the case of moving targets, weight plays a very important role. In land vehicles, light weight armor materials save engine power and increase the efficiency of the vehicle. In aircraft, the weight of each part is crucial and must be considered. In body armors where person mobility is essential, the weight is extremely important as well and different materials can be used. Metals have very good ballistic efficiency but their high density is a drawback. Ceramic materials are limited by their brittleness, as they shatter on account of their poor toughness.

The combination between low density and high hardness ceramics with ductile metals offers the possibility of reducing weight per unit area thereby providing better ballistic efficiency [44].

Furthermore, gradient materials with the hardness decreasing and the toughness increasing from a harder impact face to a more ductile backing face are other options. Examples of such applications are body protection for small calibre bullets, blast protection for shelters, waste cans, vehicles, tanks, etc.

The application of lightweight ballistic materials is used in numerous products by military, police, law enforcement agencies and UN peacekeepers around the world. Applications range from helmets to law enforcement and police vests, hand-held riot shields, bomb blanket, combat vehicle-Stryker, HMMWV (The High Mobility Multi-Purpose Wheeled Vehicle), expeditionary fighting vehicle, advanced composite armored vehicle platform (ACAVP), armored helicopters, armored helicopter crashworthy seats, C130 cargo gunship airplane, armored ballistic kits for aircraft, armored police and civilian vehicles, LCAC (landing craft, air cushion) fleet and armored hovercraft [45]

2.4 Composite materials

Composites are made of various combinations of two or more materials from different classes: metals, polymers, and ceramics. Therefore, they provide scientists and engineers with an exceptional combination of properties such as outstanding mechanical strength and toughness and in some cases even lower costs, which cannot be achieved with traditional materials [37,38].

Composite materials are utilized in a range of structural applications within the transportation, medical, communication, manufacturing armor and recreation industries. The decision to implement a particular composite system depends on a number of factors, including the economics of production, the ease of fabrication into complex shapes and the chemical reactivity of the single constituents and the composite as a whole [39].

2.4.1 Basic Concepts

Any type of material (Metals, Polymers, Ceramics), taken individually has qualities and weaknesses. Polymers can be easily processed, are very light and relatively cheap but display low strength and low melting point. Metals feature strength and ductility but are heavy, sensitive to corrosion and wear. Ceramics have high hardness, are very stiff and wear resistant, but are brittle. Combinations in various proportions of metal, polymer and/or ceramic using appropriate processes can produce composites with tailored properties for specific applications.

Composites are made of two main types of constituents which are the strengthening /reinforcing elements (in forms of fibers, whiskers or particles) and the matrix (for cohesion and load transmission). One of the main features of composites is a proportion of reinforcing constituents significantly high so that a load transfer can effectively occur between the matrix and the strengthening elements [37, 38].

There are three main classes of composite materials: Polymer Matrix Composites (PMC), Metal Matrix Composites (MMC) and Ceramic Matrix Composites (CMC). For high temperature environments, the last two are mostly used. Although their manufacturing processes can follow a liquid or a vapor route, one of the most prominent approaches has been solid processing with Powder Metallurgy (PM) techniques. In this study we mainly focus on Metal Matrix Composites.

2.4.2 Types of Composite Materials

There are five basic types of composite materials: Fiber, particle, flake, laminar or layered and filled composites as seen in Figure 2.6.

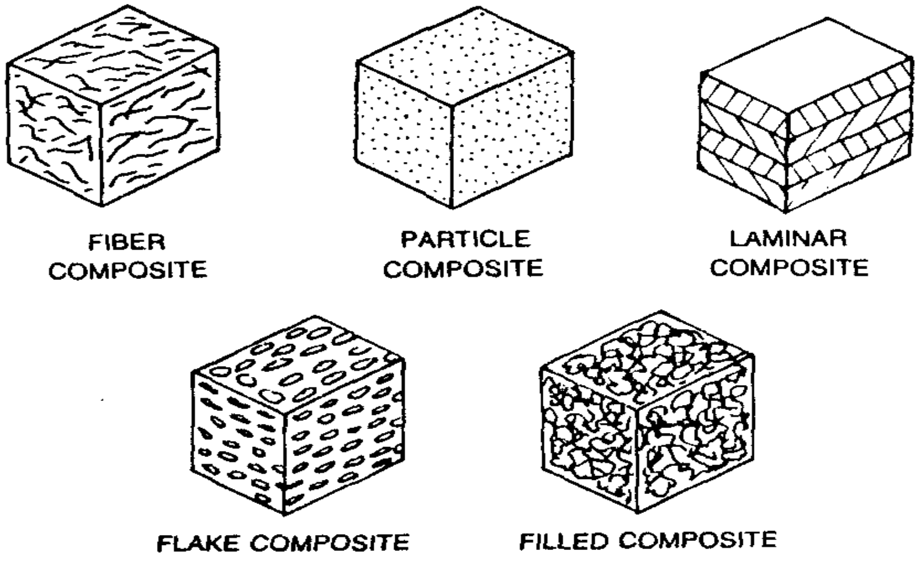

Figure 2.6: Types of Composite Materials [41]

Metal Matrix Composites (MMCs) are composed of at least two constituents: a metal matrix and the reinforcing particles, such as ceramic or organic compounds. **MMCs** can be classified according to the reinforcement to continuous (monofilament or multifilament) or discontinuous (particle, whisker, short fiber or other) strengthened alloys [42].

In general, the major advantages of Metal Matrix Composites (MMCs) are as follows [43]:

- Increased specific strength

- Increased specific stiffness
- Increased elevated temperature strength
- Improved wear resistance
- Lower density
- Improved damping capabilities
- Tailorable thermal expansion coefficients
- Good corrosion resistance

3 Finite Element Modeling

Finite element method (FEM) is the most powerful numerical technique for analyzing structural and mechanical problems and has become one of the most important and useful tools for scientists and engineers in recent years. The reliability of the numerical simulation results largely depends on the proper definition of the problem and careful control of the critical parameters.

3.1 Introduction to the Abaqus software

Abaqus has been developed by Hibbitt, Karrisson and Sorensoen, Inc. It was the first finite element program to introduce a gateway for researchers to add elements and materials models. Abaqus is a suit of engineering programs based on the finite element method, which can solve problems ranging from relatively simple linear analysis to challenging nonlinear simulations.

Abaqus CAE is an interactive, graphical environment for Abaqus. It is easily used to create or import geometries into meshable regions. Abaqus CAE contains very powerful options to mesh complex geometries and verify the resulting analysis model. Defining the material properties to the geometry, load applications, boundary conditions, and submitting the completed model for a job analysis can be done using Abaqus CAE. The visualization module can then be used to interpret the results. Abaqus consists of two main analysis modules: Abaqus/Standard and Abaqus/Explicit [46].

3.1.1 Abaqus/Standard and Abaqus/Explicit

Abaqus/Standard is a general-purpose analysis module used in solving a wide range of problems, both linear and nonlinear, involving the static, dynamic, thermal, and electrical response of components. It solves a system of equations implicitly at each solution "increment."

Abaqus/Explicit is a special-purpose analysis module that uses an explicit dynamic finite element formulation. It guides a solution forward through time in small intervals without solving a coupled system of equations at each increment. Abaqus/Explicit is suitable for modeling transient dynamic events, such as impact and blast problems, and also very efficient for highly nonlinear problems involving contact conditions, such as creating simulations [46].

3.2 Numerical model and simulation

The finite element program Abaqus/Explicit version 6.7-1 has been used to simulate the ballistic tests in this study. The numerical model consists of two parts created separately: a plate and a projectile.

The plate has been created in 2D with a 300 mm x 300 mm surface set as deformable solid structure. The surface was then extruded to a desired thickness (see Figure 3.1). The material properties including density, Young's modulus, and Poisson's ratio were defined for each material investigated in this research (see Table 3.2). The mesh was obtained by using 8-node linear brick elements (C3D8R) which offer reduced integration and hourglass control. The plate was partitioned to create an 80 mm diameter circle featuring a finer and denser mesh around the impact point (see Figure 3.5). In the Abaqus standard failure criteria method, a projectile velocity of 370 and a plate thickness of 10.7 mm were used for the convergence study. The mesh size was varied from 4 mm to 7 mm by changing the number of elements. The mesh sizes of 4 mm and 7 mm caused strong distortions at the impact point preventing convergence of the model to a final solution. The model coupled converges with the mesh size of 5 mm but the running duration was relatively long. Finally, the mesh size of 6 mm was found to provide an optimal combination of result accuracy and modeling time as can be seen in Table 3.1. Table 3.1 also shows results obtained for the different mesh sizes. A further reduction in mesh size below 6 mm does not improve the modeling results but rather leads to longer modeling durations and potential distortions. Therefore, a mesh size of 6 mm was used for all models for steels and the ceramic-metal matrix composites.

Table 3.1: Modeling with different meshing size

Velocity (m/s)	Mesh size (mm)	t (mm)
370	4	Distortion (error; a total of 4 excessively distorted elements)
370	5	≈ 10.7
370	6	≈ 10.7
370	7	Small penetration with distortion (error; a total of 4 excessively distorted elements)

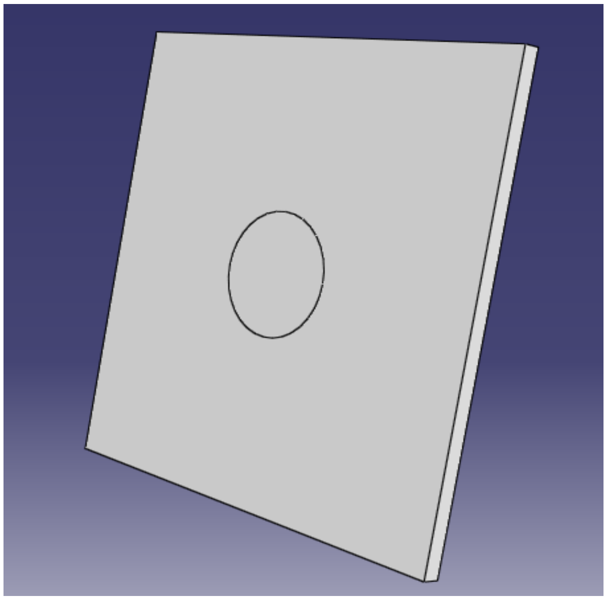

Figure 3.1: Plate model in 3D

AISI 450 stainless steel, Weldox 460 E and Weldox 700 E steels, as well as powder metallurgically manufactured metal matrix composites (CMMCs) 80wt%WC-20wt%Co and 2024Al-25wt%SiC are considered as target armor plates. Physical and mechanical properties are summarized in Table 3.2 [46, 47, 50].

Table 3.2: Physical and mechanical properties of target plates and projectiles used in this study

Material	AISI 450 stainless steel	WC-CO	Weldox 460 E steel,	Weldox 700 E steel	2024Al-SiC	WC Projectile	hardened steel projectile
Density, $\boldsymbol{\rho}$ (kg/m^3)	7800	13500	7850	7850	2800	15800	7850
Elastic modulus, E (GPa)	210	520	210	210	110	700	204
Poisson's ratio, v	0.3	0.24	0.33	0.33	0.3	0.24	0.33
Yield stress, σ_y (MPa)	814	3000	499	922	580	6000	1900
Elongation at break, el (%)	13.3	2	31	13	9	-	-

The 7.62x51 mm Armor Piercing (AP) (official NATO nomenclature 7.62 NATO) projectile is used [48]. It is a rifle cartridge developed in the 1950s as a standard for small arms among NATO countries. When loaded with a bullet design that expands, tumbles, or fragments in tissue, this cartridge is capable of delivering good terminal performance, including remote wounding effects known as hydrostatic shock [49].

An axial section of the projectile was sketched in 2D and revolved around its central axis to create the projectile 3D model as shown in Figure 3.4. The projectile was meshed using 4-node linear tetrahedron (C3D4) elements which proved to work most efficiently without severe distortions. A mesh size of 0.9 mm was used, yielding a total number of 5555 mesh elements (Figure 3.5).

Figure 3.2: The real 7.62 x 51 mm Armor Piercing projectile [56]

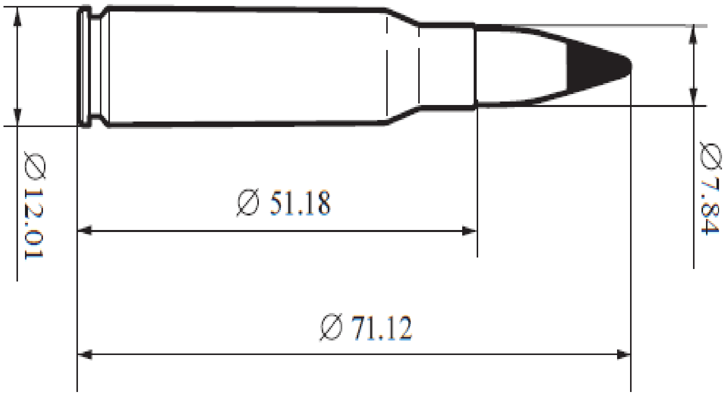

Figure 3.3: Dimensions of the 7.62x51 mm Armor Piercing projectile [50]

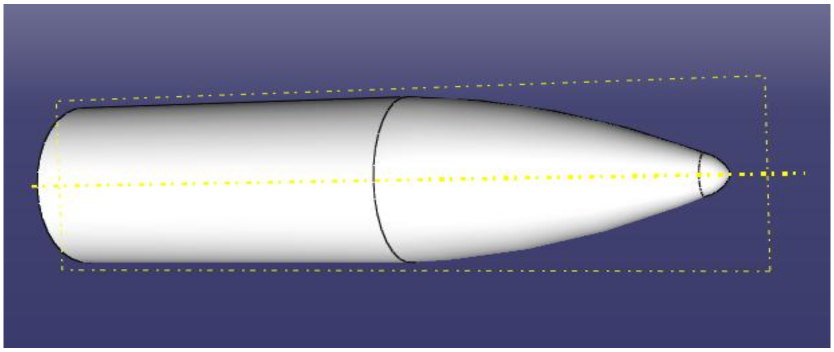

Figure 3.4: The 7.62x51 projectile model in 3D

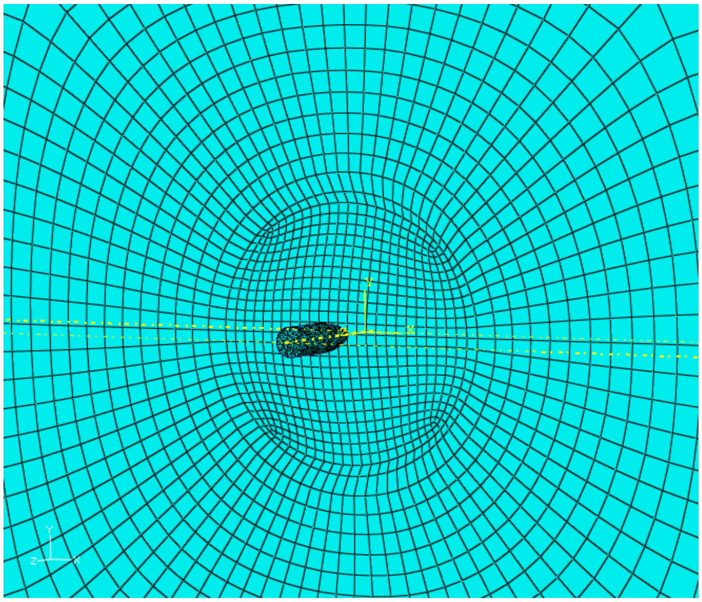

Figure 3.5: Meshed model of plate and projectile

The origin of the xyz coordinate system is at the center of back surface of the plate. The finer mesh in the projectile and around the impact point, as well as the coarser mesh in the rest of the plate can be seen.

The two model parts (projectile and plate/target) were assembled by creating a zero gap between them to reduce the running time of the job (see Figure 3.6). The contact interactions were defined as service to service contact, and then implemented in Abaqus/Explicit, which can describe the contact between deformable surfaces or between a deformable surface and a rigid body. The kinematic contact method was chosen for the mechanical constraint formulation. The explicit dynamic analysis was carried out for a total period of 1500 µs. The investigated range of initial projectile impact velocity was 350 to 400 m/s.

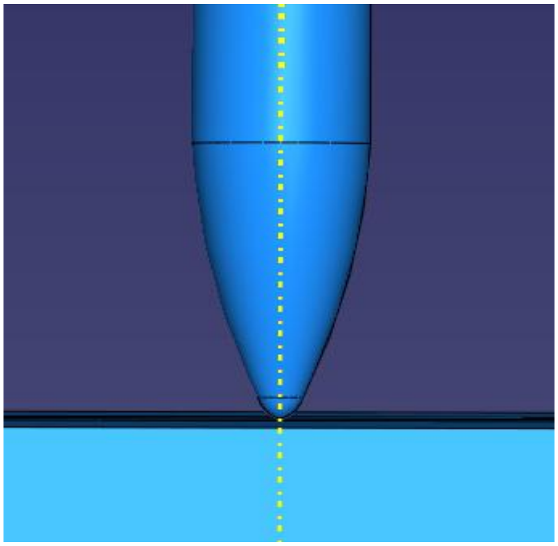

Figure 3.6: Initial assembly of projectile and plate/target with zero (0) gap

The plate was fixed along all four edges using the encastre boundary condition which constrains all degrees of freedom of edges as illustrated in Figure 3.7. The projectile was also constrained in all directions except in the impact direction normal to the plate surface (z-axis). The model was then submitted for analysis after defining required properties for each material investigated as discussed later in the thesis.

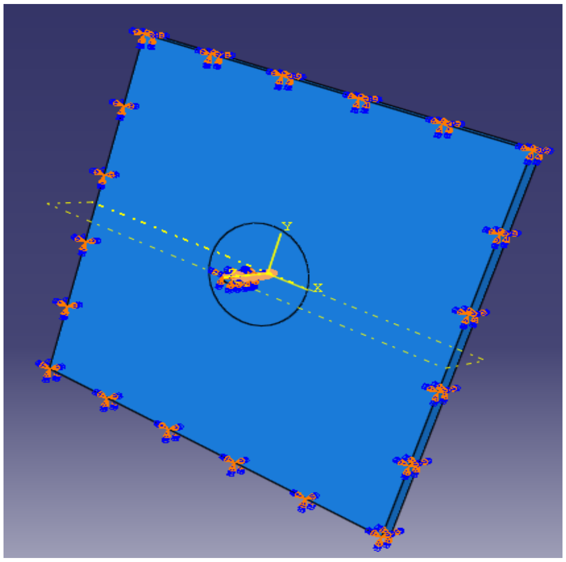

Figure 3.7: Boundary conditions applied in the model

3.3 Modeling with standard Abaqus ductile and shear failure criteria

The primary objective of using the Abaqus standard failure criteria model was to serve as a reference for the models with alternative failure conditions discussed in sub-section 3.5.

3.3.1 Progressive damage and failure

Abaqus offers a combination of multiple failure mechanisms acting simultaneously in a given material. Material failure refers to local or complete loss of load-carrying capacity that results from a progressive degradation of the material strength or stiffness. The degradation process is modeled using damage mechanics.

Figure 3.8 shows the stress-strain response of a typical metal specimen during a simple tensile test. It helps to understand the failure modeling methodology in Abaqus.

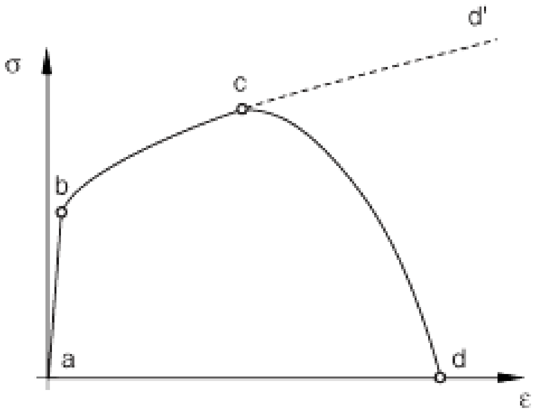

Figure 3.8: Typical uniaxial stress-strain response of a ductile metal specimen [46]

In Figure 3.8, *a-b* represents the linear elastic response of the material where the stress is directly proportional to the strain. This is followed by plastic yielding (*b-c*) generally featuring strain hardening. Beyond point *c* characterizing the material's ultimate tensile strength, the load-carrying capacity of the materials progressively falls (*c-d*) to zero at point *d* where rupture occurs. The damage initiation criterion is considered to be met, and damage is considered to start at point c where necking or cross sectional area reduction occurs. In the context of the damage mechanics, c-d can be viewed as degraded response of the curve *c-d'* that the material would have followed in the absence of necking and damage. Thus, the failure mechanism specification in Abaqus consists of four distinct parts based on Figure 3.8:

- the definition of the effective (or undamaged) material response (e.g., *a-b-c-d'*)
- a damage initiation criterion (e.g., *c*)
- a damage evolution law (e.g., *c-d*)
- and a choice of element deletion whereby elements can be removed from mesh and calculations once the local material stiffness or strength is fully degraded (e.g., *d*) [46].

3.3.2 Damage initiation criteria for the fracture of metals

There are two main mechanisms that can cause the fracture of a ductile metal: ductile fracture due to the nucleation, growth, and coalescence of voids; and shear fracture due to shear band localization. Based on phenomenological observations, these two mechanisms describe different forms of criteria for the onset of damage [46]. The ductile and shear criteria are fully defined in Abaqus and were set to be applied automatically in this study for the models called “with failure criterion”. They were applied solely to AISI 450 stainless steel targets since all required parameters [46] could be retrieved from existing literature in contrast to CMMCs for which most required data are unavailable.

3.3.2.1 Ductile criterion

The ductile criterion is specified by providing the equivalent plastic strain at the onset of ductile damage $\bar{\varepsilon}_{\mathrm{D}}^{pl}(\eta, \dot{\bar{\varepsilon}}^{pl})$, as a function of stress triaxiality (η) and strain rate $(\dot{\bar{\varepsilon}}^{pl})$.

With
$$\eta = -p/q \tag{3.1}$$

where p is the pressure stress and q is the von Mises equivalent stress. The criterion for damage initiation is met when the following condition is satisfied:

$$\omega_{\mathrm{D}} = \int \frac{\mathrm{d}\bar{\varepsilon}^{pl}}{\bar{\varepsilon}_{\mathrm{D}}^{pl}(\eta, \dot{\bar{\boldsymbol{\varepsilon}}}^{\boldsymbol{pl}})} = 1 \tag{3.2}$$

where ω_{D} is a state variable that increases monotonically with plastic deformation. At each increment during the analysis, the incremental increase in ω_{D} is computed as [46]

$$\Delta\omega_{\mathrm{D}} = \frac{\Delta\bar{\varepsilon}^{pl}}{\bar{\varepsilon}_{\mathrm{D}}^{pl}(\eta, \dot{\bar{\boldsymbol{\varepsilon}}}^{\boldsymbol{pl}})} \geq 0 \tag{3.3}$$

3.3.2.2 Shear criterion

The shear criterion is a phenomenological model for predicting the onset of damage due to shear band localization. The model assumes that the equivalent plastic strain at the onset of damage, $\bar{\varepsilon}_{\mathrm{S}}^{\mathrm{pl}}(\theta_s, \dot{\bar{\varepsilon}}^{pl})$, is a function of the shear stress ratio (θ_s) and strain rate $(\dot{\bar{\varepsilon}}^{pl})$.

With
$$\theta_s = (q + k_s p)/\tau_{max}, \tag{3.4}$$

where τ_{max} is the maximum shear stress, k_s is a material parameter, p and q are the pressure and the von Mises equivalent stresses respectively as defined previously. The criterion for damage initiation is met when the following condition is satisfied:

$$\omega_{\mathrm{s}} = \int \frac{\mathrm{d}\bar{\varepsilon}^{pl}}{\bar{\varepsilon}_{\mathrm{s}}^{pl}\,(\theta_s, \dot{\bar{\boldsymbol{\varepsilon}}}^{\boldsymbol{pl}})} = 1 \qquad (3.5)$$

where ω_{s} is a state variable that increases monotonically with plastic deformation. At each increment during the analysis, the incremental increase in ω_{s} is computed as [46]

$$\Delta\omega_{\mathrm{s}} = \frac{\Delta\bar{\varepsilon}^{pl}}{\bar{\varepsilon}_{\mathrm{s}}^{pl}\,(\theta_s, \dot{\bar{\boldsymbol{\varepsilon}}}^{\boldsymbol{pl}})} \geq 0 \qquad (3.6)$$

3.3.3 Damage evolution

Figure 3.9 illustrates the typical stress-strain behavior of a material undergoing damage. In the context of an elastic-plastic behavior with isotropic hardening, material damage can be characterized by a drop in either the yield strength or the elastic modulus. The solid curve in the Figure represents the damaged stress-strain response, while the dashed curve is the response in the absence of damage.

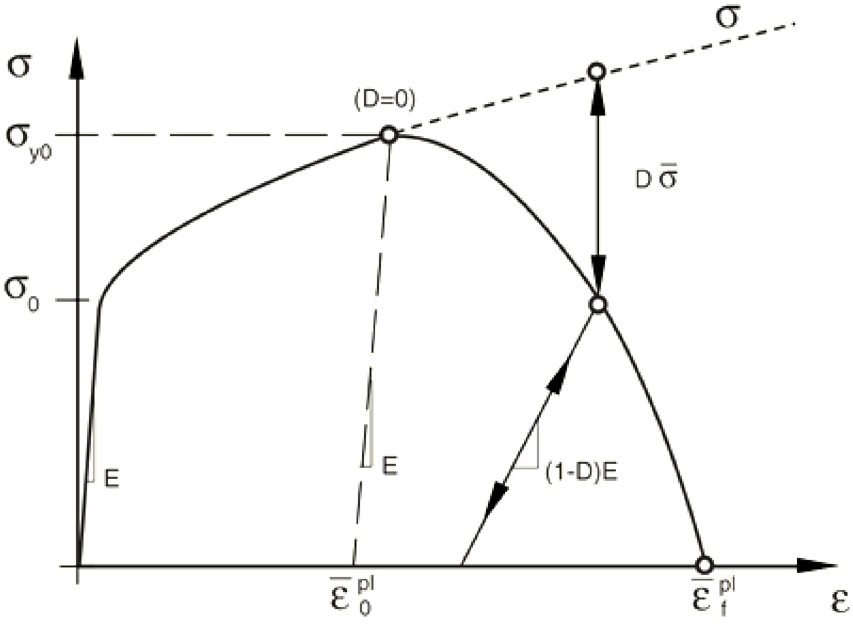

Figure 3.9: Stress-strain curve with progressive damage degradation [46]

In Figure 3.9 σ_{y0} and $\bar{\varepsilon}_0^{pl}$ are the yield stress and equivalent plastic strain at the onset of damage, $\bar{\varepsilon}_f^{pl}$ is the equivalent plastic strain at failure where the overall damage variable reaches the value $D_{\max}=1$.

$$\boldsymbol{\sigma} = (1-D)\,\bar{\sigma} \qquad (3.7)$$

Equation (3.7) is the scalar damage equation for the stress tensor in the material at any given time during the analysis; D is the overall damage variable and $\bar{\sigma}$ is the effective (or undamaged) stress tensor computed in the current increment. $\bar{\sigma}$ is the stress that would exist in the material in the absence of damage. The overall damage variable, D, captures the combined effect of all active damage mechanisms and is computed in terms of the individual damage variables, $d_{i,}$ for each mechanism. Abaqus can automatically remove elements as soon as their damage variable *D* reaches the maximum value of 1, which means the element has failed [46].

3.4 Modeling with alternative failure criteria

A large set of material parameters and properties is required for defining ductile and shear failure criteria standardly used in Abaqus. This requires exhaustive experimentation and testing as well as huge time and money investments. Therefore, required data are barely available for materials considered in armor applications. Specifically, no appropriate literature data could be found for ceramic-metal matrix composites. For this reason, alternative failure criteria are studied for which data can easily be obtained from the literature. The primary objectives of the alternative failure condition models are firstly to double check the accuracy of the model with Abaqus standard ductile and shear failure criteria as discussed in 3.3 using AISI 450 stainless steel as reference material. Secondly, they allow modeling of ceramic-metal matrix composites for which the Abaqus standard failure criteria model cannot be applied as a result of the lack in material properties and parameters required.

Similar to the Abaqus standard failure criteria models, an elastic-plastic material behavior is considered.

The plasticity model is then defined using the material density, the modulus of elasticity, the Poisson's ratio and the stress-strain behavior in the plastic region. The elastic strain is assumed negligible compared to the relatively large plastic deformation at fracture for ductile materials. In this study, Engineering or nominal stress and strain values obtained from uniaxial tests are converted into true stress and true strain values as follows [46]:

$$\sigma_{true} = \sigma_{nom}(1 + \varepsilon_{nom}) \qquad (3.8)$$

$$\varepsilon_{ln}^{pl} = \ln(1 + \varepsilon_{nom}) - \frac{\sigma_{true}}{E} \qquad (3.9)$$

where σ_{true} , σ_{nom} ,ε_{nom} , and ε_{ln}^{pl} are true stress, nominal stress, nominal strain, and true plastic strain respectively. Two alternatives were considered for defining plasticity: (1) real plasticity using stresses and strains from experimental stress-strain curves (Figure 3.10a); and (2) perfect plasticity in which the material is taken to be elastic up to the yield point and then behaves perfectly plastic with the material strength remaining constant for further increasing strains as in Figure 3.10.

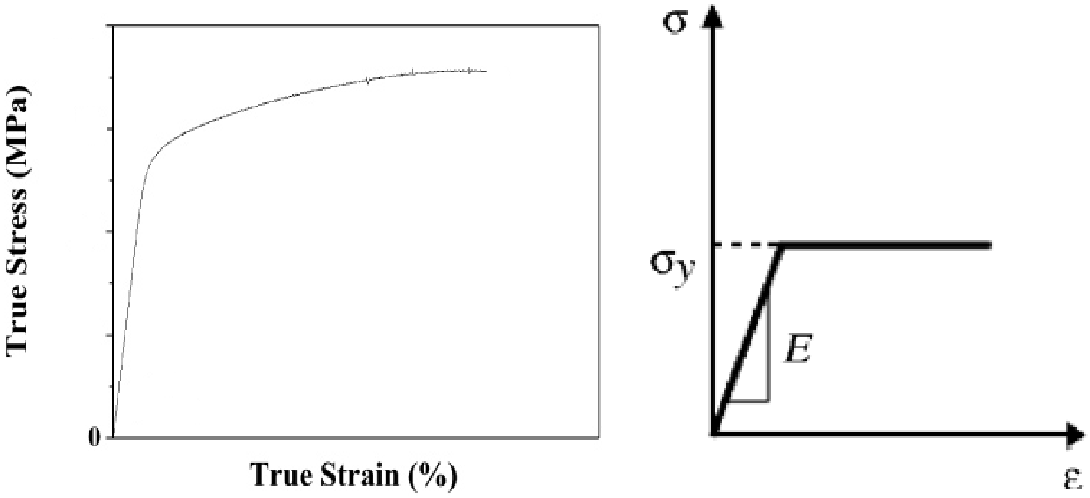

(a) (b)

Figure 3.10: Real plasticity with strain hardening (a) and perfect plasticity (b) curves considered in this study

Also, two alternative conditions are studied for defining failure or complete penetration (perforation) of the plate (target) by the projectile: (a) the maximum principal strain at the back surface of the plate reaches the elongation to fracture; and (b) the initial impact kinetic energy of the projectile is equal to the strain energy absorbable in the plate at fracture.

The energy obtained from Abaqus is the energy for the whole model and that will be seen in the result chapter for the kinetic and the strain energy. In Abaqus, the kinetic energy for the whole model is denoted as ALLKE and the strain energy for the whole model is denoted as ALLIE, where

ALLIE = ALLSE + ALLPD + ALLCD + ALLAE

Where ALLSE is the recoverable strain energy, ALLPD is the plastic dissipation energy, ALLCD is the energy dissipated by creep, viscoelasticity, and swelling, and ALLAE is the "artificial" strain energy [46].

3.4.1 Critical principal strain criterion

For this assumption, the kinetic energy of the projectile causes local deformation of the plate during impact. For complete penetration of the plate, the local strain shall exceed the elongation to fracture all along the projectile path through the plate as determined using the tensile stress-strain curve of the plate material. As the strain increases from the front impact surface to the back surface of the plate, the complete penetration condition is met when the deformation at the back surface, as the last point, equals the deformation to fracture. Therefore, the maximum principal strain for the back surface of the plate was obtained from the Abaqus model and compared with the elongation to fracture for each investigated plate thickness and projectile speed. The plate thickness for which the condition for perforation is met is considered to be the critical thickness below which penetration occurs, and above which the projectile would be stopped by the plate. The critical plate thickness is used to compare the different investigated materials, whereby materials with lower critical thicknesses are better, which means they better resist perforation. In addition, the critical thicknesses are used as parameter to compare and validate the different models and failure criteria.

3.4.2 Critical strain energy criterion

For this assumption, the impact kinetic energy of the projectile is transferred to the plate and absorbed in the form of strain energy. The projectile is considered to penetrate or perforate the plate if the kinetic energy exceeds the energy absorption capability of the plate. The critical thickness corresponds to the situation where the kinetic energy exactly equals the strain energy absorbed in the plate at fracture. To estimate the energy absorbable in the plate, the fracture energy by unit volume is multiplied by the effective deformation volume of the plate during impact. As a ballistic impact is a highly dynamic process, the deformation is strongly concentrated around the impact point, which means the effective deformation volume is much smaller than the total plate volume.

The kinetic energy (K_E) of the projectile of mass (m) moving with initial velocity (v) is given by

$$\mathrm{K_E} = \frac{1}{2}\ \mathrm{mv}^2 \qquad (3.10)$$

The energy absorbed in the plate per unit volume (u) can be obtained as in equation (3.11) as the area under the stress-strain curve of the material of the plate up to the fracture strain (ε_f) at the point of failure (B or B'**;** see Figure 3.11) [2].

$$u = \int_0^{\varepsilon_f} \sigma \, d\varepsilon \qquad (3.11)$$

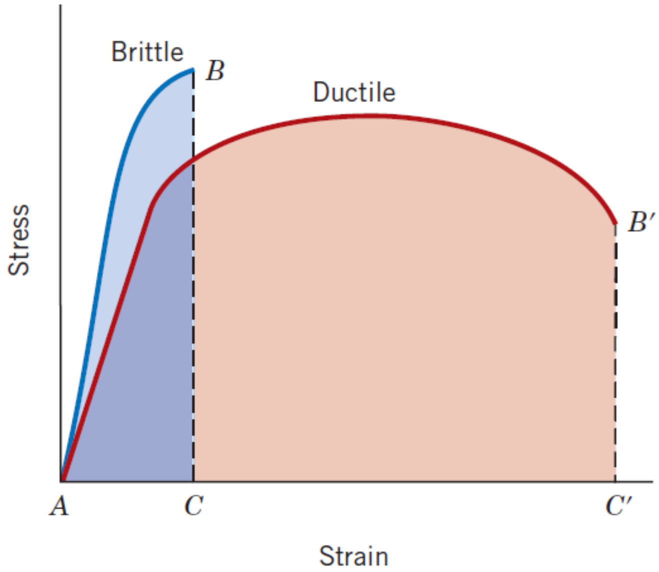

Figure 3.11: Stress-strain curves for brittle and ductile materials. The colored area below the curve represents the strain energy per unit volume at fracture [2]

The effective deformation volume is assumed to have the shape of a cone (see Figure 3.12). The front and rear circular surfaces of the cone are considered to cover all Abaqus nodes, on the front and back plate surfaces respectively, for which the von Mises stress is equal to or larger than the yield strength as illustrated in Figure 3.13.

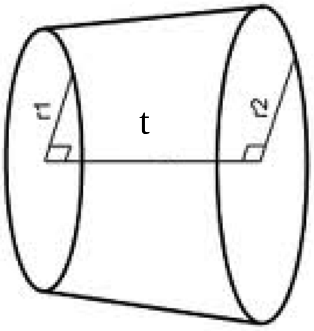

Figure 3.12: Cone representing the effective deformation volume of the plate during impact

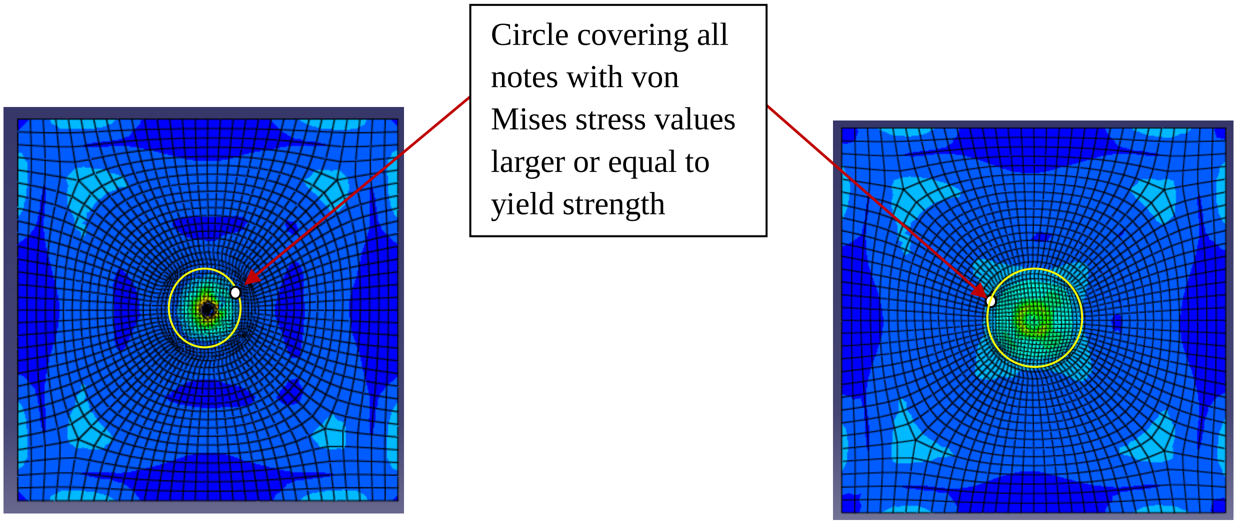

Circle covering all notes with von Mises stress values larger or equal to yield strength

a) Front surface (r_1)

b) Back surface

Figure 3.13: Front (a) and back (b) circular surfaces of the effective deformation cone volume

The effective impact volume can then be calculated as the volume of the cone (V_c) according to:

$$V_c = \frac{1}{3}\pi t(r_1^2 + r_1 r_2 + r_2^2) \qquad (3.12)$$

Where, r_1 is the radius of the front cone face, r_2 is the radius of the back cone face, and t is the thickness of the plate.

As discussed earlier, perforation of the plate by the projectile occurs when the initial impact kinetic energy of the projectile is equal to the strain energy absorbed at failure as:

$$\mathrm{K_E} = u * \mathrm{V_c} \tag{3.13}$$

or

$$\frac{1}{2}mv^2 = u * \frac{1}{3}\pi t(r_1^2 + r_1 r_2 + r_2^2) \tag{3.14}$$

For given material and projectile velocity, the critical plate thickness for perforation is then calculated by solving equation (3.14) as:

$$t = \frac{3mv^2}{2u*\pi(r_1^2+r_1r_2+r_2^2)} \tag{3.15}$$

3.5 Material definitions

In this study, the ballistic performance of AISI 450 stainless steel is investigated using Abaqus/explicit at different impact speeds from 350 – 400 m/s and the progressive damage criteria (ductile and shear failure criteria) which are standard in Abaqus. In addition, the ballistic performance of AISI 450 stainless steel, WC-CO, Weldox 460 E steel, Weldox 700 E steel, and 2024Al-SiC are investigated using critical back surface deformation and strain energy as alternative failure criteria. For WC-CO, the true stress strain curve from the literature [51] and the perfectly plastic curve in Figure 3.16 and 3.17 respectively, are used to define the plasticity part in Abaqus.

The real elastic-plastic and perfectly elastic-plastic curves of all investigated materials are shown in the following Figures 3.14 to 3.19.

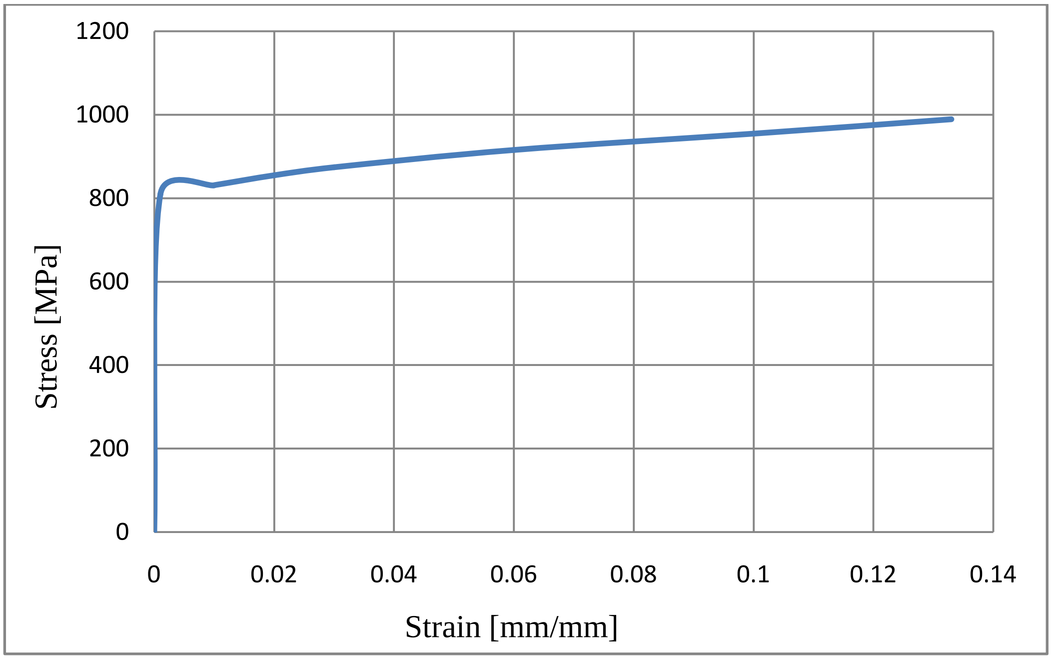

Figure 3.14: Experimental stress-strain curve of AISI 450 stainless steel with strain hardening [46]

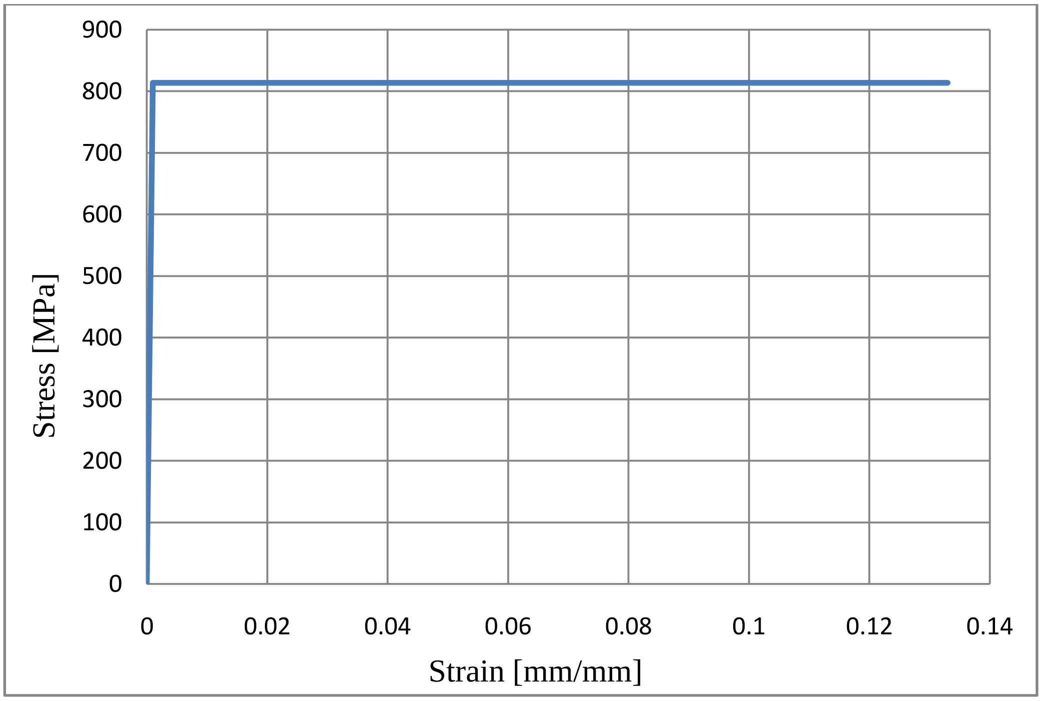

Figure 3.15: Perfectly elastic-plastic stress-strain curve for AISI 450 stainless steel

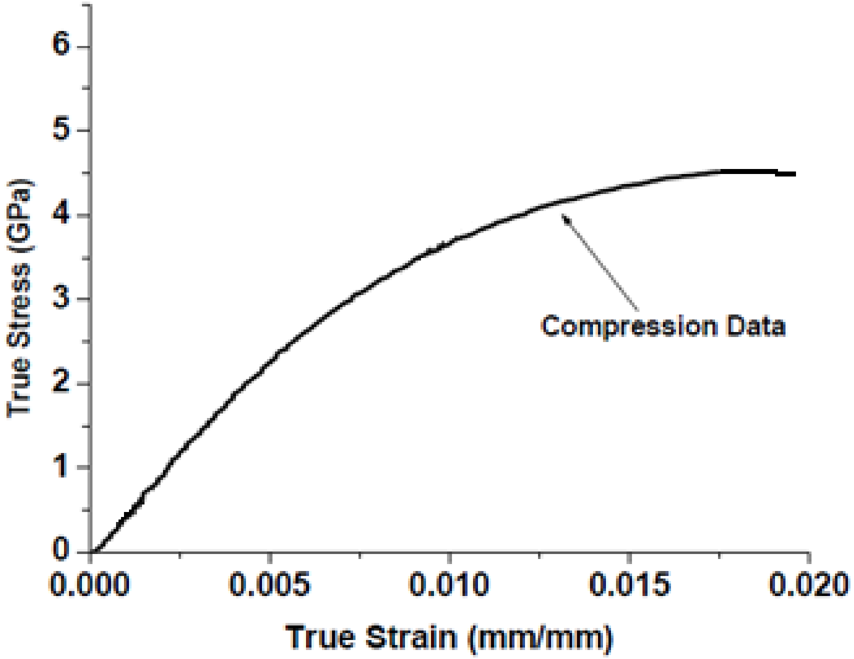

Figure 3.16: True stress-strain curve of WC-CO [51]

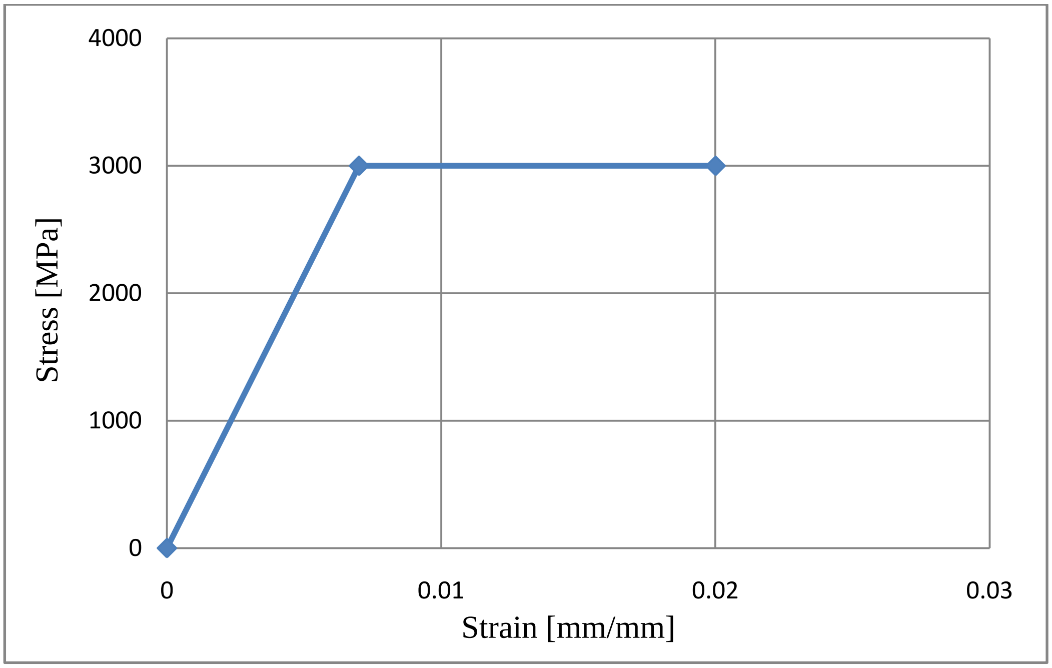

Figure 3.17: Perfectly elastic-plastic stress-strain curve for WC-CO

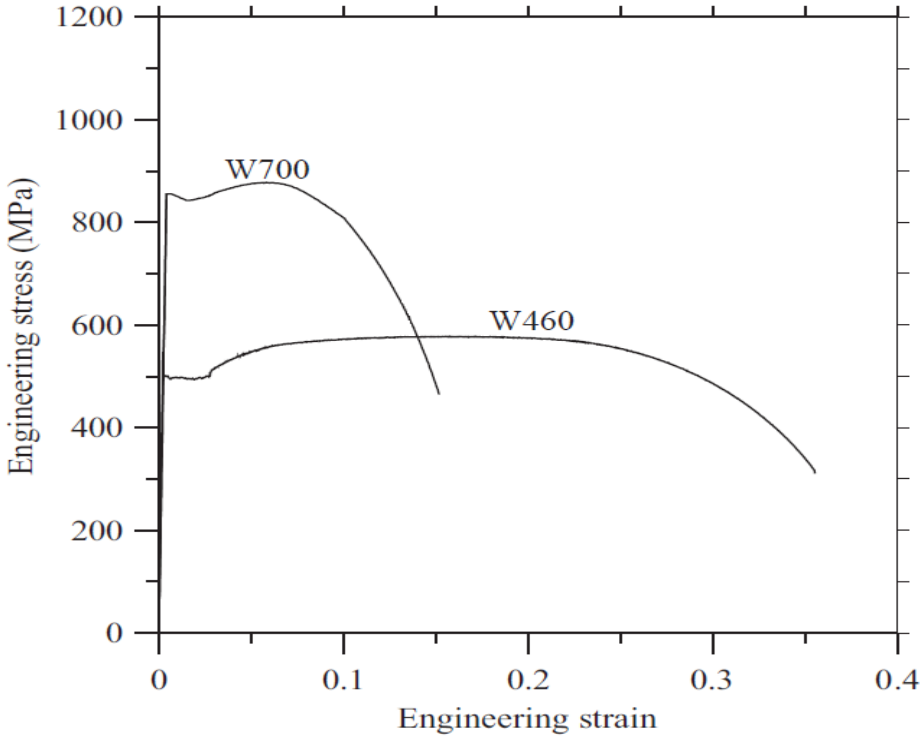

Figure 3.18: Engineering stress–strain curves for Weldox 460 E and Weldox 700 E [52]

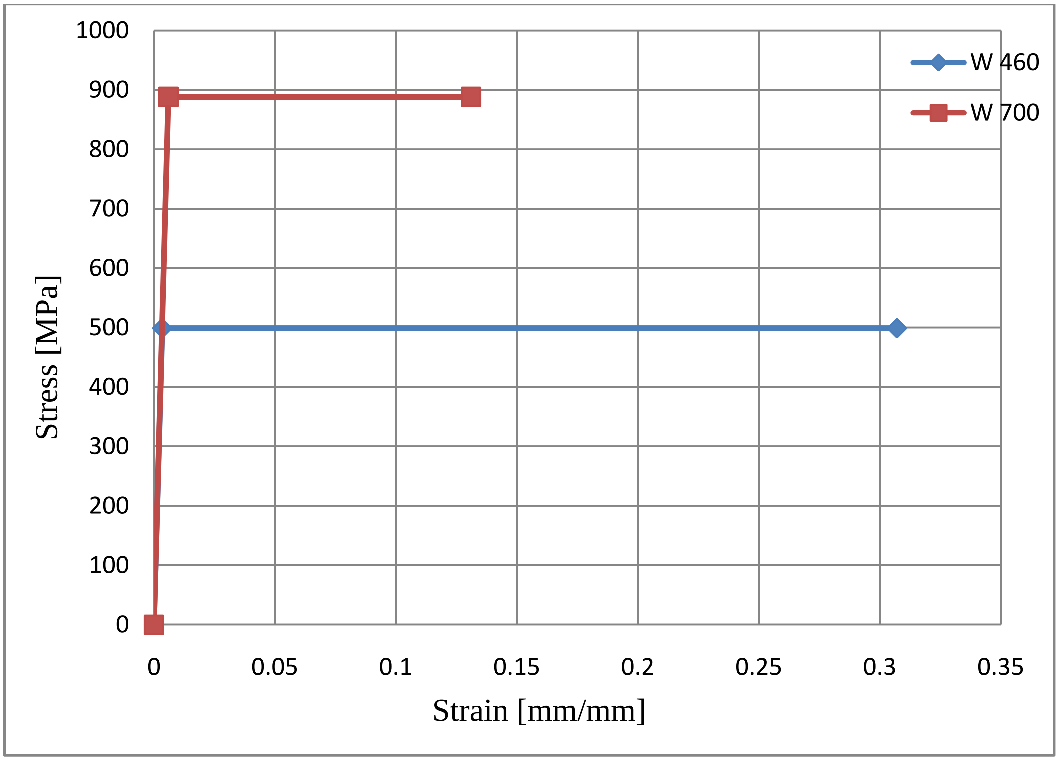

Figure 3.19: Perfectly elastic-plastic stress-strain curves for Weldox 460 E and Weldox 700 E

4 Results

Critical thicknesses for the penetration of AISI 450 stainless steel impacted by a 7.62x51mm tungsten carbide projectile, and Weldox 460 E and Weldox 700 E steels impacted by a hardened steel projectile with a nominal mass and diameter of 197 g and 20 mm respectively, are determined numerically. In addition, critical thicknesses for the penetration of CMMCs including WC-CO impacted by a 7.62x51mm tungsten carbide projectile and 2024Al-SiC impacted by a 50 caliber bullet are found numerically.

The ballistic impact of AISI 450 stainless steel is modeled using standard Abaqus ductile and shears failure criteria, as well as alternative failure conditions. This allows comparing the different models.

Figures 4.1 a to f show the simulated progression of the penetration of a 9.9 mm AISI 450 stainless steel plate struck by a 7.62x51 mm hard tungsten carbide projectile at a velocity of 360 m/s using standard Abaqus ductile and shears failure criteria. In addition, the von Mises stress distributions for the plate and the projectile are shown in Figure 4.1.

a

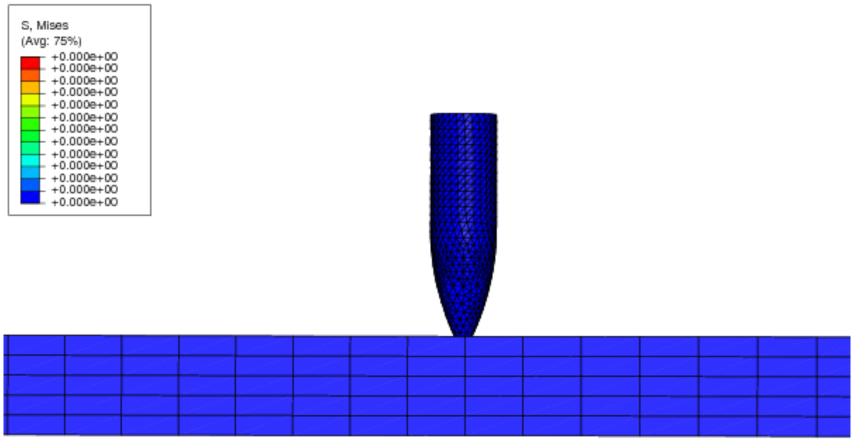

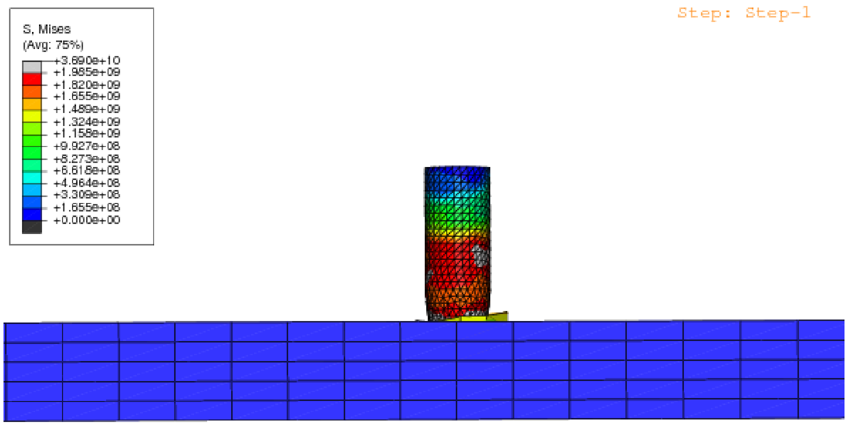
S, Mises
(Avg: 75%)
+3.690e+10
+1.985e+09
+1.820e+09
+1.655e+09
+1.489e+09
+1.324e+09
+1.158e+09
+9.927e+08
+8.273e+08
+6.618e+08
+4.964e+08
+3.309e+08
+1.655e+08
+0.000e+00
Step: Step-1

b

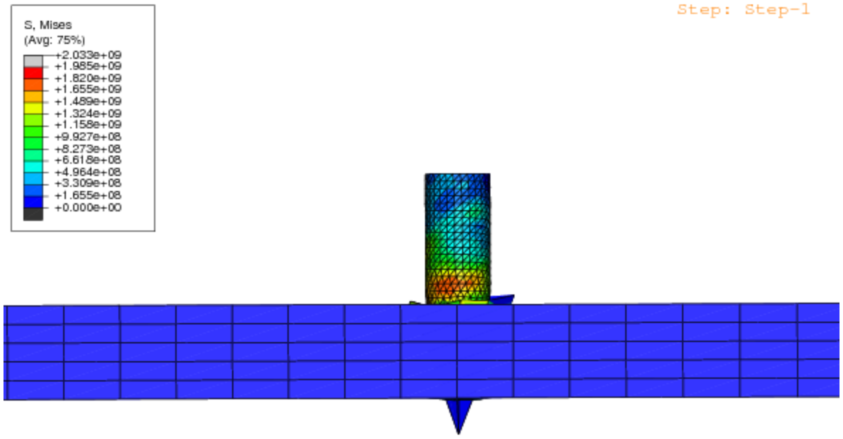
S, Mises
(Avg: 75%)
+2.033e+09
+1.985e+09
+1.820e+09
+1.655e+09
+1.489e+09
+1.324e+09
+1.158e+09
+9.927e+08
+8.273e+08
+6.618e+08
+4.964e+08
+3.309e+08
+1.655e+08
+0.000e+00
Step: Step-1

c

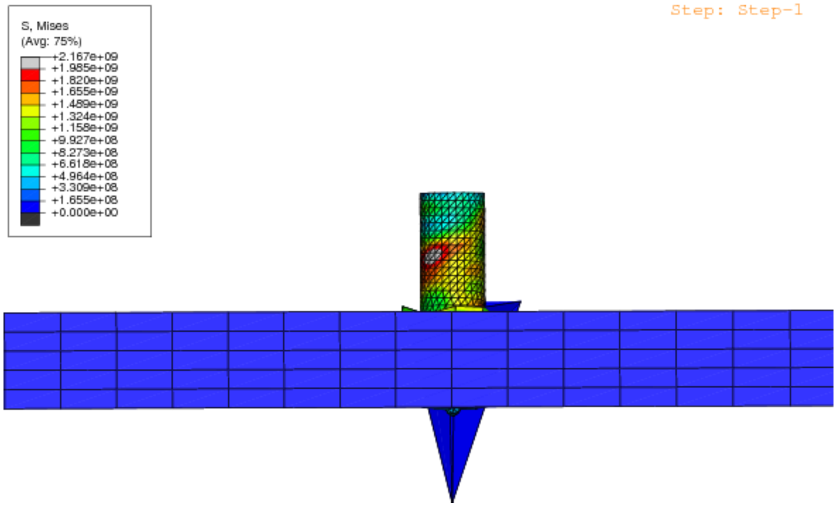
S, Mises
(Avg: 75%)
+2.167e+09
+1.985e+09
+1.820e+09
+1.655e+09
+1.489e+09
+1.324e+09
+1.158e+09
+9.927e+08
+8.273e+08
+6.618e+08
+4.964e+08
+3.309e+08
+1.655e+08
+0.000e+00
Step: Step-1

d

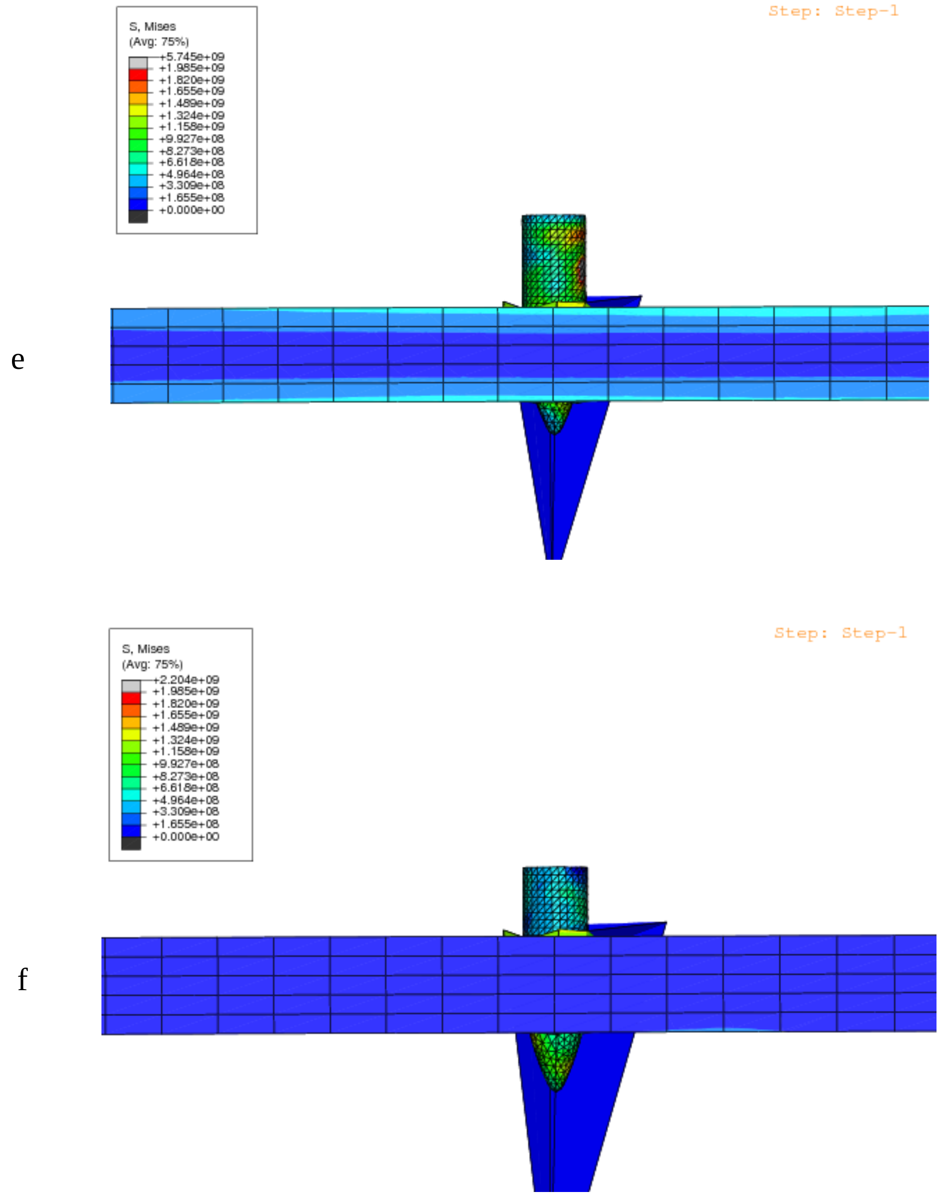

Figure 4.1: Penetration simulation of a 7.62x51mm hard tungsten carbide projectile with an impact velocity of 360 m/s through a 9.9 mm thick AISI 450 stainless steel plate

As seen in Figure 4.2, the kinetic energy of the whole system decreases rapidly during impact, while the strain energy increases. For this case, the kinetic energy of the projectile exceeded the strain energy absorption capacity of the plate, i.e. the plate fails and there is a remaining kinetic energy of the projectile after impact as seen in Figure 4.3: the projectile penetrates or perforates the plate.

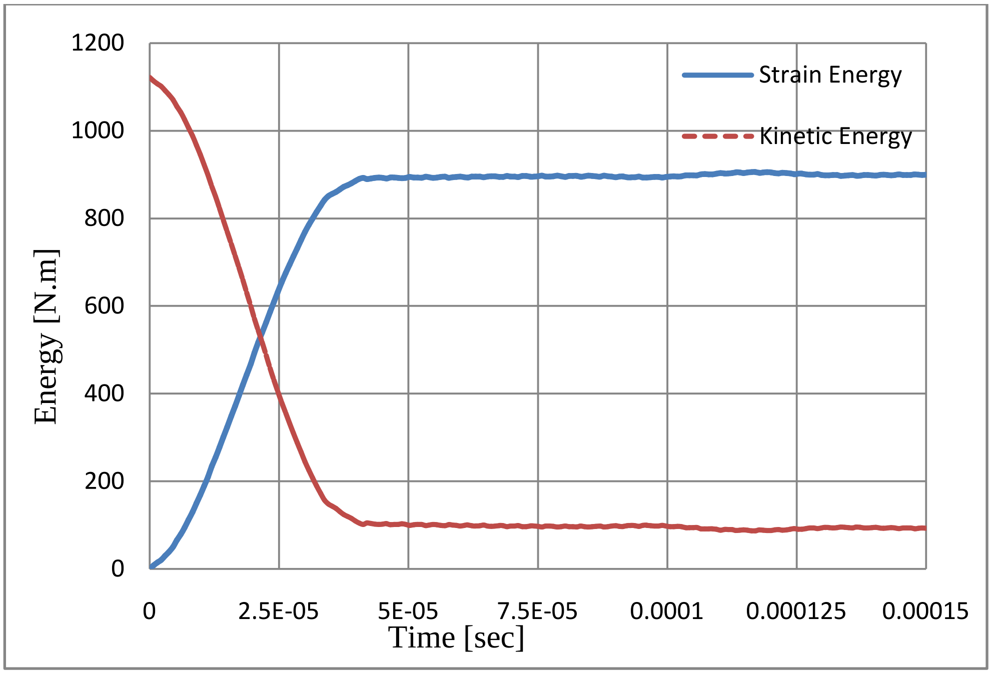

Figure 4.2: Kinetic and strain energy for the whole model changes during impact of a 9.9 mm thick AISI steel plate by a 7.62x51mm hard tungsten carbide projectile at a velocity of 360 m/s

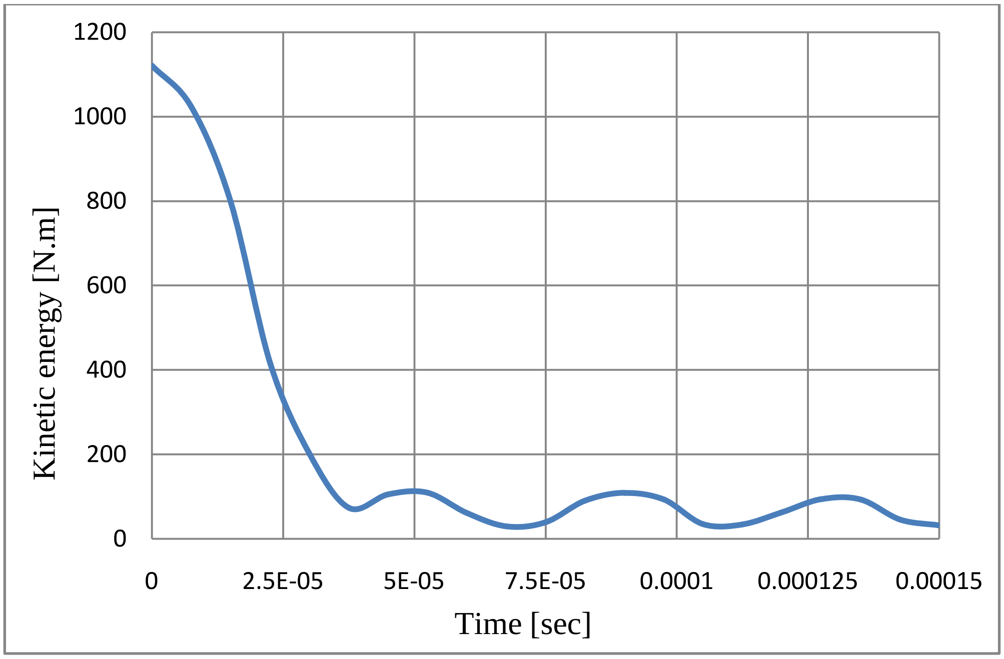

Figure 4.3: The kinetic energy of the projectile during the impact of a 9.9 mm thick AISI steel plate at 360 m/sec

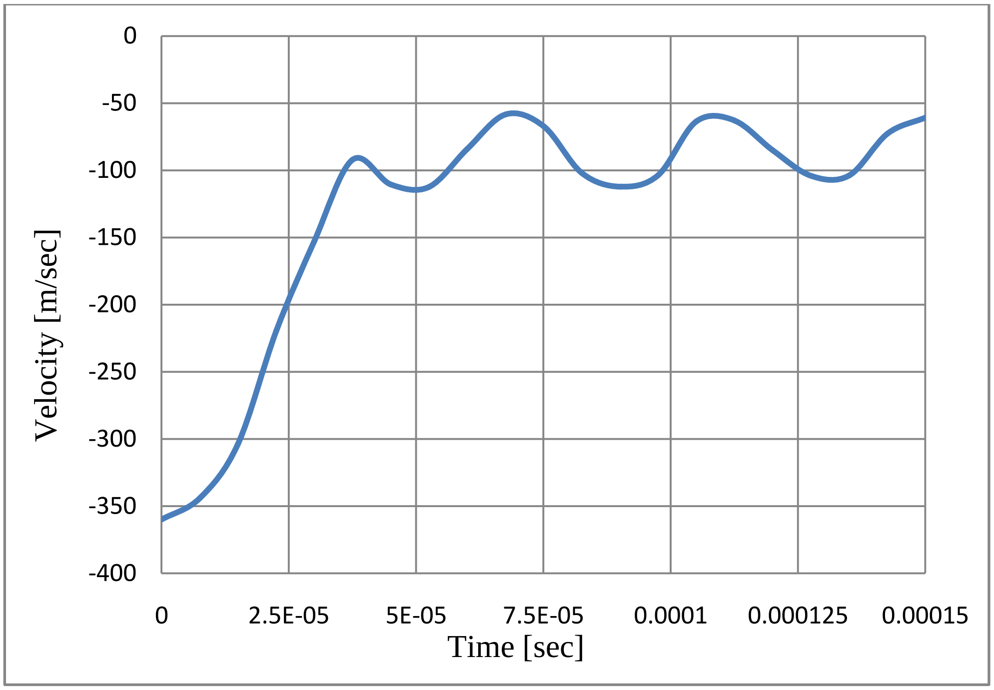

Figure 4.4: The velocity of the projectile during the impact of a 9.9 mm thick AISI steel plate at 360 m/sec

In contrast, for the case of an initial projectile velocity of 340m/s, the kinetic energy of the projectile is completely transformed into the strain energy of the plate and drops to zero during impact, meaning that the projectile is completely stopped by the plate and does not penetrate as seen in Figure 4.6. The penetration speed for a 9.9 mm thick plate of AISI 450 stainless steel is then determined to be 360 m/s. On the other hand, the deformation in the back surface of the plate increases with the impact velocity of the projectile.

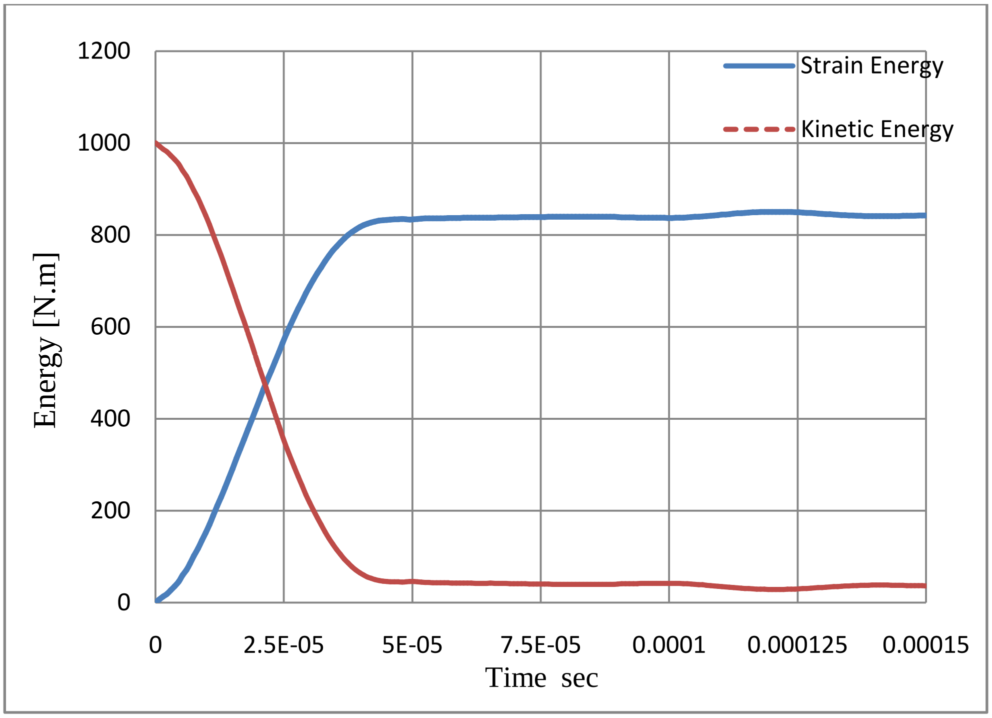

Figure 4.5: Kinetic and strain energy for the whole model changes during impact of a 9.9 mm thick AISI steel plate by a 7.62x51 mm hard tungsten carbide projectile with an impact velocity of 340 m/s

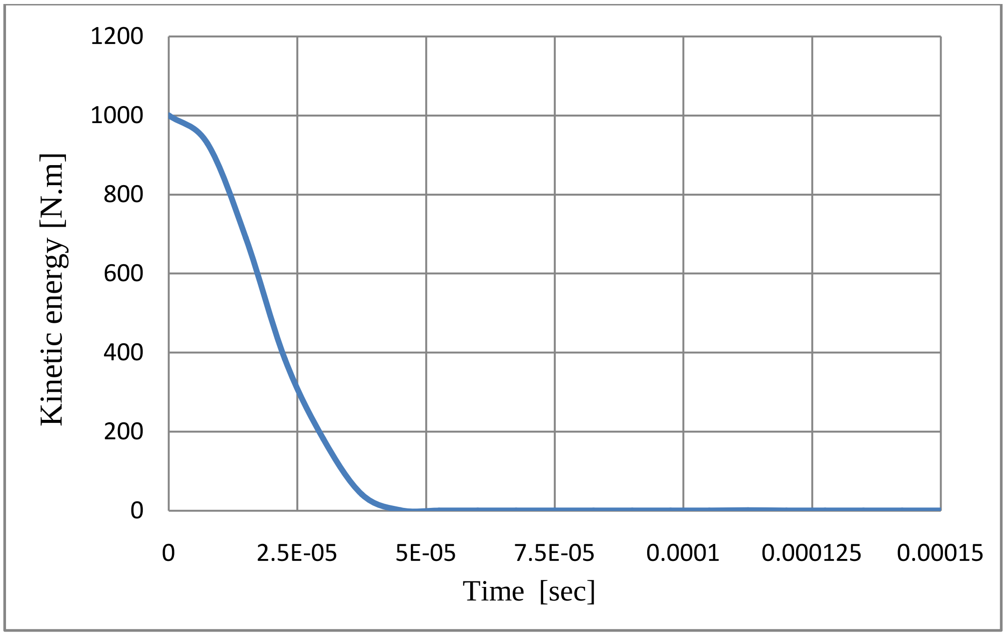

Figure 4.6: The kinetic energy of the projectile during the impact of a 9.9 mm thick AISI steel plate at 340 m/sec

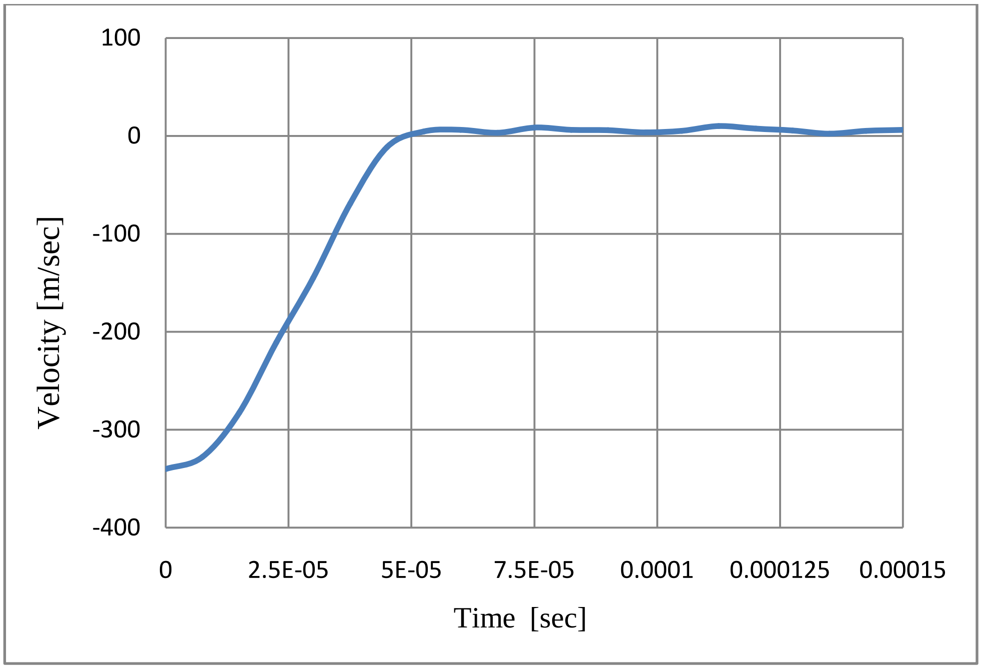

Figure 4.7: The velocity of the projectile during the impact of a 9.9 mm thick AISI steel plate at 340 m/sec

Figure 4.8 shows the deformation at the back surface of an 8.7 mm thick AISI steel plate struck by a 7.62x51mm hard tungsten carbide projectile with an impact velocity of 360 m/s for the real elastic-plasticity material behaviour. The von Mises stress distributions in the plate and the projectile are also shown. As expected, the back surface deformation increased with increasing projectile impact velocity in the investigated range from 340 to 400 m/s.

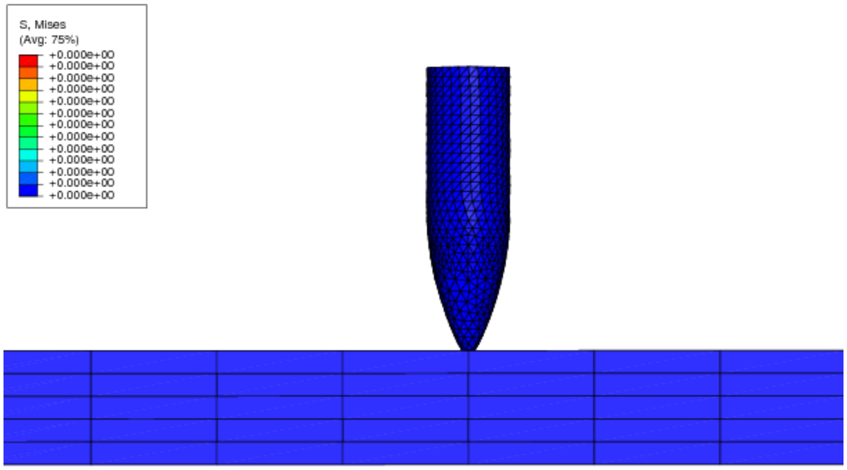
S, Mises
(Avg: 75%)
+0.000e+00
+0.000e+00
+0.000e+00
+0.000e+00
+0.000e+00
+0.000e+00
+0.000e+00
+0.000e+00
+0.000e+00
+0.000e+00
+0.000e+00
+0.000e+00
+0.000e+00

a

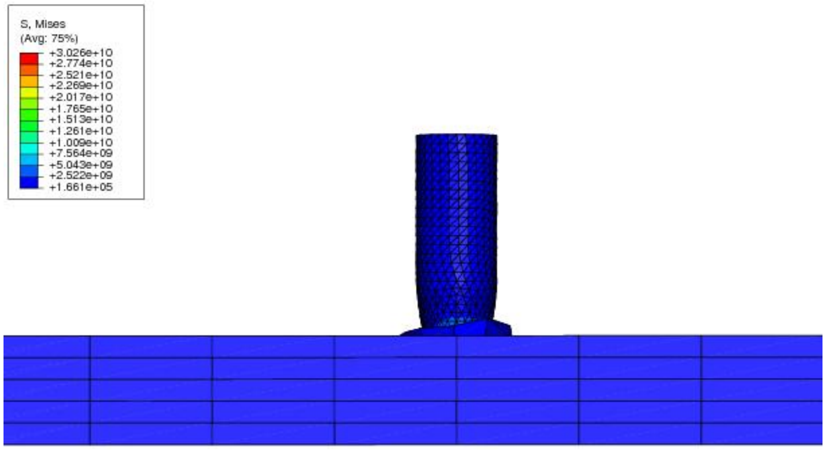
S, Mises
(Avg: 75%)
+3.026e+10
+2.774e+10
+2.521e+10
+2.269e+10
+2.017e+10
+1.765e+10
+1.513e+10
+1.261e+10
+1.009e+10
+7.564e+09
+5.043e+09
+2.522e+09
+1.661e+05

b

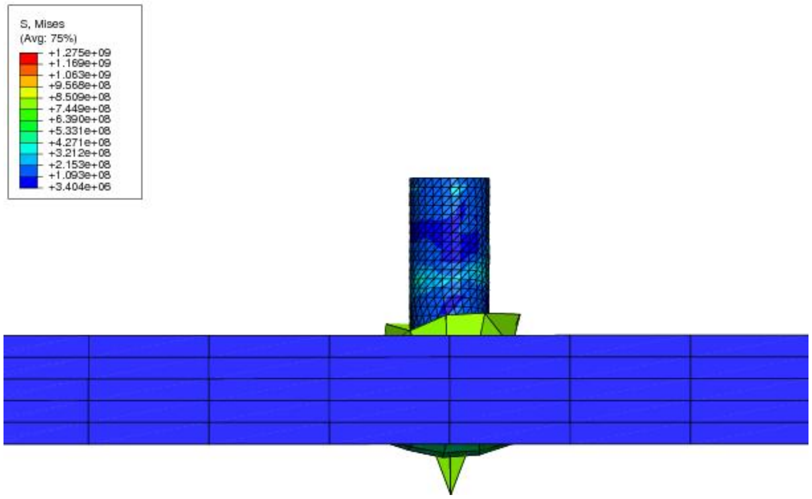
S, Mises
(Avg: 75%)
+1.275e+09
+1.169e+09
+1.063e+09
+9.568e+08
+8.509e+08
+7.449e+08
+6.390e+08
+5.331e+08
+4.271e+08
+3.212e+08
+2.153e+08
+1.093e+08
+3.404e+06

c

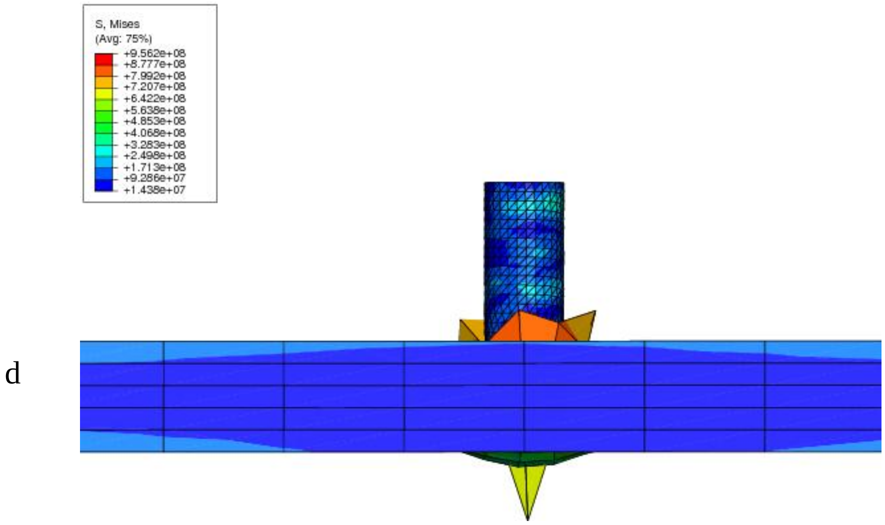

Figure 4.8: Deformation progression at the back surface of an 8.7 mm thick AISI plate struck by a 7.62x51mm hard tungsten carbide projectile with an impact velocity of 360 m/s

Figure 4.9 shows the kinetic and strain energy for the whole model during impact of an 8.7 mm thick AISI 450 stainless steel plate struck by a 7.62x51mm hard tungsten carbide projectile at a velocity of 360 m/s for the real elastic-plasticity material behaviour, and Figure 4.10 illustrates that the kinetic energy of a 7.62x51mm hard tungsten carbide projectile with an impact velocity of 360 m/s is completely transformed into the strain energy of an 8.7 mm thick AISI target plate. The kinetic energy then ultimately drops to zero towards the end of the impact process, meaning that the projectile is stopped and does not penetrate the plate.

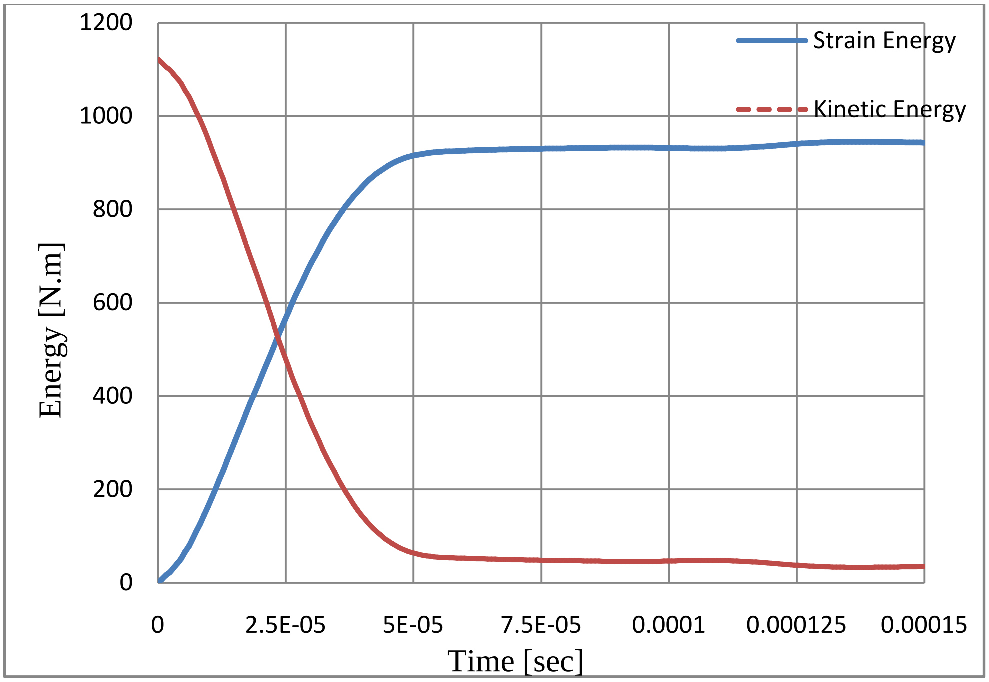

Figure 4.9: Kinetic and strain energy for the whole model changes during impact of an 8.7 mm thick AISI 450 stainless steel plate by a 7.62x51 mm hard tungsten carbide projectile at a velocity of 360 m/s

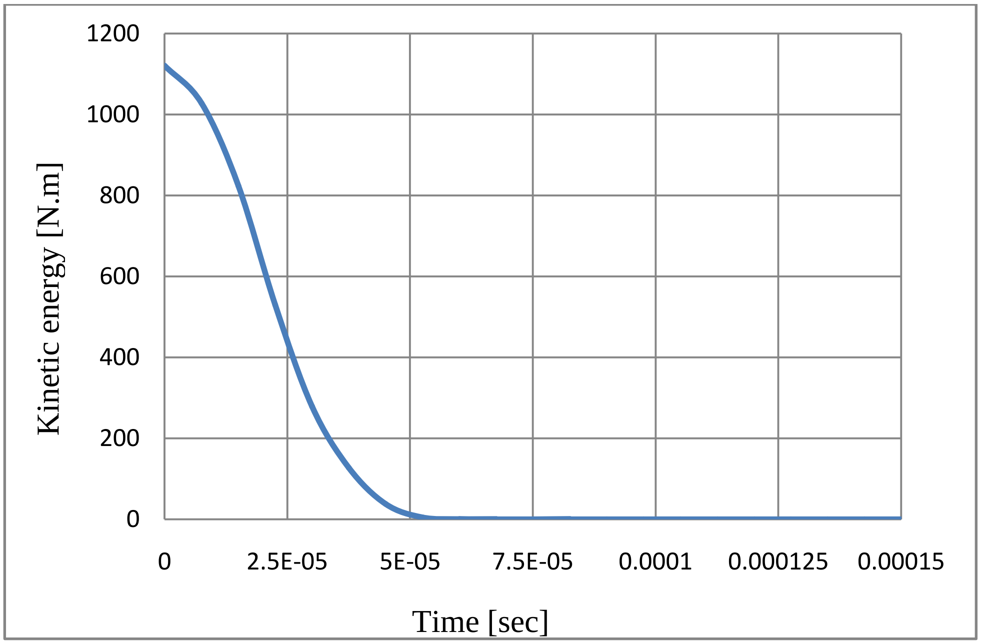

Figure 4.10: the kinetic energy of the projectile during the impact of an 8.7 mm thick AISI 450 stainless steel plate at 360 m/sec

The critical thicknesses for penetration of AISI 450 stainless steel plates by a 7.62x51mm hard tungsten carbide projectile for different projectile velocities as determined using the different models are summarized in Table 4.1. As expected, the critical thicknesses increased with increasing impact speed as more energy needs to be absorbed by the plate.

Table 4.1: Critical thicknesses for perforation of AISI 450 stainless steel plates by a 7.62x51mm hard tungsten carbide projectile for different projectile velocities and models

	With standard F.C.	With critical back surface deformation criterion	
Velocity v m/s	t	t R-P* curve	t P-P* curve
350	9	8.4	8.9
360	9.9	8.7	9.2
370	10.7	9	9.4
400	12.8	9.9	9.9

* R-P: Real plasticity; P-P: perfect plasticity

Figure 4.11 shows that the thicknesses of AISI 450 stainless steel with standard failure criteria are greater than the thicknesses obtained with the local deformation at fracture as failure criterion.

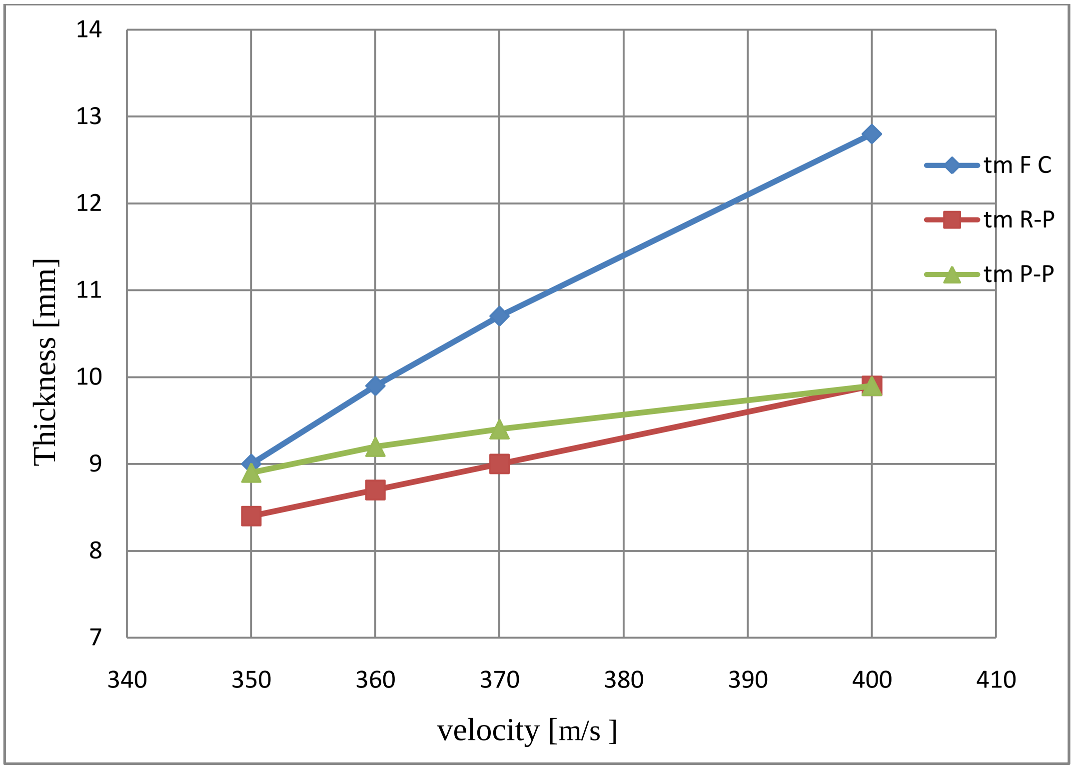

Figure 4.11: Dependence of the critical thicknesses for perforation of AISI 450 stainless steel plates on projectile speed as determined using models with standard ductile and shear criteria, as well as with the elongation to fracture criterion

The maximum deformations at the back surface of the AISI 450 stainless steel upon impact at different impact speeds are summarised in Figure 4.12 for the real elastic-plastic material behaviour. As expected, the deformation increases with increasing impact velocity.

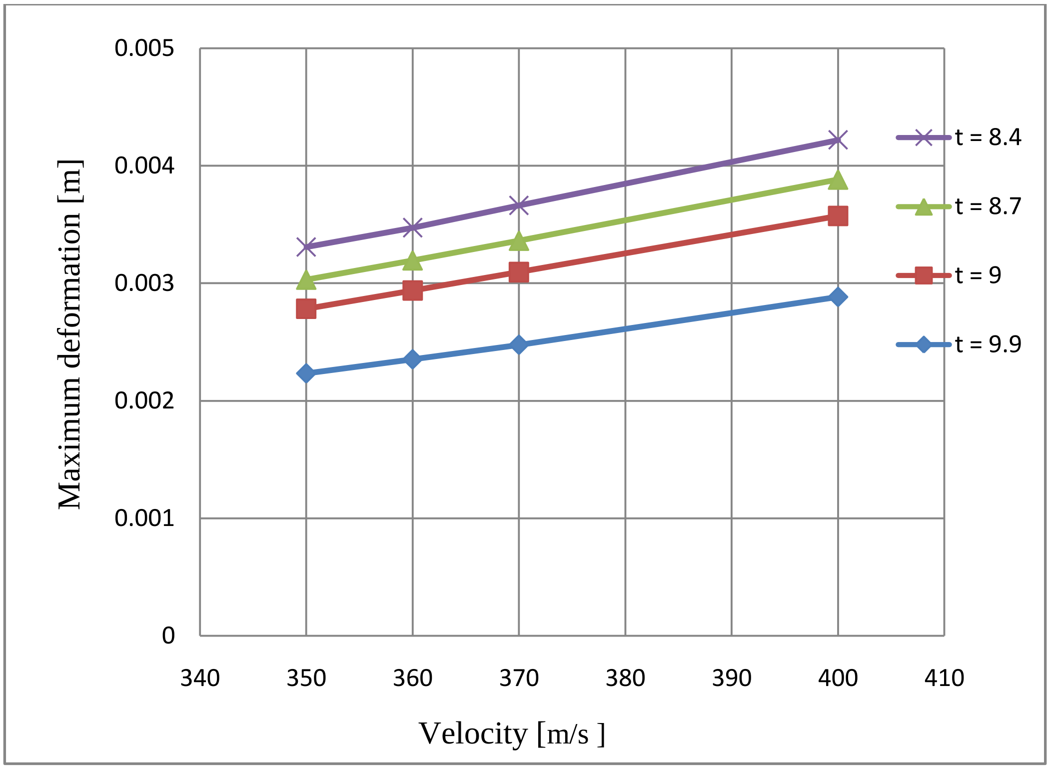

Figure 4.12: Maximum deformation at the back surface of AISI 450 stainless steel targets versus impact velocity

Critical thicknesses for the penetration of WC-CO composite plate impacted by a 7.62x51mm tungsten carbide projectile at different projectile speeds using the elongation to fracture failure criterion and either the perfectly (P-P) or the real elastic-plastic (R-P) material behaviour are summarized in Table 4.2 and in Figure 4.13.

Table 4.2: Critical thicknesses for perforation of WC-CO composite impacted by a 7.62x51mm hard tungsten carbide projectile for different projectile impact velocities using Abaqus with the elongation to fracture failure criterion

Velocity v [m/s]	t [mm] R-P curve	t [mm] P-P curve
350	8.7	9.4
360	9	9.6
370	9.2	9.9
400	9.7	10.4

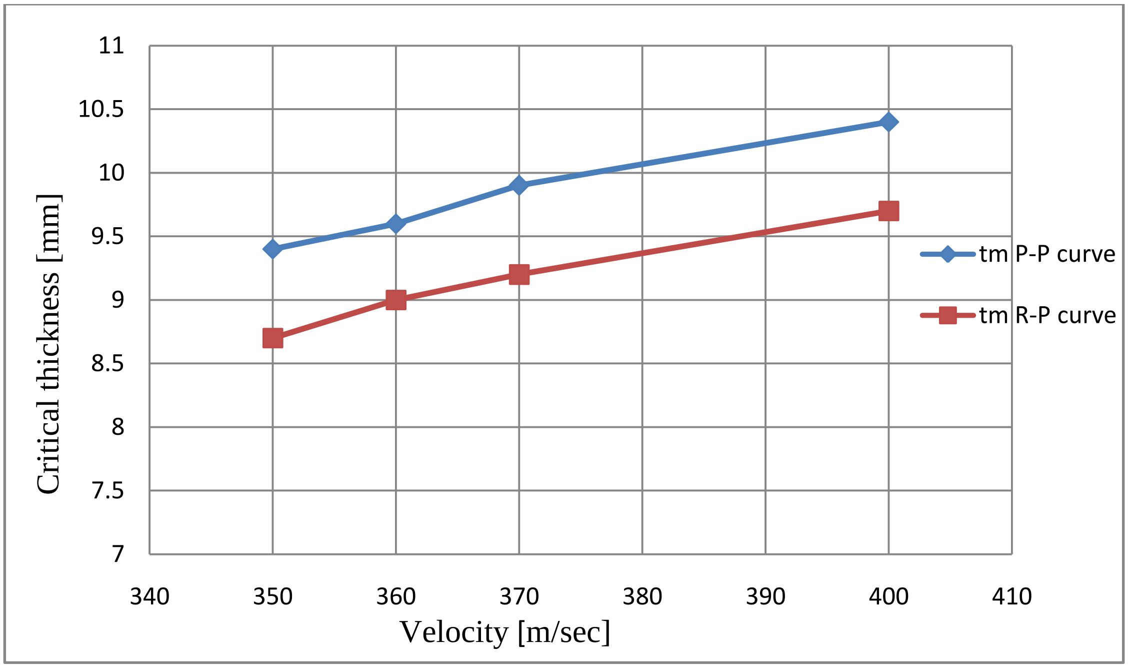

Figure 4.13: Dependence of the critical thickness for perforation of WC-CO plates on projectile speed as determined using the elongation to fracture failure criterion

Figure 4.14 shows the deformation at the back surface of a 9.7 mm thick WC-CO plate struck by a 7.62x51mm hard tungsten carbide projectile with an impact velocity of 400 m/s using real plasticity material behaviour. The von Mises stress distributions in the plate and the projectile are also shown.

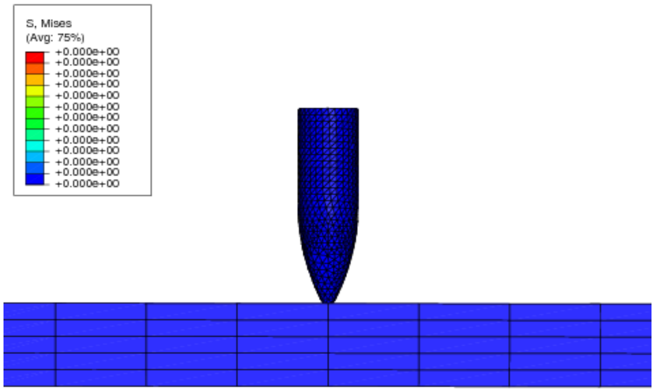

a

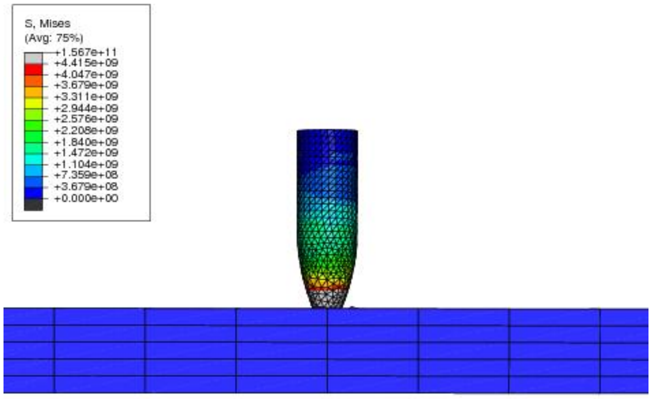

b

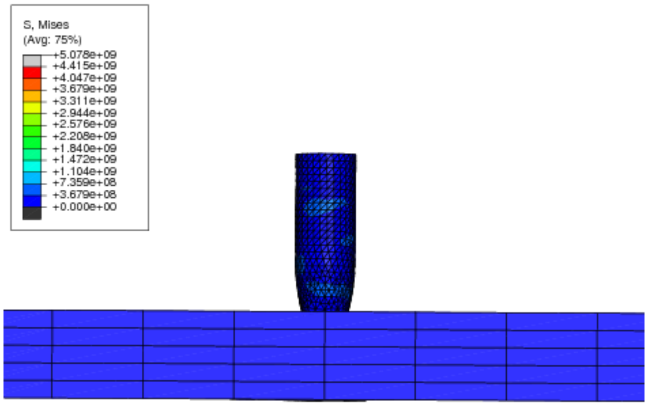

c

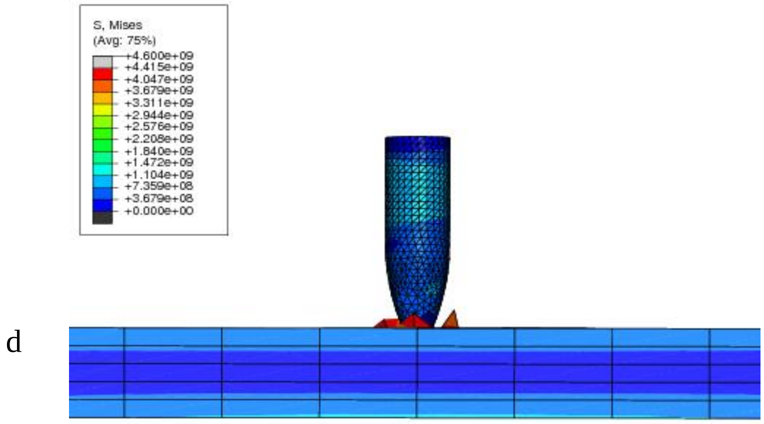

Figure 4.14: Deformation progression at the back surface of a 9.7 mm thick WC-CO plate struck by a 7.62x51 mm hard tungsten carbide projectile with an impact velocity of 400 m/s

The maximum deformations of the back surface for different thicknesses of WC-CO plate for different impact speeds are given in Figure 4.15.

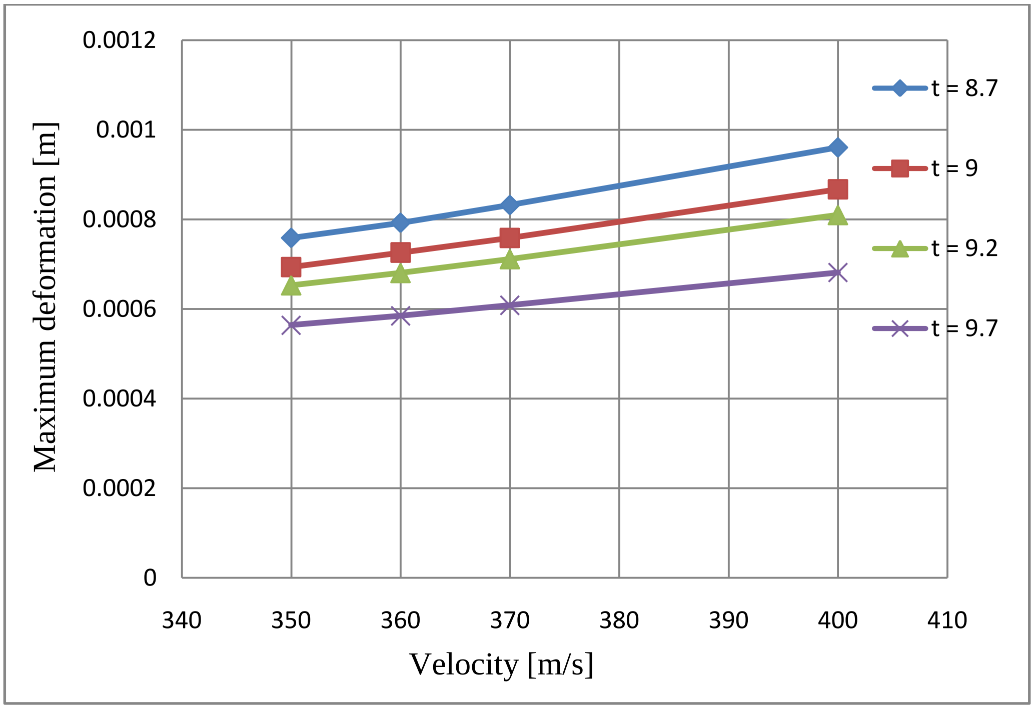

Figure 4.15: The maximum deformation of the back surface of WC-CO plates versus the impact velocity

The results obtained for the critical strain energy failure criterion method are summarized in Table 4.3 for impact speed of 350 and 360 m/s. The dimensions of the cone representing the effective deformation volume of the plate, as well as the initial kinetic energy of the projectile and the strain energy absorbed by the plate during impact are also given. It can be seen that the strain energy absorbed by the plate is only about half the initial kinetic energy of the projectile, which means the projectile penetrates the plate. This is in strong contrast with the results of the standard and elongation to fracture failure criteria for which projectiles with initial velocities between 350 and 360 m/s are stopped at plate thicknesses between 8 and 10 mm.

Table 4.3: Critical thickness calculated using the energy method

Velocity m/s	Plate thickness [m]	Front cone radius r_1 [m]	Back cone radius r_2 [m]	V_c [m^3]	$W = u * V_c$ [J]	$K_E = 1/2mv^2$ [J]
350	0.009	0.011	0.01437	4.5751E-06	478.1	1059.625
	0.01	0.0106	0.0142	4.864E-06	508.16	1059.625
360	0.009	0.011	0.01425	4.5377E-06	473.3885	1121.04
	0.01	0.0106	0.0141	4.827E-06	503.91	1121.04

Critical thicknesses for the penetration of Weldox 460 E steel, Weldox 700 E Steel, and 2024 Al-SiC plates using the elongation to fracture failure criterion and either real plasticity or perfect plasticity behaviour are summarized in Table 4.4. The corresponding projectiles and impact speeds are also provided.

Table 4.4: Simulated critical thicknesses for different plate materials, projectiles, and impact speeds using the elongation to fracture failure criterion

Material	Projectile	Experimental thickness [mm]	Impact velocity (m/s)	Modeling thickness (mm)	
				t P-P	t R-P
Weldox 460 E Steel	Conical 20 mm $\boldsymbol{\phi}$	12	290	13.6	12.2
Weldox 700 E Steel	Conical 20 mm $\boldsymbol{\phi}$	12	340.1	14	13.3
2024Al-SiC	Conical 12 mm $\boldsymbol{\phi}$	26.8	472	16.7	N/A

5 Discussion and Validation

In this study, the ballistic performance of AISI 450 stainless steel and WC-CO plates impacted by 7.62x51 mm armor piercing (AP) projectiles are investigated using Abaqus/Explicit and different failure criteria. The impact velocities range from 350 to 400 m/s and at each speed, the plate thickness is gradually changed in order to determine the critical plate thickness for penetration.

The simulated penetration process for a 9.9 mm AISI 450 stainless steel plate using standard Abaqus ductile and shear failure criteria struck by a 7.62x51mm hard tungsten carbide projectile at a velocity of 360 m/s is shown in Figure 4.1. The projectile is taken to be made of an isotropic material and to deform purely elastically during the impact; therefore, and because of the very small projectile volume, the deformation energy absorbed by the projectile is small and can be neglected.

Figure 4.2 shows that the kinetic energy of the whole system decreases rapidly during impact while the strain energy increases. For this case, the kinetic energy of the projectile exceeds the strain energy absorption capacity of the plate. Therefore, the plate fails and there is a remaining kinetic energy of the projectile after impact as seen in Figure 4.3, which means the projectile penetrates the plate. The difference between the kinetic energy and the strain energy for the model can be seen in Figure 4.2. This is due to the heat and friction loses during the impact. The simulated critical thickness for penetration of AISI 450 stainless steel plates by a 7.62x51mm hard tungsten carbide projectile at varying projectile velocities are given in Table 4.1 for the different failure criteria. It can be seen that the standard ductile and shear failure criteria yield greater thickness values as compared to those obtained using the elongation to fracture failure criterion with either real or perfect plasticity behaviour as graphically illustrated in Figure 4.11. As expected, the critical plate thicknesses are larger when a perfectly elastic-plastic material behaviour is assumed, and smaller when real elastic-plastic behaviour is considered. This is due to strain hardening in real plasticity that leads to greater material resistance to deformation and larger energy absorption, meaning thinner plates are able to stop the projectile. The deviation of the local elongation to fracture failure criterion from the standard ductile and shear failure criteria models are summarised in Table 4.1 and are 14% and 9.6% for real plasticity and perfectly elastic-plastic behaviour respectively. The simulated critical thickness for penetration of WC-CO plates by a 7.62x51mm hard tungsten carbide projectile at varying projectile velocities are given in Table 4.2 with using the elongation to fracture failure criteria. In contradiction to experimental observations that ceramic metal matrix composites provide better ballistic performance than stain steel, the modeling results suggest that the critical plate thicknesses for projectile penetration are practically identical for 80wt%WC-20wt%Co and ASIS 450 stainless steel. Since WC-Co is heavier, identical plate thicknesses would means that WC-Co plates would be heavier than stainless steel armors for identical ballistic performance. This deviation of modeling results from experiment can be rationalized by the non-consideration of friction, heat, thermal softening and adiabatic shear band formation.

Figures 4.12 and 4.15 show the maximum deformations at the target back surface for AISI 450 stainless steel and WC-CO respectively. In the case of AISI 450, the better ductility yields larger plastic deformations. In contrast, the WC-CO composites show less deformation due to their higher strength. As expected, the maximum deformation values increase with increasing initial impact velocity of the projectile.

The results obtained using the strain energy criterion are summarized in Table 4.3 for impact speeds of 350 and 360 m/s. The strain energy criterion yields critical thickness values much larger than those obtained using either the elongation to fracture criterion or the standard Abaqus ductile and shear failure criteria. This is most likely due to the inaccurate estimate of the effective deformation volume during the impact event. The effective deformation volume of the target plate is crucial for the calculation because it is the only variable parameter in equation (3.13). Therefore, the cone volume assumed in this method needs to be further investigated in order to determine it more accurately.

Experimental data for Weldox 460 E steel, Weldox 700 E Steel, and 2024 Al-SiC were obtained from literature [52-54]. The experimental thicknesses shown in Table 4.4 are the critical thicknesses for penetration. The comparison between experimental and numerical results as obtained using the elongation to fracture failure criterion for Weldox 460 E steel, Weldox 700 E Steel, and 2024Al-SiC materials are summarized in Table 4.4. As can be seen, model and experiment agree well, with a deviation of about 14% for the perfectly elastic-plastic behaviour and 6% for real plasticity. However, in the case of 2024 Al-SiC the difference between the experimental and the numerical results is quite high at approximately 37%. This could be due to different parameters between experiment and model. For instance, the material of the projectile for the 2024 Al-SiC tests is not mentioned in the literature [54] and a tungsten carbide projectile was assumed for the model [50]. Also, the contact between the plate and the projectile was considered frictionless, which is a strong simplification of the real case and may have an influence on the numerical results. Another reason for the deviation of modeling results from available test data is that the projectile may have differed with respect to shape, material and mass for most available test data. This can result in differences in the kinetic energy input during impact.

6 Conclusions

The ballistic performance of selected steels and Ceramic-Metal matrix Composites (CMMC) impacted by a 7.61x51 mm armor piercing projectile has been investigated numerically using the finite element method Abaqus/Explicit. The projectile is made of tungsten carbide and is considered undeformable. The critical thicknesses for AISI 450 stainless steel obtained using two alternative failure criteria for projectile speeds between 350 and 400m/s are compared with thicknesses obtained using Abaqus standard ductile and shear failure criteria. The elongation to fracture at the back surface of the target plate as failure criterion produces critical thickness values that are in good agreement with the results using the Abaqus standard ductile and shear failure criteria. Therefore, it is an appropriate alternative for CMMCs that cannot be modelled using the standard failure criteria due to the lack of the required large set of material data and parameters. In contrast, the strain energy model still poses some serious challenges due to the yet to solve difficulty of defining an appropriate effective deformation volume. Overall, FEA models based on the standard failure criteria and the elongation to failure criterion show a good correlation with experimental tests from literatures. The errors are less than 14% for stainless steel and 37% for CMMCs.

The relatively large modeling errors obtained, particularly at high projectile speed and for the ceramic-metal matrix composites, can be primarily related to the major simplifications assumed in this work, namely neglecting heat input, thermal softening and adiabatic shear band formation.

In the energy method, the kinetic energy of the projectile was found to be approximately twice the strain energy simulated using FEM for AISI 450 stainless steel at all thicknesses. It is assumed that this large error is primarily due to inaccurately estimating the effective deformation volume in addition to ignoring the heat, thermal softening and shear band formation as discussed previously. The alternative to estimating the effective deformation volume would be a very length and exhaustive aggregation of the energy at every element in the mesh. Future research on these error factors is expected to substantially improve the accuracy of the energy based model

7 Future work

The current thesis is practically the first of the art to investigate different failure criteria for the prediction of critical thicknesses for CMMC armor plates. As such, much remains to be done before a broad consensus can be achieved on the equivalence of the standard ductile and shear criteria and alternative failure criteria, including the local elongation to failure and the strain energy absorbed at failure. This equivalence is crucial for FEA modeling of CMMC armor plates, since a large set of data are required for the definition of the standard failure criteria that are extremely difficult to obtain for CMMCs. Following are some critical aspects deemed very important for future work:

1. Investigate the impact of strain rate by considering stress-strain material behavior.
2. Investigate the impact of local heating during impact by considering the drop in material strength with increasing temperature.
3. Develop a better method for determining the deformation volume to be used for the strain energy criterion model.
4. Carry out additional ballistic tests to validate modeling results, particularly for CMMCs.
5. Study potential adiabatic shear band formation during impact.

8 References

[1] http://en.wikipedia.org/wiki/Deformation_(engineering), retrieved December 10, 2009.

[2] William D. Callister, David G. Rethwisch, Materials Science and Engineering: An Introduction, John Wiley & Sons, 8th Edition, 2009.

[3] R. C. Hibbeler, Mechanics of Materials, Pearson Prentice Hall, 7th edition, 2008.

[4] M. Colakoglu, O. Soykasap and T. Ozek, Experimental and Numerical Investigations on the Ballistic Performance of Polymer Matrix Composites Used in Armor Design, Applied Composite Materials, 2007, Vol.14, pp.47-58.

[5] B. Basaran, Computational Analysis Of Advanced Composite Armor System, Master Of Science, 2007.

[6] L.E. Murr, In: T.Z. Blazynski, Editor, *Materials at High Strain Rates*, Elsevier Applied Science Publisher, London (1987), p. 223.

[7] M. Cottrell, J. Yu and D. Owen, The adaptive and erosive numerical modelling of confined boron carbide subjected to large-scale dynamic loadings with element conversion to undeformable meshless particles, Int. J. Impact Eng. 28 (9) (2003), pp. 1017–1035.

[8] T. Børvik, O.S. Hopperstad, T. Berstad and M. Langseth, A computational model of viscoplasticity and ductile damage for impact and penetration, *Eur. J. Mech. A/Solids* **20** (2001), pp. 685–712.

[9] M.M. Nazeer, M.A. Khan, A. Naeem and A. Haq, Analysis of conical tool perforation of ductile metal sheets, *Int. J Mech. Sci.* **42** (2000), pp. 1391–1403.

[10] D. Liu and W.J. Stronge, Ballistic limit of metal plates struck by blunt deformable missiles: experiments, *Int. J. Solids Struct.* **37** (2000), pp. 1403–1423.

[11] A. Rusinek, J.A. Rodriguez-Martinez, R. Zaera, J.R. Klepaczko, A. Arias and C. Sauvelet, Experimental and numerical study on the perforation process of mild steel sheets subjected to perpendicular impact by hemispherical projectiles, *Int. J. Impact Eng.* 36 (2009), pp. 565–587.

[12] M. Lee and Y.H. Yoo, Analysis of ceramic/metal armour systems. Int. J. Impact Eng. 25 (2001), pp. 819–829.

[13] B. Wang, G. Lu and M.K. Lim, Experimental and numerical analysis of the response of aluminum oxide tiles to impact loading. *J. Mater. Process. Technol.* 51 (1995), pp. 321–345.

[14] H. D. Espinosa, S. Dwivedi, P. D. Zavattieri and G. Yuan, A numerical investigation of penetration in multilayered material/structure system, *Int. J. Solids Struct.* 35 (1997), pp. 2975–3001.

[15] I.S. Chocron Benloulo and V. Sanchez-Galvez, A new analytical model to simulate impact onto ceramic/composite armors, *Int. J. Impact Eng.***21** 6 (1998), pp. 461–471.

[16] V. Sanchez Galve and F. Galvez Diaz-Rubio, Ballistic impact on ceramic/composite armours. In: N. Jones *etal. Structures under shock and impact V*, Computational Mechanics Publications (1998), pp. 673–681.

[17] R. Cortés, C. Navarro, M.A. Martínez, J. Rodríguez and V. Sanchez-Galvez, Numerical modeling of normal impact on ceramic composite armours. *Int. J. Impact Eng.***12** 4 (1992), pp. 639–651.

[18] J.G. Hetherington and P.F. Lemieux, The effect of obliquity on the ballistic performance of two component composite armours. *Int. J. Impact Eng.* **15** (1994), pp. 133–137.

[19] S. Sadanandan and J.G. Hetherington, Characterisation of ceramic/steel and ceramic/aluminium armours subjected to oblique impact. *Int. J. Impact Eng.* **19** (1997), pp. 811-819.

[20] V.B.C. Tan, V.P.W. Shim, and T.E. Tay, Experimental and numerical study of the response of flexible laminates to impact loading, International Journal of Solids and Structures, vol 40 (2003), pp. 6245-6266.

[21] A.H. Sheikh, P.H. Bull, and J.A. Kepler, Behaviour of Multiple Composite Plates Subjected to Ballistic Impact, Composites Science and Technology, 2009, Vol. 69, pp. 704-710.

[22] L. J. Deka, S. D. Bartus and U. K. Vaidya, Multi-site impact response of S2-glass/epoxy composite laminates, Composites Science and Technology (2008), Vol. 69, pp. 725-735.

[23] L. J. Deka, S. D. Bartus, and U. K. Vaidya, Damage Evolution and Energy Absorption of E-glass/Polypropylene Laminates Subjected to Ballistic Impact. Journal of Materials Science, 2008, Vol. 43, pp. 4399-4410.

[24] M.A.G. Silva, C. Cismasiu, and C.G. Chiorean, Numerical Simulation of Ballistic Impact on Composite Laminates. International Journal of Impact Engineering, 2005, Vol. 31, pp. 289-306.

[25] E. Sevkat, B. Liaw, F. Delale, and B.B. Raju, A Combined Experimental and Numerical Approach to Study Ballistic Impact Response of S2-Glass Fiber/Toughened Epoxy Composite Beams, Composites Science and Technology, 2009, Vol. 69, pp. 965-982.

[26] C.Y. Tham, V.B.C. Tan, and H.P. Lee, Ballistic impact of a KEVLAR helmet: Experiment and simulations, International Journal of Impact Engineering, vol. 35 (2008), pp. 304-318.

[27] H.L. Gower, D.S. Cronin, and A. Plumtree, Ballistic impact response of laminated composite panels, International Journal of Impact Engineering, vol. 35 (2008), pp. 1000-1008.

[28] T. He, H. M. Wen, and Y. Qin, Finite element analysis to predict penetration and perforation of thick FRP laminates struck by projectiles, International Journal of Impact Engineering, vol. 35 (2008), pp. 27-36.

[29] S. Chan, Z. Fawaz, K. Behdinan, and R. Amid, Ballistic Limit Prediction Using a Numerical Model with Progressive Damage Capability, Composite Structures, 2005, Vol. 77, pp. 466-474.

[30] Z. Fawaz, W. Zheng, and K. Behdinan, Numerical simulation of normal and oblique ballistic impact on ceramic composite armours, Composite Structures, vol. 63 (2004), pp. 387-395.

[31] W. L. Cheng, S. Langlie, and S. Itoh, High Velocity Impact of Thick Composites, International Journal of Impact Engineering, 2003, Vol. 29, pp. 167-184.

[32] D. Nandall, K. Williams, and R. Vaziri, Numerical simulation of the ballistic response of GRP plates, Composites Science and Technology, vol. 58 (1998), 1463-1469.

[33] J.M. Sibeaud, L. Thamié, and C. Puillet, Hypervelocity impact on honeycomb target structures: Experiments and modeling, International Journal of Impact Engineering, vol. 35 (2008), pp. 1799-1807.

[34] T. Lin, Q. Yang, C. Tan, B. Liu, and A. McDonald, Processing and ballistic performance of lightweight armors based on ultra-fine-grain aluminum composites, J. Mater. Sci. (2008), vol. 43, pp. 7344–7348.

[35] J. Swab, and L. Franks, Advances in Ceramic Armor V, Ceramic Engineering and Science Proceedings, John Wiley and Sons, Volume 30, 2009.

[36] http://en.wikipedia.org/wiki/Vehicle_armour, retrieved October 11, 2010

[37] Ronald F. Gibson, Principles of Composite Material Mechanics, McGraw-Hill, inc. 2007.

[38] F. L. Mattews and R. D. Rawlings "Composite Materials: Engineering and Science" Chapman and Hill Publications.

[39] S. R. Lampman, Advanced materials and processes, 5, 1991.

[40] R. Zaera and V. Sanchez-Galvez, Analytical modelling of normal and oblique ballistic impact on ceramic/metal lightweight armours. Int. J. Impact Eng.21 3 (1998), pp. 133–148.

[41] www1.gantep.edu.tr/~erklig/me429/introduction.ppt, retrieved December 11, 2010.

[42] http://en.wikipedia.org/wiki/Metal_matrix_composite, retrieved February 5, 2010.

[43] http://www.cmt-ltd.com/html/mat_1.htm, retrieved November 13, 2010.

[44]http://www.ceramicindustry.com/Articles/Feature_Article/63fe89b404ac7010VgnVCM100000f932a8c0, retrieved November 12, 2010.

[45] A. Bhatnagar, Lightweight Ballistic Composites for Military and Law-Enforcement Applications, Woodhead Publishing Ltd. 2006.

[46] ABAQUS Inc., Getting Started with ABAQUS (v. 6.7), ABAQUS Inc., 2007

[47] T. C. Totemeier, C. J. Smithells, Smithells metals reference book, a Butterworth-Heinemann title, 8th edition, 2003, pp 23-33

[48] http://www.defensemunitions.com/nammo/7-62x39mm/copy_of_Epson_Generic_Museo_Instructions-1.pdf/, retrieved January 20, 2010.

[49] http://en.wikipedia.org/wiki/7.62x51mm_NATO, retrieved January 20, 2010.

[50] http://www.memsnet.org/material/tungstencarbidewcbulk/, retrieved December 12, 2009.

[51] F. J. Thomas, R. V. Mark, W. Tusit, and M. Paul, Extracting Stress-Strain and Compressive Yield Stress Information From Spherical Indentation, Weapons and Materials Research Directorate, ARL- TR-4229, 2007.

[52] S. Dey, T. Børvik, O.S. Hopperstad, J.R. Leinum, and M. Langseth, The effect of target strength on the perforation of steel plates using three different projectile nose shapes, International Journal of Impact Engineering, vol. 30 (2004), pp 1005–1038.

[53] T. Børvik, M. Langseth, O.S. Hopperstad, and K.A. Malo, Perforation of 12mm thick steel plates by 20mm diameter projectiles with flat, hemispherical and conical noses Part I: Experimental study, International Journal of Impact Engineering, vol. 27, (2002), pp 19–35.

[54] T. Lin, Q. Yang, C. Tan, B. Liu and A. McDonald, Processing and ballistic performance of lightweight armors based on ultra-fine-grain aluminum composites, J Mater Sci (2008) vol. 43, pp 7344–7348.

[55] D. Delfosse, and A. Poursartip, Experimental parameter study of static and dynamic out of plane loading of CFRP laminates, Proceeding of tenth international conference on composite materials (ICCM10), 583590, 1995.

[56] http://wapedia.mobi/en/7.62x51mm_NATO, retrieved April 1, 2011.

9 Appendix

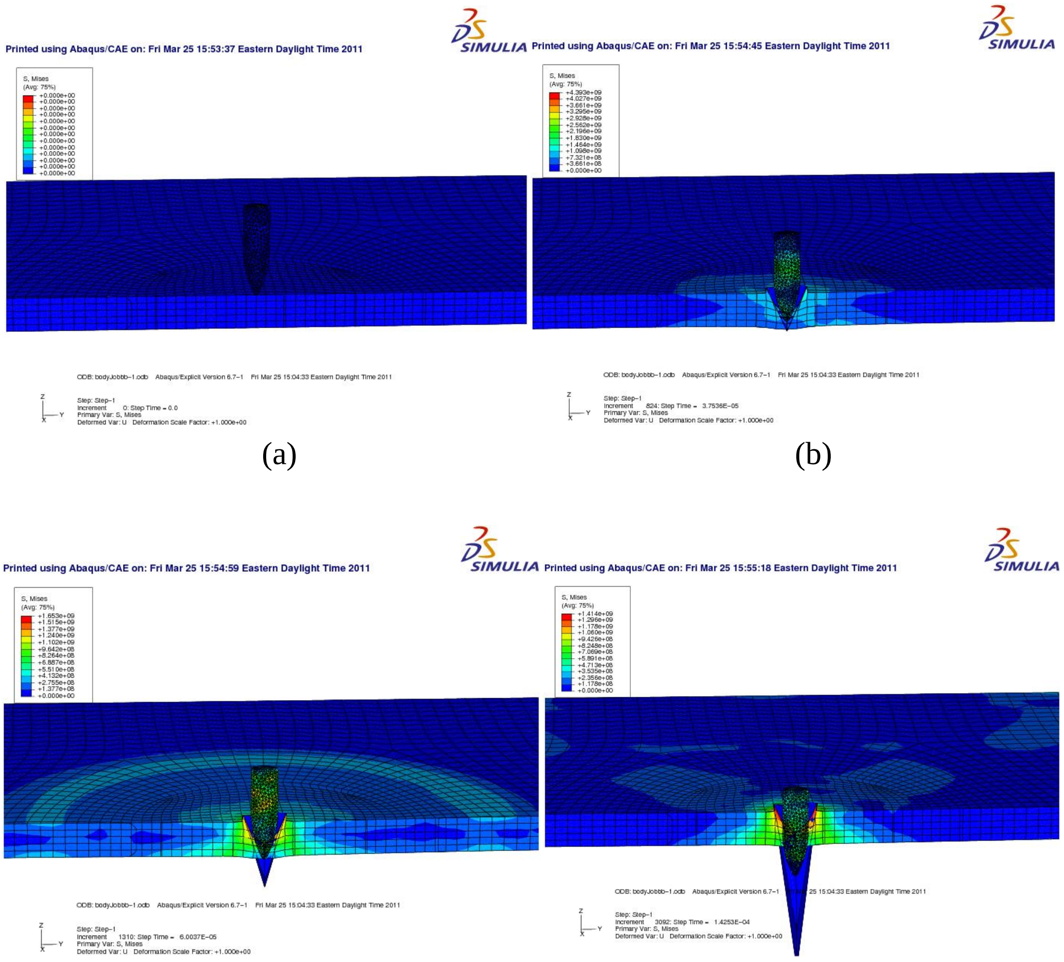

(a) (b)

(c) (d)

Figure 9.1: Penetration simulation of a 7.62x51mm hard tungsten carbide projectile with an impact velocity of 350 m/s through a 9 mm thick AISI 450 stainless steel plate

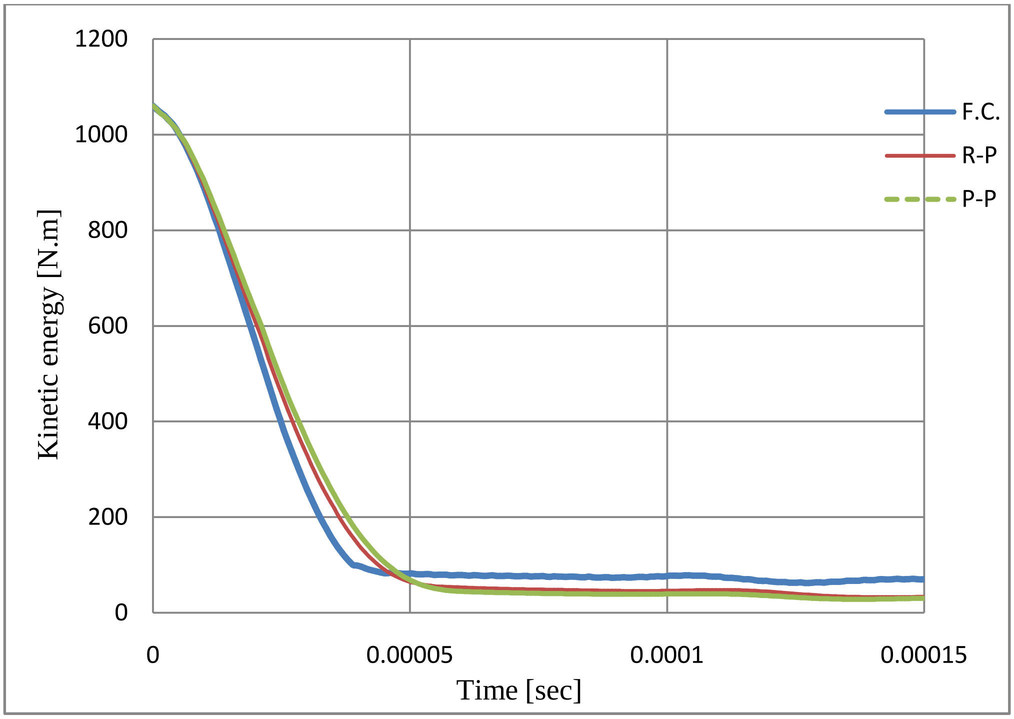

Figure 9.2: Kinetic energy for the whole model of AISI stainless steel plate by a 7.62x51mm hard tungsten carbide projectile at a velocity of 350 m/s by using different failure criteria

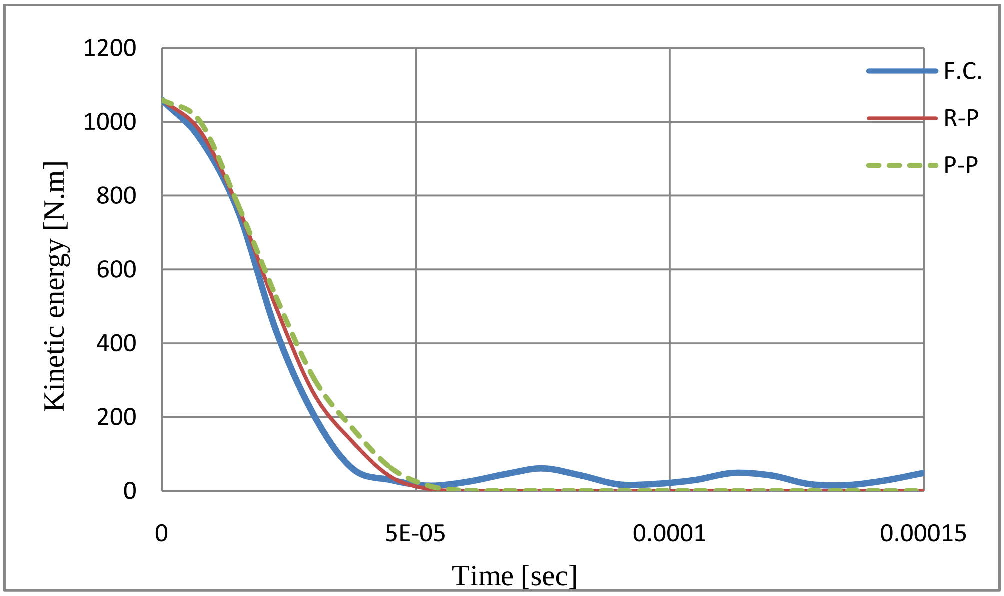

Figure 9.3: Kinetic energy of the projectile during the impact of AISI stainless steel plate at a velocity of 350 m/s by using different failure criteria

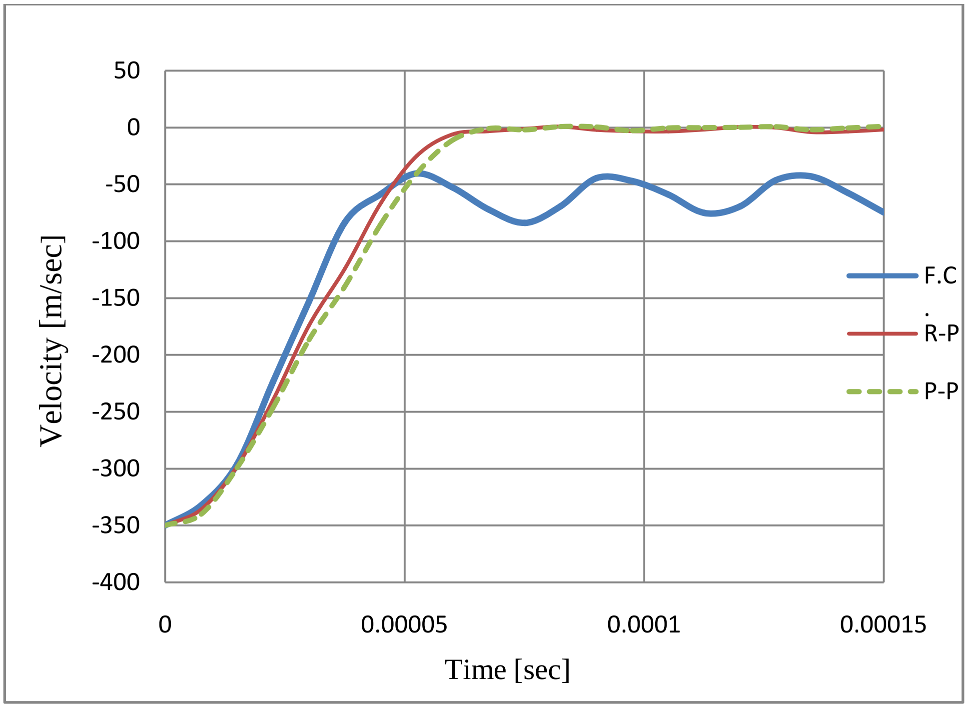

Figure 9.4: The velocity of the projectile during the impact of AISI stainless steel plate at 350 m/sec by using different failure criteria

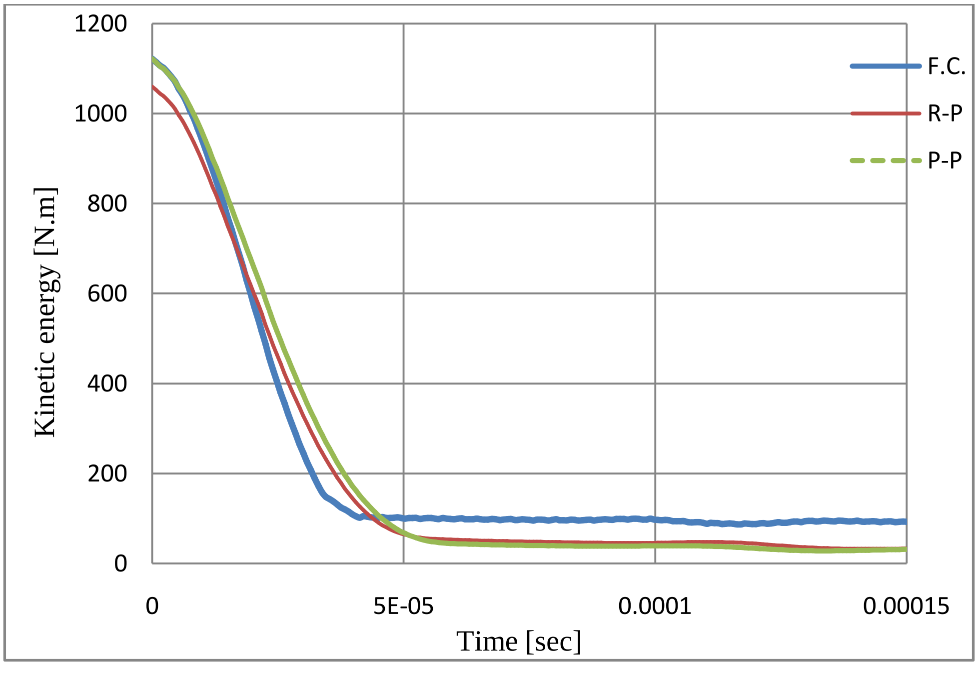

Figure 9.5: Kinetic energy for the whole model of AISI stainless steel plate by a 7.62x51mm hard tungsten carbide projectile at a velocity of 360 m/s by using different failure criteria

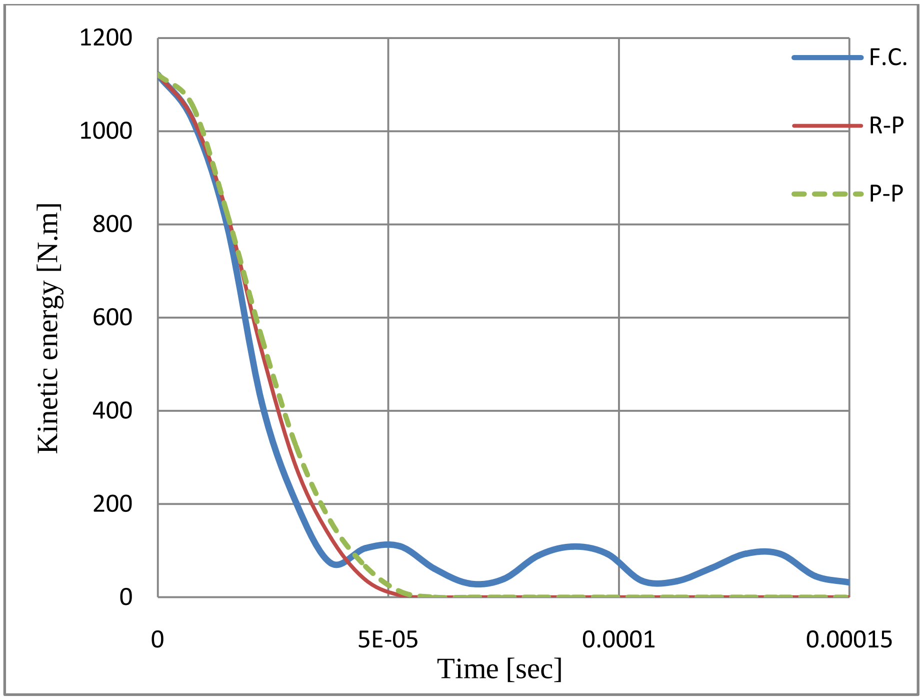

Figure 9.6: Kinetic energy of the projectile during the impact of AISI stainless steel plate at a velocity of 360 m/s by using different failure criteria

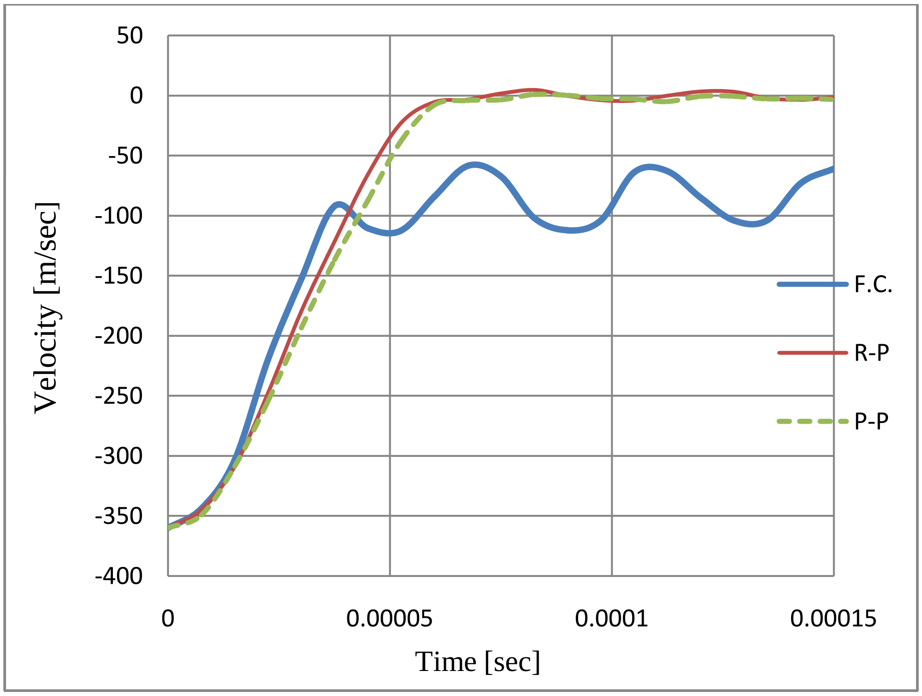

Figure 9.7: The velocity of the projectile during the impact of AISI stainless steel plate at 360 m/sec by using different failure criteria

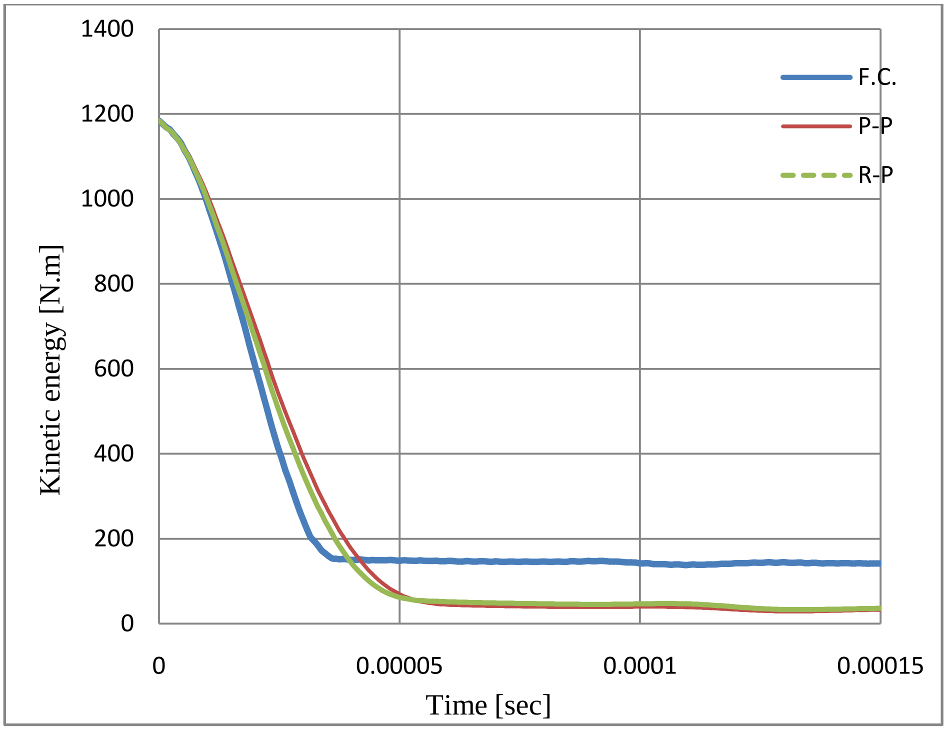

Figure 9.8: Kinetic energy for the whole model of AISI stainless steel plate by a 7.62x51mm hard tungsten carbide projectile at a velocity of 370 m/s by using different failure criteria

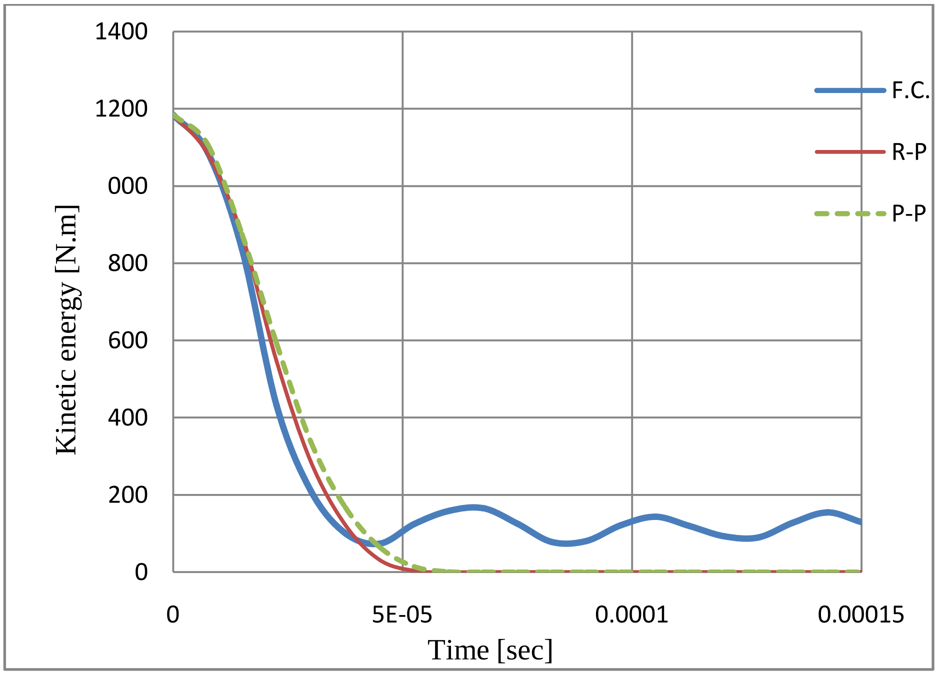

Figure 9.9: Kinetic energy of the projectile during the impact of AISI stainless steel plate at a velocity of 370 m/s by using different failure criteria

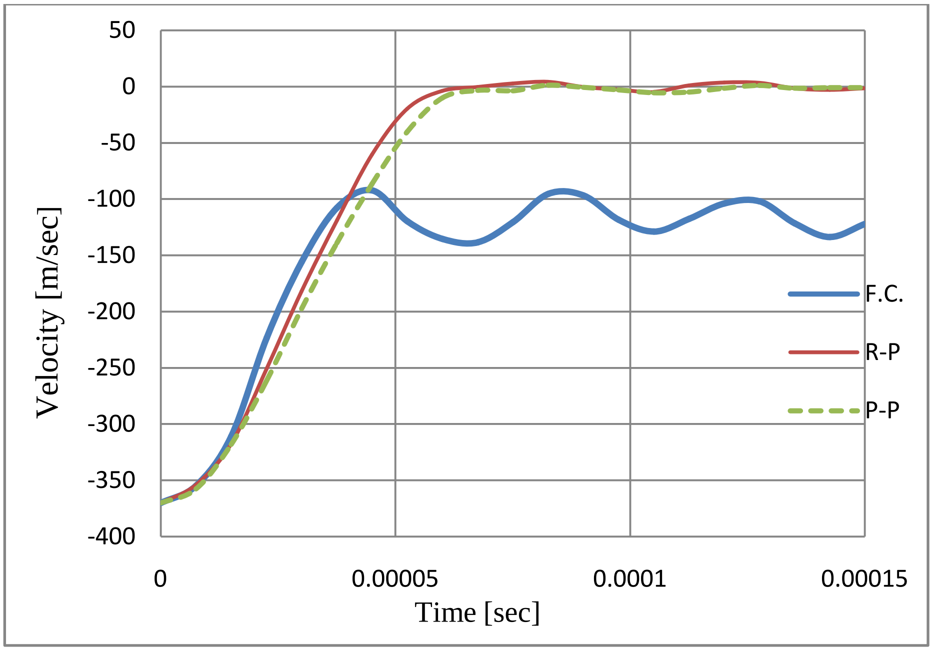

Figure 9.10: The velocity of the projectile during the impact of AISI stainless steel plate at 370 m/sec by using different failure criteria

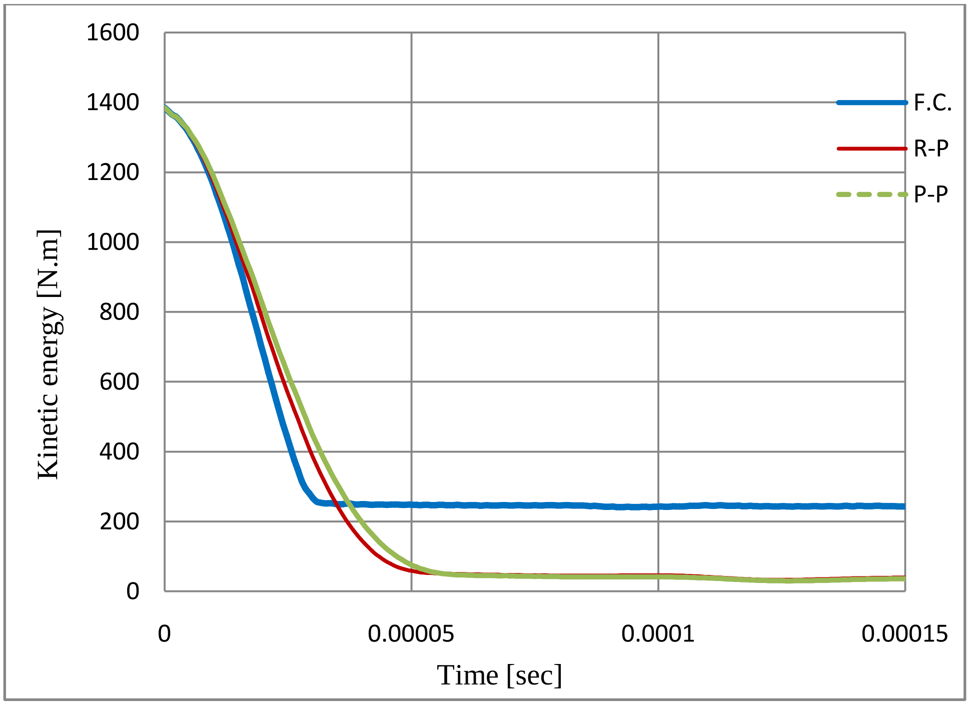

Figure 9.11: Kinetic energy for the whole model of AISI stainless steel plate by a 7.62x51mm hard tungsten carbide projectile at a velocity of 400 m/s by using different failure criteria

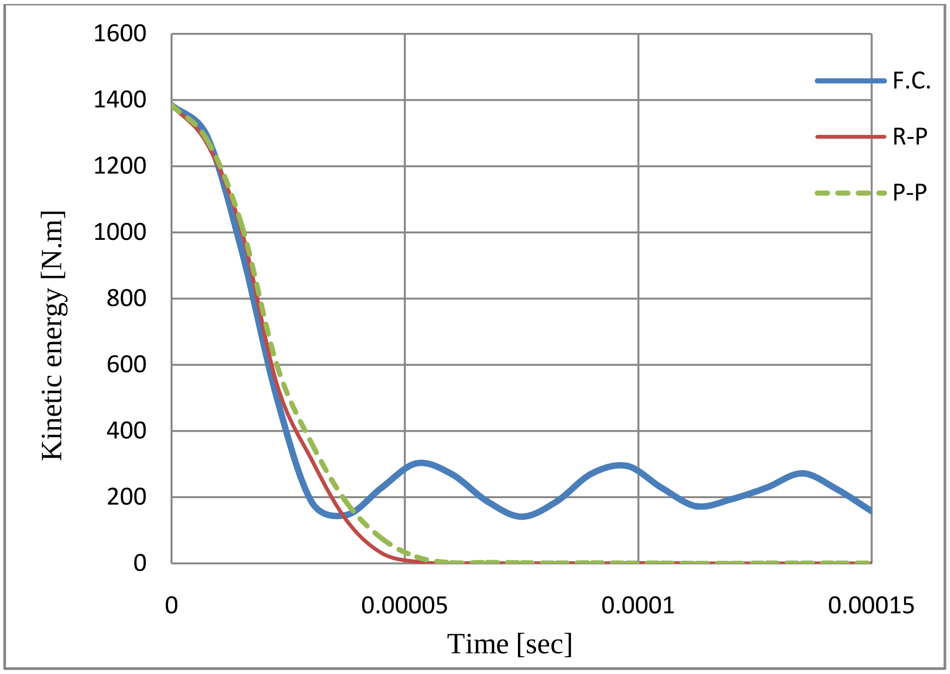

Figure 9.12: Kinetic energy of the projectile during the impact of AISI stainless steel plate at a velocity of 400 m/s by using different failure criteria

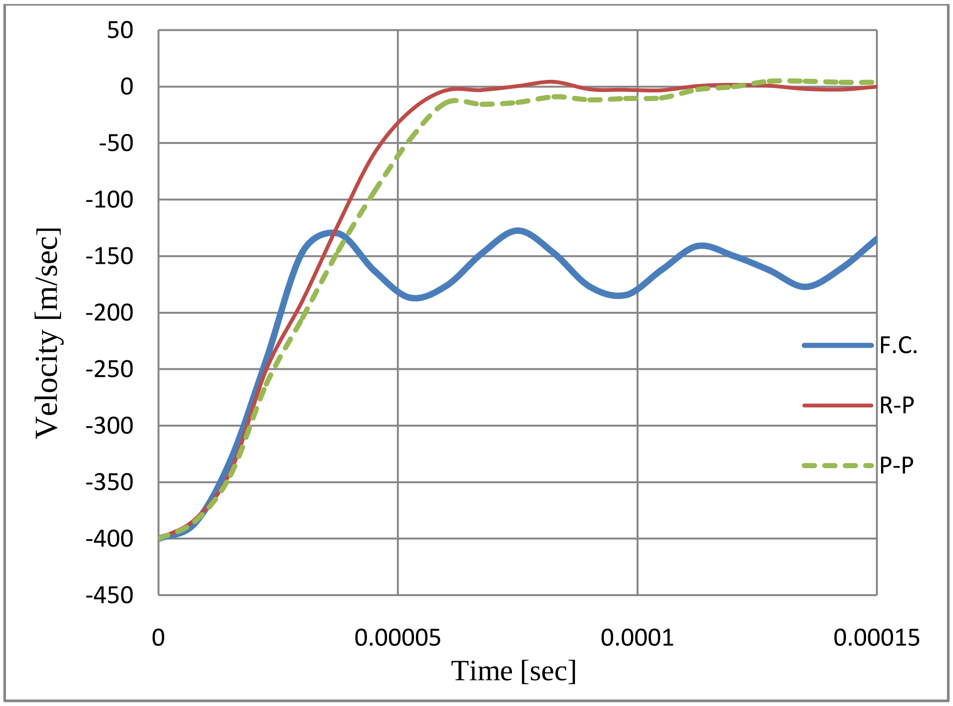

Figure 9.13: The velocity of the projectile during the impact of AISI stainless steel plate at 400 m/sec by using different failure criteria

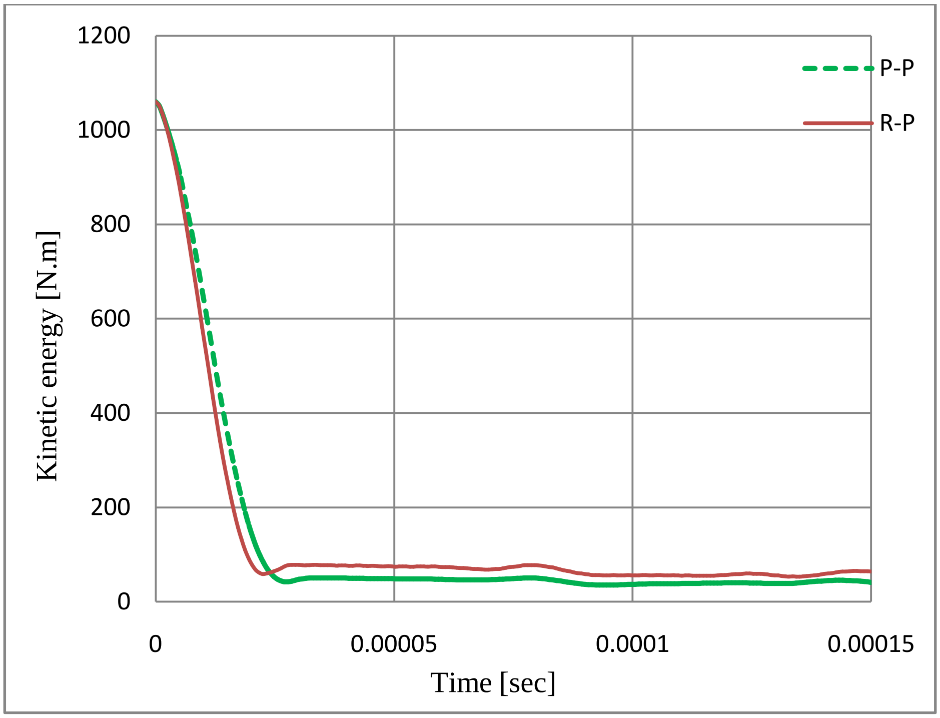

Figure 9.14: Kinetic energy for the whole model of WC-CO plate by a 7.62x51mm hard tungsten carbide projectile at a velocity of 350 m/s by using the elongation to fracture failure criterion

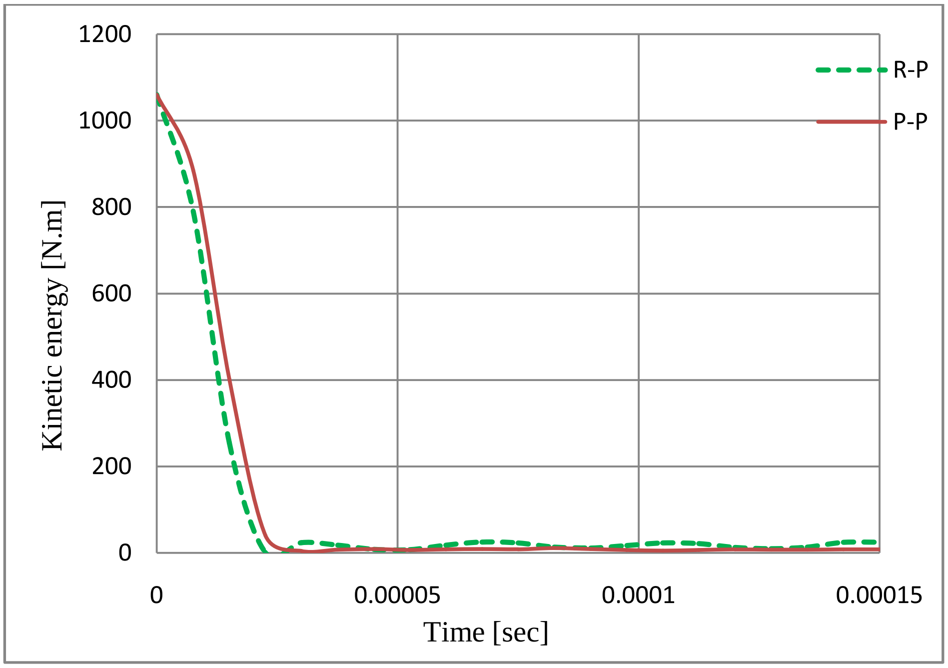

Figure 9.15: Kinetic energy of the projectile during the impact of WC-CO plate at a velocity of 350 m/s by using the elongation to fracture failure criterion

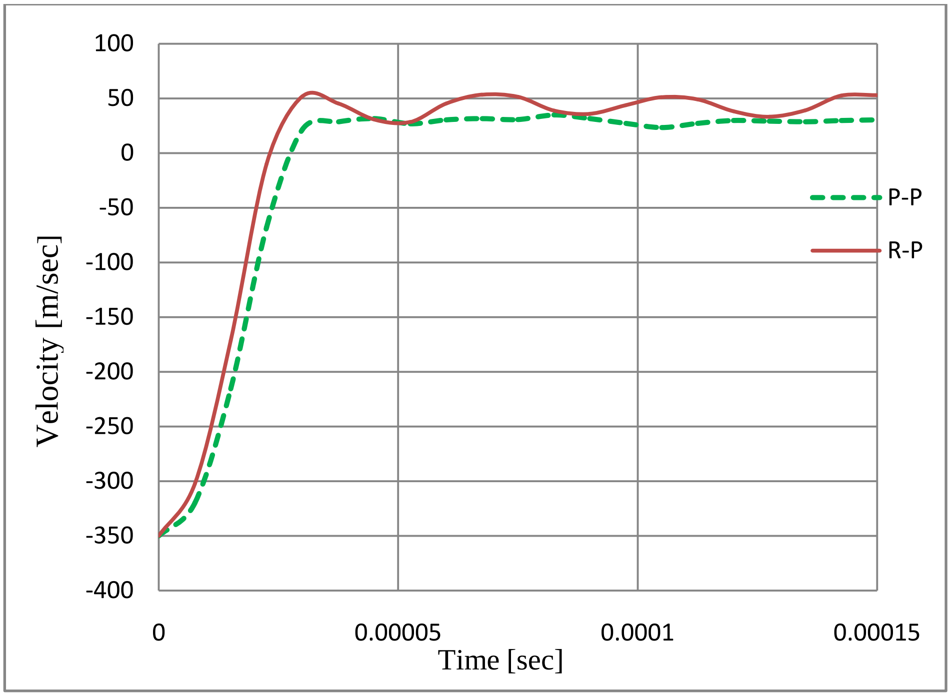

Figure 9.16: The velocity of the projectile during the impact of WC-CO plate at 350 m/sec by using the elongation to fracture failure criterion

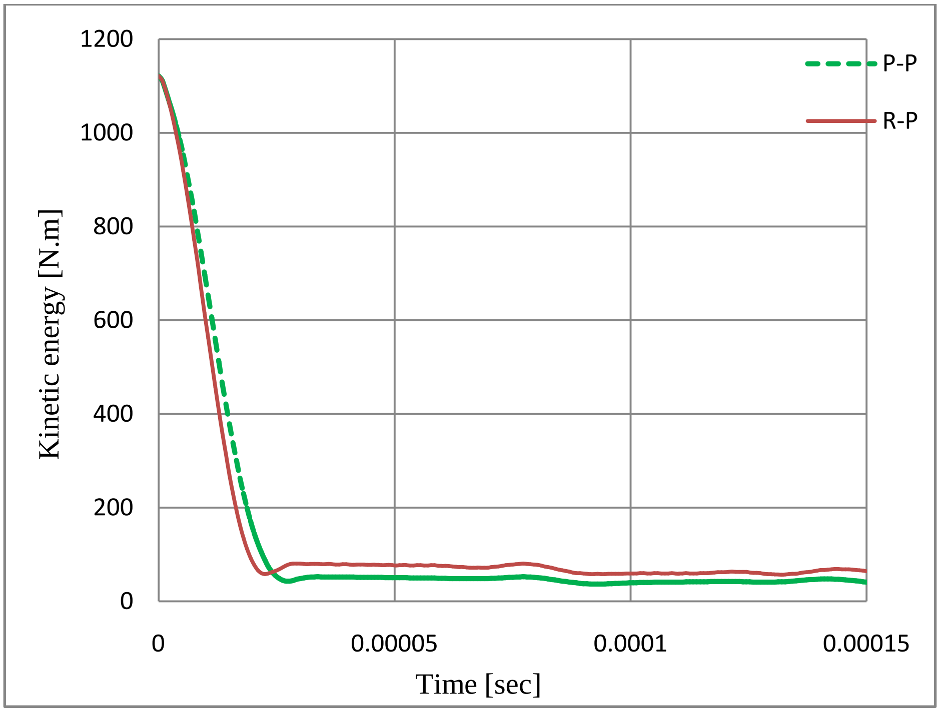

Figure 9.17: Kinetic energy for the whole model of WC-CO plate by a 7.62x51mm hard tungsten carbide projectile at a velocity of 360 m/s by using the elongation to fracture failure criterion

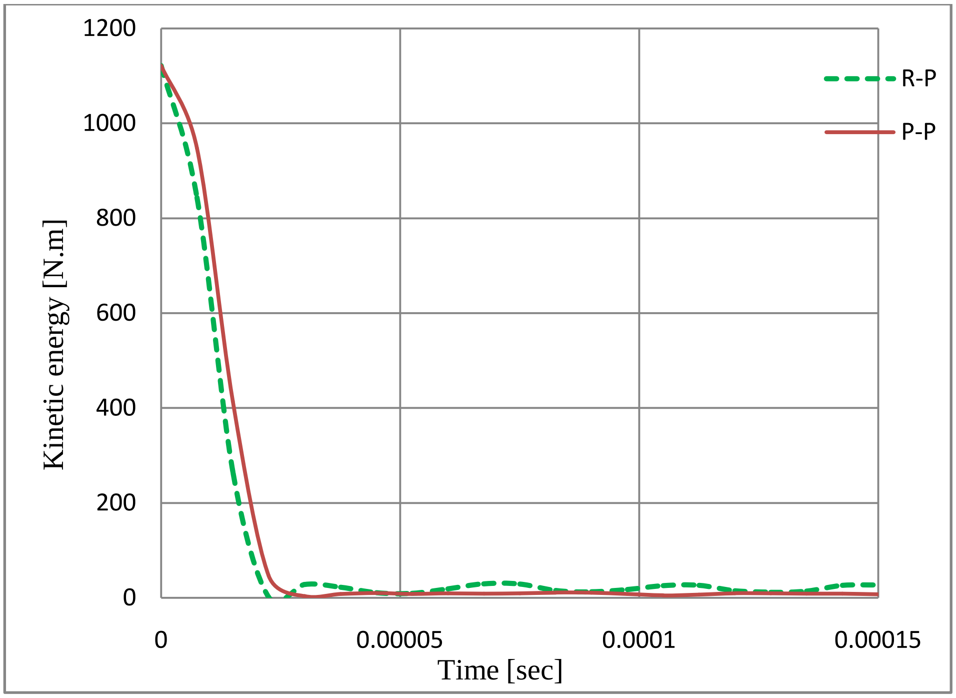

Figure 9.18: Kinetic energy of the projectile during the impact of WC-CO plate at a velocity of 360 m/s by using the elongation to fracture failure criterion

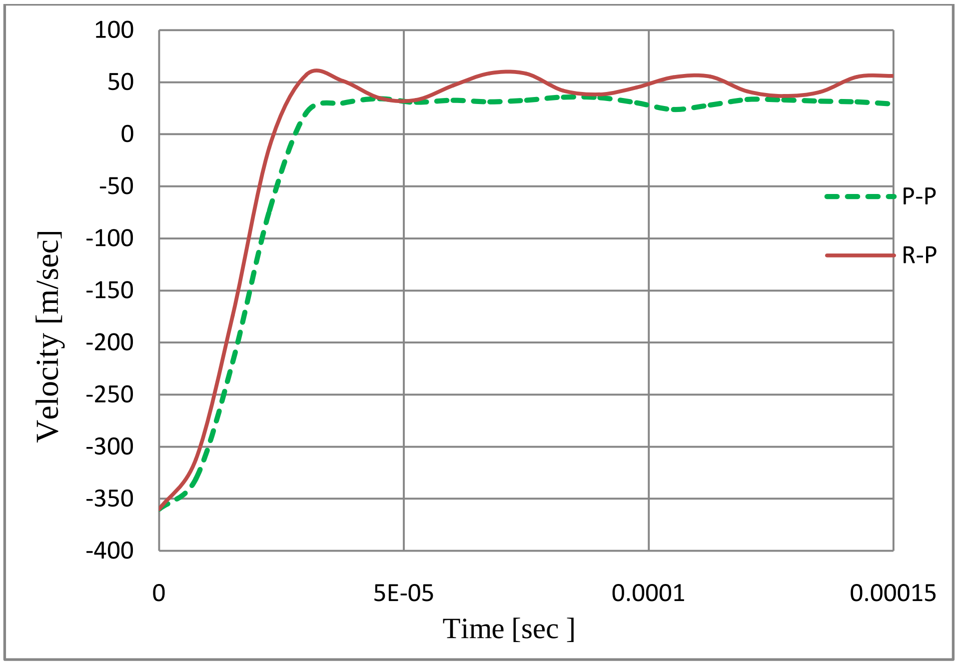

Figure 9.19: The velocity of the projectile during the impact of WC-CO plate at 360 m/sec by using the elongation to fracture failure criterion

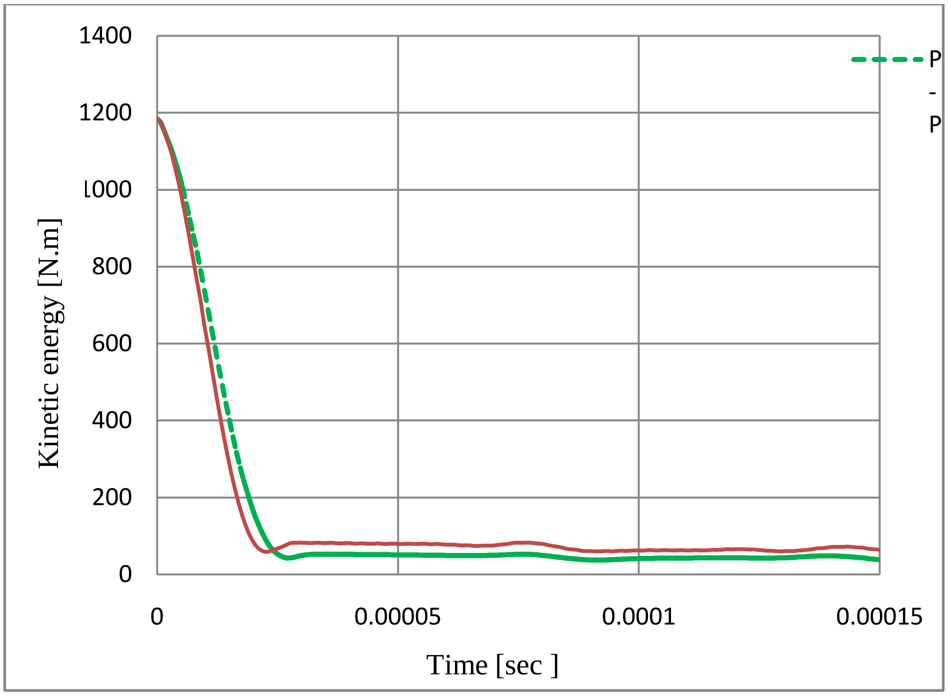

Figure 9.20: Kinetic energy for the whole model of WC-CO plate by a 7.62x51mm hard tungsten carbide projectile at a velocity of 370 m/s by using the elongation to fracture failure criterion

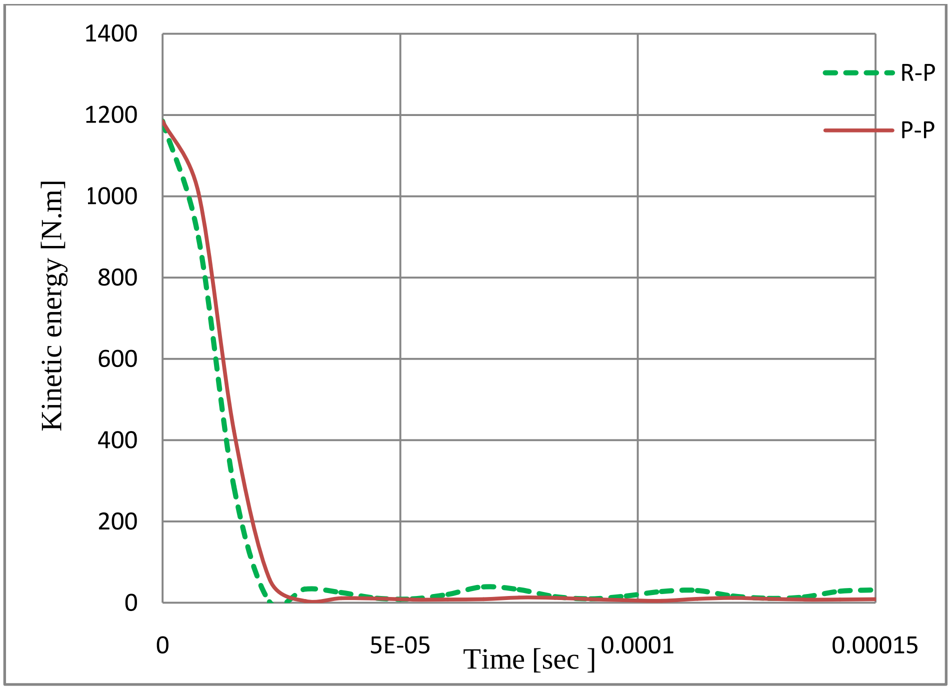

Figure 9.21: Kinetic energy of the projectile during the impact of WC-CO plate at a velocity of 370 m/s by using the elongation to fracture failure criterion

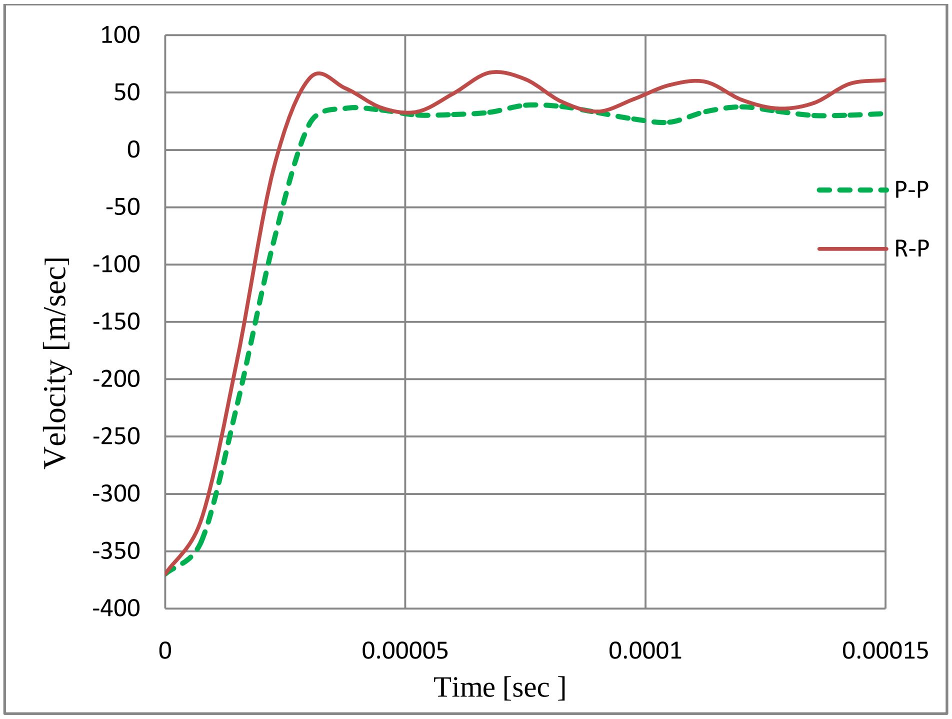

Figure 9.22: The velocity of the projectile during the impact of WC-CO plate at 370 m/sec by using the elongation to fracture failure criterion

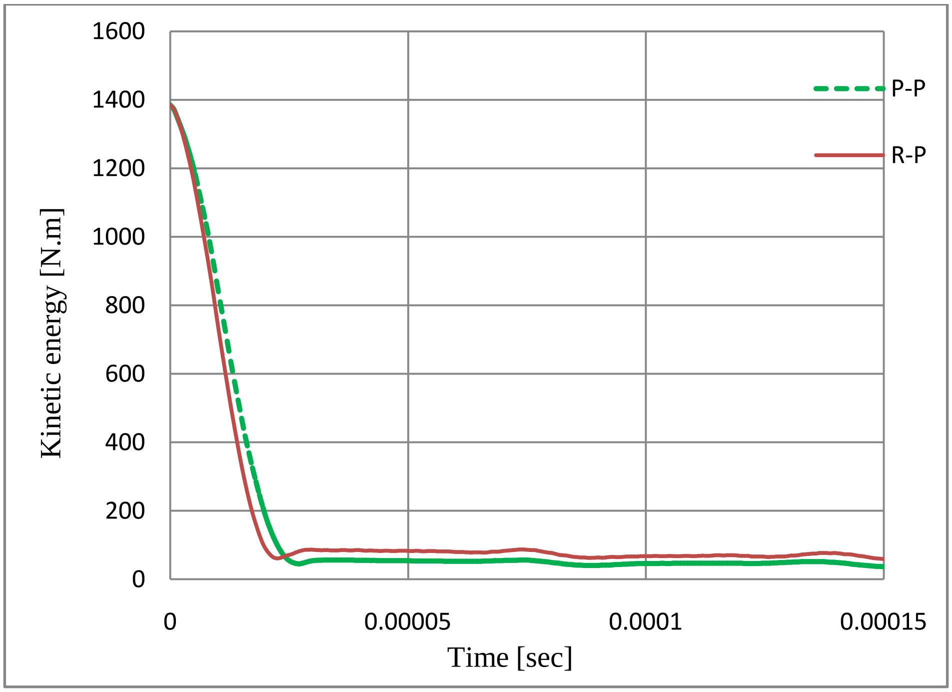

Figure 9.23: Kinetic energy for the whole model of WC-CO plate by a 7.62x51mm hard tungsten carbide projectile at a velocity of 400 m/s by using the elongation to fracture failure criterion

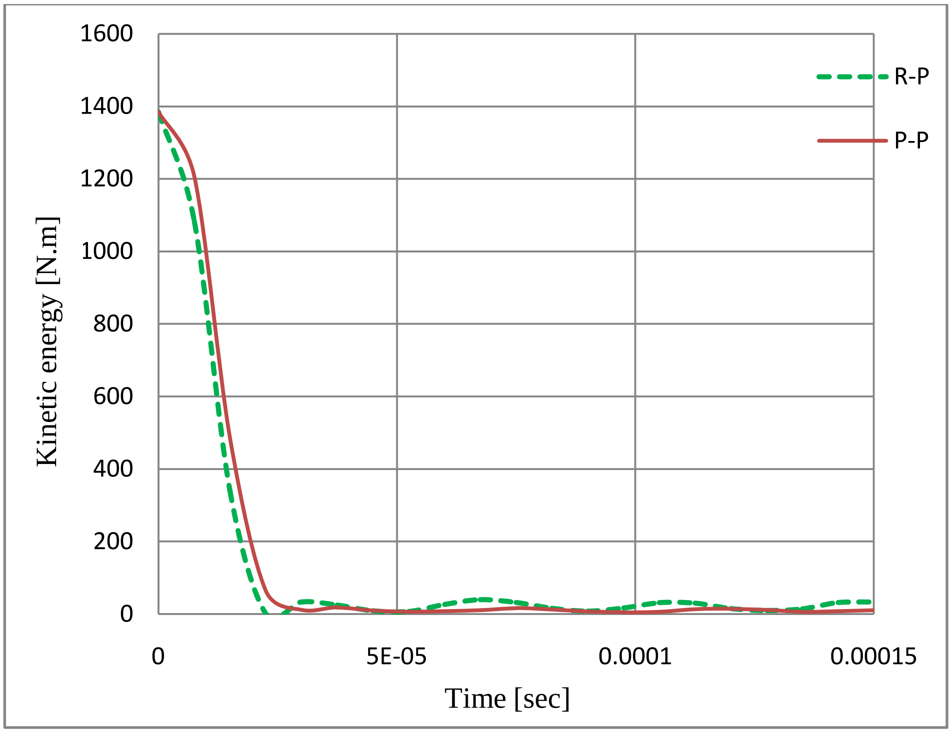

Figure 9.24: Kinetic energy of the projectile during the impact of WC-CO plate at a velocity of 400 m/s by using the elongation to fracture failure criterion

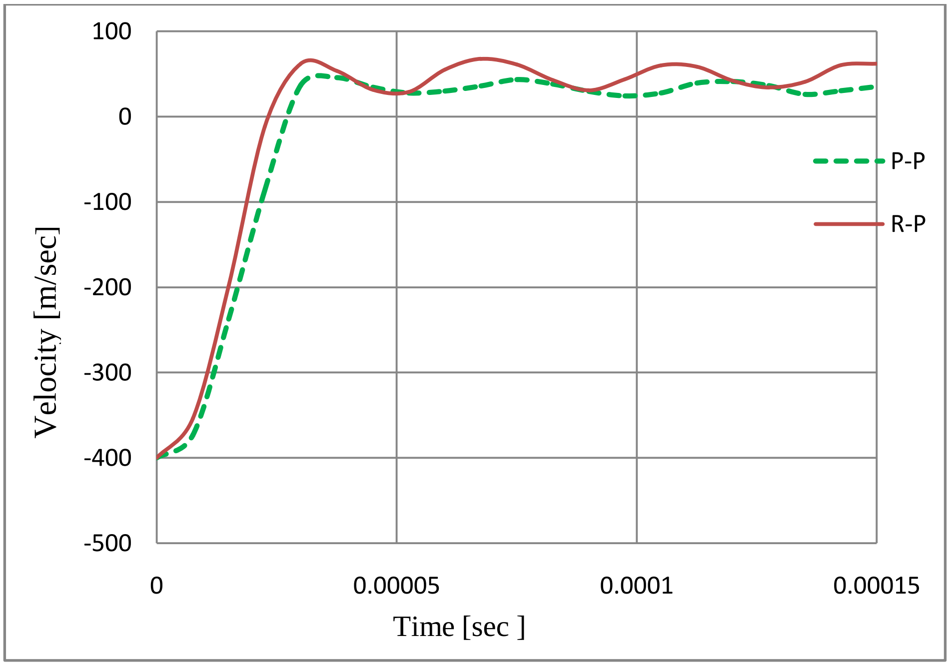

Figure 9.25: Kinetic energy of the projectile during the impact of WC-CO plate at a velocity of 400 m/s by using the elongation to fracture failure criterion